UNIVERSITÄT BONN
Physikalisches Institut

Measurement of the Mass of the Top Quark in Dilepton Final States with the DØ-Detector

von

Oleg Brandt

In the Standard Model (SM) the top quark mass is a fundamental parameter. Its precise measurement is important to test the self-consistency of the SM. Additionally, it offers sensitivity to New Physics beyond the Standard Model. In proton anti-proton collisions at a centre-of-mass energy of $\sqrt{s} = 1.96$ TeV $t\bar{t}$ quarks are pair-produced, each decaying into a W boson and a b quark. In the dilepton channel both W bosons decay leptonically. Because of the presence of two neutrinos in the final state the kinematics are underconstrained. A so-called Neutrino Weighting algorithm is used to calculate a weight for the consistency of a hypothesised top quark mass with the event kinematics. To render the problem solvable, the pseudorapidities of the neutrinos are assumed. The Maximum Method, which takes the maximum to the weight distribution as input to infer the top quark mass, is applied to approximately 370 pb^{-1} of Run-II data, recorded by the DØ experiment at the Tevatron. The $e\mu$-channel of the 835 pb^{-1} dataset is analysed.
The top quark mass is measured to

$$
\begin{aligned}
m_{\mathrm{top}}^{370\,\mathrm{pb}^{-1}} &= 176.8\,\mathrm{GeV} \quad {}^{+17.5}_{-29.3}\,\mathrm{GeV\ (stat.)} \quad {}^{+4.0}_{-4.8}\,\mathrm{GeV\ (syst.)} \\
m_{\mathrm{top}}^{835\,\mathrm{pb}^{-1}} &= 165.5\,\mathrm{GeV} \quad \pm 10.0\,\mathrm{GeV\ (stat.)} \quad {}^{+3.9}_{-4.2}\,\mathrm{GeV\ (syst.)}\,.
\end{aligned}
$$

Post address:
Nussallee 12
D-53115 Bonn
Germany

BONN-IB-2006-13
Bonn University
September 2006

UNIVERSITÄT BONN
Physikalisches Institut

Measurement of the Mass of the Top Quark in Dilepton Final States with the DØ-Detector.

von
Oleg Brandt

Dieser Forschungsbericht wurde als Diplomarbeit von der mathematisch-naturwissenschaftlichen Fakultät der Universität Bonn angenommen.

Angenommen am:	04. September 2006
Referent:	Prof. Dr. N. Wermes
Korreferent:	Prof. Dr. E. Hilger

Contents

1. Introduction and Motivation

By convention sweet, by convention bitter, by convention hot, by convention cold, by convention colour: but in reality atoms and void.

Democritus, V-IV century b.C.

For generations, Mankind is looking for answers on how our world is organised and what governs it in order to understand who we are by analysing *our* reflection of the world. Evidence of ancestral cults indicating this continuous strive for explanations can be traced back to times as early as several tens of thousands of years ago.

A milestone to our modern view of the world was placed by Greek philosophers more than 3000 years ago. Besides bringing the idea of empiricism to a higher level, they contributed another essential element to Science as we know it today – strict logic. An excellent example is the citation of Democritus above, who anticipated the main idea of Elementary Particle Physics by introducing the concept of "the indivisible" – "$\alpha\tau o\mu o\varsigma$" from the observation that stepstones would be abraded in not visible, infinitely small pieces.

This approach was carried to a scientific level by (post-) renaissance philosophers. For the first time experiments were *intentionally* and systematically designed to probe Nature. A milestone for the change of this paradigm is the works of Galileo. For instance, he derived the acceleration law $s = a/2 \cdot t^2$ by measuring the acceleration due to Earth's gravitation using inclined surfaces and pendulums.

This naturally grown scientific approach has drastically changed our view of the world and our view of ourselves over the last millennia. The advancements of Science culminated in the great discoveries of the XX century, like the Theory of Relativity, Quantum Mechanics, the discovery of the role of the DNA, the ongoing investigation of the genome, and the understanding of the history of the Universe to name a few.

However, besides the crucial breakthroughs listed above the most intriguing question still remains: what are the most elementary building blocks our world is made of? Elementary Particle Physics attempts to answer this question. Of course, there is no final answer and, fortunately, never will be. Over the XX-th century the so-called Standard Model of Elementary Particle Physics has emerged [1, 2, 3, 4, 5, 6, 7], which serves us tremendously well in interpreting experimental findings. In the beginning of the 90's the Tevatron, the world's most powerful proton anti-proton collider with a centre-mass energy of $\sqrt{s} = 1.8\,\text{TeV}$, was launched. Its both experiments, DØ and CDF, are testing the validity of the Standard Model at this ever higher energy range and looking for New Physics. With success. The Tevatron's Run I culminated in the the discovery of the top quark in 1995 by DØ and CDF collaborations [8, 9]. In fact, the top quark is the most recently discovered particle with the exception of the tau neutrino. The existence of

the top quark was predicted in 1977 as the electroweak isospin partner of the bottom quark. Its mass, being the subject of this thesis, could be inferred from fits to electroweak precision data using theoretical input from the Standard Model. Finally, the prediction was confirmed by the discovery and direct measurement in 1995 [8, 9] at the Tevatron.

The top quark is utterly interesting for a variety of reasons. The most intriguing one is risen by its high mass of $172.3 \pm 3.3\,\mathrm{GeV}$ [10]: is there a possible connection to the mechanism of the Spontaneous Symmetry Breaking? In the Standard Model, this mechanism is responsible for the masses of elementary particles. Canonically, Spontaneous Symmetry Breaking is incorporated in the Standard Model by introducing a scalar Higgs field with the Higgs boson being the excitation eigenstate of it [7]. Understanding the high mass of the top quark might yield new insights into Spontaneous Symmetry Breaking. The coupling of the Higgs field is strongest for the top quark together with the $\mathcal{O}(100\,\mathrm{GeV})$ heavy $W^{\pm}$, Z bosons, compared to other elementary particles. In fact, their masses and the mass of the Higgs boson, which still remains to be found, are important parameters of the Standard Model and are connected to each other. This is why their precision measurement is so important and might reveal some New Physics. Furthermore, the high top quark mass results in an extremely short life time of $\tau \simeq 0.5 \times 10^{-24}\,\mathrm{s}$, which makes the formation of bound states impossible. Therefore, the information about its quantum numbers, for instance the spin, does not get lost and can be measured [11]. All this makes the top quark the hottest Elementary Particle Physics topic of our time.

At the Tevatron, the top quarks are dominantly produced in pairs. Within the Standard Model, there are 3 decay channels for a top anti-top pair. The subject of this thesis is the measurement of the top quark mass in the so-called dilepton channel, which is characterised by two bottom quarks and two leptons together with the corresponding neutrinos from W-boson decay in the final state. Despite the low branching ratio, the dilepton channel is highly important due to its low background and low systematics. It offers a possibility to test the Standard Model and could reveal New Physics, which cannot be seen in other channels. The presented analysis is based on the so-called Neutrino Weighting algorithm combined with the Maximum Method for the top mass extraction and was presented as a DØ preliminary at the ICHEP 2006 conference [12, 13].

This Diploma thesis is organised as follows:

- Theoretical Aspects relevant for this analysis covered in Chap. 2;
- The Experimental Setup – the Tevatron and the DØ detector – is described in Chap. 3;
- The Analysed Dataset and the selection criteria applied are explained in Chap. 4;
- The Neutrino Weighting Method for inferring the top mass is described in Chap. 5;
- The Maximum Method for the Top Quark Mass Extraction is presented in Chap. 6;
- Testing the Maximum Method with Pseudo-Experiments can be found in Chap. 7;
- Results found in all dileptonic channels of the $370\,\mathrm{pb}^{-1}$ dataset and in the $e\mu$ channel of the $835\,\mathrm{pb}^{-1}$ dataset are presented in Chap. 8;
- The Systematic Uncertainties are evaluated in Chap. 9;
- Conclusion and outlook from the findings of this analysis are drawn in Chap. 10 and 11.

2. Theoretical Aspects

To our current knowledge[1], the world is built of fundamental particles which are governed by four basic types of interactions. They are organised[2] in a scheme described by the so-called Standard Model of Elementary Particle Physics (SM). A brief review of the Standard Model shall be given in the following. The most recently discovered hadronic particle of the Standard Model – the Top Quark and its physical properties are introduced thereafter. Special emphasis is given to its mass, being the subject of this thesis.

2.1. The Standard Model

Over the last decades, the Standard Model has served us tremendously well as a description of the world's most fundamental known processes. It was developed in the course of the last century, and the progress culminated in a hot phase in the 60's and 70's. There is a lot of canonical literature available, for example [14, 15, 16, 17]. It should be mentioned, that although the Standard Model is an appropriate model, it is not the final answer to questions of Particle Physics, as it is governed by many free parameters and a more fundamental theory is still to be found. Further, difficulties arise when incorporating most recent experimental results like the non-zero neutrino masses or the gyromagnetic factor of the muon.

2.1.1. Brief Overview of the Standard Model

The Standard Model of Particle Physics describes the elementary particles observable in our world as well as three of the four basic interactions ruling them: the strong, the weak, and the electromagnetic interaction. Yet, there is no canonical way to include the gravitational interaction in the Standard Model.

The Bosonic Sector of the Standard Model

From a theoretical point of view, the Standard Model is a quantum field theory based on the principle of local gauge invariance, which, starting from the $\mathbb{SU}_C(3) \times \mathbb{SU}_L(2) \times \mathbb{U}_Y(1)$ symmetry, yields a formalism for the description of the strong, the weak and the electromagnetic interaction in a natural way [1, 2, 3]. These interactions are mediated by force carriers, the so-called gauge bosons, being the eigenstates of the field constructed to preserve the gauge invariance. The

[1] "Knowledge" in this context refers to experimentally proven results.
[2] up to the gravitational interaction.

Generation		I	II	III
Fermionic Sector:	leptons:	ν_e (1953)	ν_μ (1962)	ν_τ (2000)
		e (1897)	μ (1936)	τ (1975)
	quarks:	u (1968)	c (1974)	t (1995)
		d (1968)	s (1964)	b (1977)
Bosonic Sector:	gauge bosons:		$g_1, ..., g_8$ (1979)	
			γ (1900)	
			$W^\pm, Z^0$ (1983)	

Table 2.1.: The scheme of elementary particles described by the Standard Model. In parentheses, the year of discovery is given [15, 16, 8, 9]. Although essential to the SM, the Higgs particle, being a scalar boson, is not shown here, since it has not been discovered yet.

gauge bosons are: 8 gluons[3] for $\mathbb{SU}_C(3)$ and the colour charge gauge field associated with it, plus the $W^\pm$, Z, γ bosons for the electroweak interaction. All force carriers have an even non-zero spin, giving them the name vector bosons. The force carriers of the strong and the electroweak interaction have spin 1. There is a consensus that the graviton, the vector boson of the gravitational force, is expected to be a tensor particle with a spin of 2.

The Fermionic Sector of the Standard Model

The particles of the Standard Model can be divided up into two distinct groups with respect to their role in the theory. Besides the Bosonic Sector, all remaining particles described by the Standard Model[4] comprise the so-called Fermionic Sector. As the name implies, they have spin 1/2.

In the framework of the Standard Model, the fermions are organised in a scheme with respect to their masses and the interactions in which they can participate. First, there is the quark and the leptonic sector. Quarks participate in strong and electroweak interactions. Leptons, however, cannot undergo any strong processes. Particles of both the quark and the leptonic sector can be divided up into two categories with respect to their electric charge: quarks can carry either the charge +2/3 and -1/3, leptons -1 and 0; the neutral leptons are called neutrinos. In both sectors, there are 3 pairs of particles, called generations, which are organised in increasing mass. To both particles in a given pair a so-called isospin quantum number is assigned, indicating them as dominant partners of each other regarding the weak interaction. Each particle of the fermionic sector has a so-called anti-particle, featuring the same mass, but opposite inner quantum numbers like charge.

The particles of the Standard Model are summarised for convenience in Tab. 2.1. Fundamental publications [1, 2, 3] on the unification of the weak and the electromagnetic interaction placed the milestone of the Standard Model in the 60's. The theory of the strong interacion, Quantum Chromo-Dynamics, was formulated in the 70's [4, 5, 6]. The theoretical framework of the Standard Model is summarised in [14, 15, 16, 17].

[3] to be precise, the theory features 9 gluons, but one of them must remain colourless and is irrelevant

[4] with the exclusion of the Higgs boson. It will be treated separately in the next paragraph due to its special role.

Electroweak Symmetry Breaking in the Standard Model

The $\mathbb{SU}_C(3) \times \mathbb{SU}_L(2) \times \mathbb{U}_Y(1)$ symmetry is not a symmetry of the vacuum. E.g. the fact that the $W^{\pm}$ and the Z boson are massive in contrary to the photon breaks this symmetry. The same is true for the Fermionic Sector of the Standard Model. This phenomenon is called Spontaneous Symmetry Breaking. The most elegant way to create it, i.e. to provide particles with mass, is the introduction of the so-called Higgs field, coupling to the other particles of the Standard Model via its excitation quantum, the Higgs boson, as suggested by P. Higgs in 1964 [7]. In the framework of the Standard Model, the Higgs boson must be a non-charged scalar boson. Its existence remains to be experimentally proven yet, but its mass can be inferred from other parameters of the Standard Model, in particular the mass of the top quark via electroweak radiative corrections. The concept of Spontaneous Symmetry Breaking was introduced by Ginzburg and Landau in the context of superconductivity [18].

2.2. The Physics of the Top Quark

In the following, a brief overview of Top Physics at the Tevatron shall be given. The production of the top quark in $t\bar{t}$ pairs is discussed. Thereafter, the properties of the top quark are covered. A more detailed review can be found in [19]. A special focus is placed on the relevance of a precision measurement of the top quark mass, being the subject of this thesis.

2.2.1. Top Anti-Top Pair Production

The top quark was discovered as lately as in 1995 by the DØ and CDF collaborations [8, 9] after its prediction as the electroweak partner of the bottom quark in 1977. In fact, the top quark is the most recently discovered elementary particle, up to the τ-neutrino.

At the Tevatron, the top quark production has so far been observed via the strong interaction in $t\bar{t}$ pairs: $q\bar{q} \to t\bar{t}$ which accounts for 85% (90%) of the total cross section of the process, and $gg \to t\bar{t}$ contributing with 15% (10%). The numbers in parentheses give the corresponding numbers for Tevatron's Run I[5] at $\sqrt{s} = 1.8\,\text{GeV}$. For the Large Hadron Collider, relative contributions of 10 and 90 percent are predicted, respectively. In Fig. 2.1 the corresponding tree level production diagrams are shown.

The total cross section for the strong $t\bar{t}$ production is approximately $\sigma_{t\bar{t}} \simeq 7\,\text{pb}$. A summary of the cross section predicted and measured in Run I and II per-experiment is given in Tab. 2.2.

The cross section for the top quark production is determined by the centre-of-momentum energy of the participating (anti-) quarks and gluons. This energy depends on the one hand on the centre-of-mass energy $\sqrt{s}$ of the $p\bar{p}$ system, and on the other hand on the fraction of the total proton momentum x_i carried by the i-th participating (anti-) quark or gluon in the parton model. With p_p, $p_{\bar{p}}$ being the 4-momenta of the proton and the anti-proton, the effectively

[5] for more details on the Tevatron, its two collider experiments DØ and CDF, the Run I and II refer to Chap. 3.

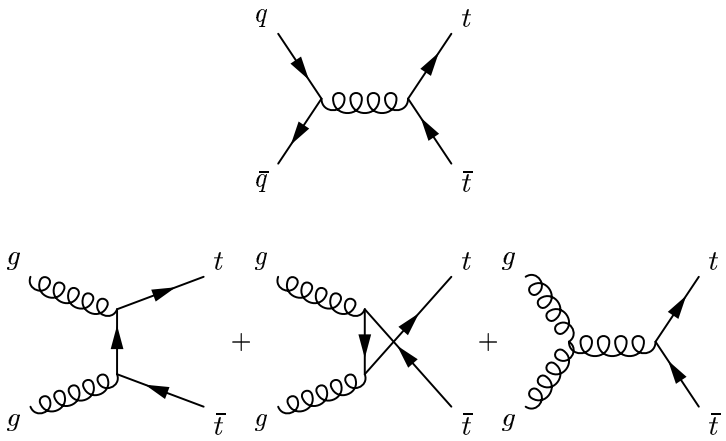

Figure 2.1.: Tree level Feynman diagrams for $t\bar{t}$ production at the Tevatron: quark anti-quark annihilation (85%) in the top row and gluon-gluon fusion (15%) in the t, u, and the s channel going from left to right in the bottom row.

$\sigma_{t\bar{t}}$ [pb]	DØ	CDF	Theory
Run I	5.7 ± 1.6	$6.5\ ^{+\ 1.7}_{-\ 1.4}$	$4.5 - 5.7$
Run II	$7.1\ ^{+\ 1.9}_{-\ 1.7}$	7.3 ± 0.9	$5.8 - 7.4$

Table 2.2.: The total cross section for the strong $t\bar{t}$ production measured by the DØ and CDF experiments in Run I and II of the Tevatron, as summarised in [20]. The Run II figures include published results only. The theoretical prediction was calculated in [21, 22] for a top quark mass of $m_{\text{top}} = 175\,\text{GeV}$.

available centre-of-mass energy $\sqrt{\tilde{s}}$ becomes:

$$\tilde{s} = (x_1 p_p + x_2 p_{\bar{p}})^2 \overset{m_p \to 0}{\simeq} 2 \cdot x_1 x_2 \cdot p_p p_{\bar{p}} = x_1 x_2 \cdot s\,.$$

If for the sake of the argument $x_1 \equiv x_2$ and a top quark mass of $m_{\text{top}} = 175\,\text{GeV}$ are assumed, for the production of a $t\bar{t}$ pair a minimum momentum fraction $x_{\text{min}} \simeq 2 \cdot m_{\text{top}}/\sqrt{s} = 0.18$ is required.

In Fig. 2.2 (left) the Parton Distribution Function (PDF) set is shown in version CTEQ5L for the various parton flavours [23]. These PDF's are used with the $370\,\text{pb}^{-1}$ dataset and the `p14` version of DØ software (Chap. 4). The parton distribution function $f(x)$ gives via $xf(x)\mathrm{d}x$ the probability for a parton to carry a momentum fraction between x and $x + \mathrm{d}x$.

Besides the dependence on the centre-of-mass energy available, the $t\bar{t}$ production cross section depends on the top quark mass. This relation is depicted in Fig. 2.2 (right), as calculated in [21, 22].

The Dilepton Decay Channel

According to the Standard Model and assuming 3 quark generations, the top quark predominantly decays into its weak interaction partner, the bottom quark, with a branching ratio $f_{\text{BR}}(t \to Wb) > 0.998$ [20]. This is due to the fact that $|V_{tb}| \simeq 1$, as follows from the unitarity

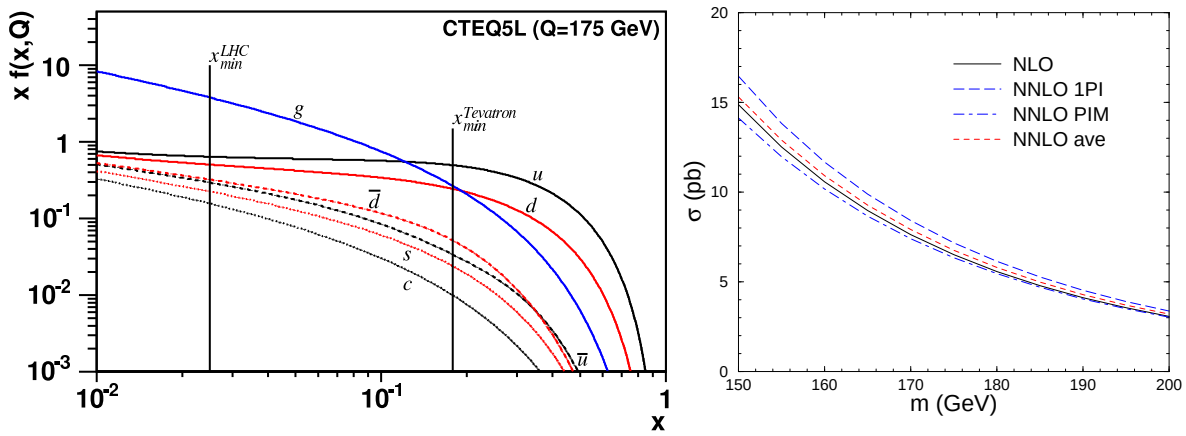

Figure 2.2.: The Parton Distribution Function (PDF) set CTEQ5L at the scale $Q^2 = 175\,\mathrm{GeV}$, as determined by the CTEQ collaboration [23] is shown on the left hand side. The minimum momentum fraction x_{min} bands defined in the text are marked as vertical lines for Tevatron and LHC centre-of-mass energies. On the right hand side the dependence of the total $t\bar{t}$ cross section on the top quark mass as in [21, 22] is shown.

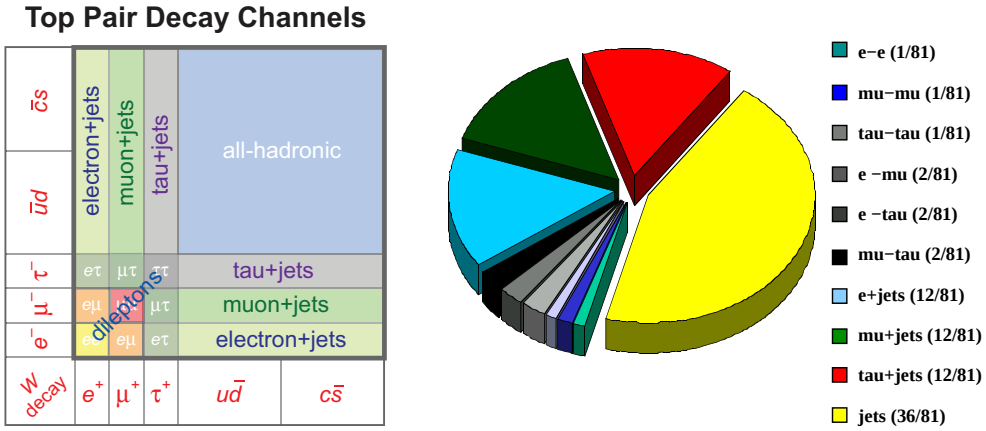

Figure 2.3.: On the left hand side a summary of the decay subchannels of a $t\bar{t}$ pair is given. The right hand side displays the relative contributions at Born level. The τ-inclusive contribution of the dilepton channel is approximately 5%.

of the CKM matrix and the measurement of its other elements. Each of the W-bosons can subsequently decay leptonically ($f^{e}_{\mathrm{BR}} = 10.72 \pm 0.16$, $f^{\mu}_{\mathrm{BR}} = 10.57 \pm 0.22$, $f^{\tau}_{\mathrm{BR}} = 10.74 \pm 0.27$; 1/9 each at Born level, all numbers are from [20]) or hadronically ($f^{\mathrm{hadrons}}_{\mathrm{BR}} = 67.96 \pm 0.35 \simeq 3 \cdot 2/9$ at Born level, where the number 3 accounts for the number of strong colour charges and 2 is the number of quark generations available for W decay regarding energy conservation). This defines three decay channels for a $t\bar{t}$ pair: the dileptonic channel, being the subject of this thesis, where both W-bosons decay leptonically, the semileptonic channel where one W decays leptonically and the other hadronically, and the all-jets channel, where both W-bosons decay hadronically.

The decay channels of a $t\bar{t}$ pair are listed schematically on the left hand side of Fig. 2.3, their relative contributions are shown in a pie chart on the right hand side. However, the τ-leptons have a short life time and are not detected directly. Therefore, the dilepton channel is understood to be defined with either 2 electrons, 2 muons, or an electron and a muon in the final state.

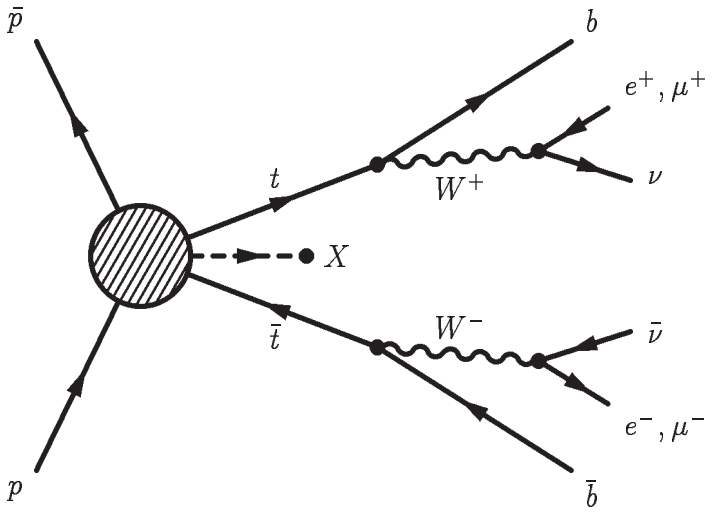

Figure 2.4.: Tree level Feynman diagram for the simplest $t\bar{t}$ decay scenario into the dilepton channel.

These final states include leptonic decays of the τ-lepton: $\tau \to e$ ($f_{\mathrm{BR}} = 17.84 \pm 0.06$) and $\tau \to \mu$ ($f_{\mathrm{BR}} = 17.36 \pm 0.06$). Taking this into account, the branching ratios in the dilepton channel are:

Channel	Process (incl.)	f_{BR} [%], from [20]
$e\mu$:	$t\bar{t} \to e^{\pm}\mu^{\mp}b\bar{b}\nu's$	3.16 ± 0.06
ee:	$t\bar{t} \to e^{+}e^{-}b\bar{b}\nu's$	1.58 ± 0.03
$\mu\mu$:	$t\bar{t} \to \mu^{+}\mu^{-}b\bar{b}\nu's$	1.57 ± 0.03

The total contribution of the dilepton channel including leptonic τ-decays is 6.3%. However, the dilepton channel is very important. Due to the two leptons and fewer jets in the final state, it potentially has the lowest systematic error of all $t\bar{t}$ decay channels and will provide a top quark mass measurement of a similar precision as the semileptonic channel once a certain integrated luminosity is collected. Further, New Physics which is not visible in other decay channels may be found in the dilepton channel. Additionally, precision measurements can be made in the dilepton channel to test the Standard Model.

The basic signature of a dileptonic $t\bar{t}$ event is evident from the tree level Feynman diagram in Fig. 2.4, which represents the simplest decay scenario without any τ-leptons or any initial/final state radiation:

$$q\bar{q},\, gg \to t\bar{t} + X \to l^{-}\bar{\nu}\bar{b}l^{+}\nu b + \tilde{X}\,,$$

where $X, \tilde{X}$ are any additionally produced particles. Thus, as a signature, one expects 2 leptons and 2 b-jets. All 4 physics objects should have a high p_T and be central (i.e. have a low $|\eta|$) due to the high mass of a $t\bar{t}$ pair and the fact that its rest frame almost coincides with the rest frame of the detector. This can be seen from steeply falling parton distribution functions, which makes equal momentum fractions for both partons probable. Due to a b-jet fragmentation as well as possible initial and final state radiation the 2 jet bin is understood to be inclusive. Further, large $\not\!\!E_T$ values are expected due to 2 or more neutrinos. The background processes to mimic this signature are discussed in Sec. 2.3.

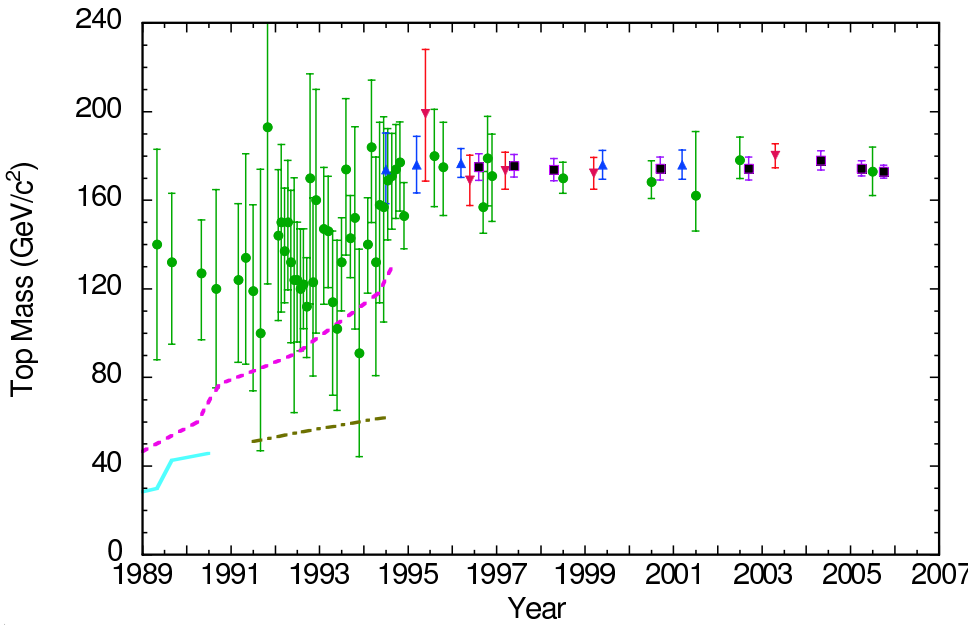

Figure 2.5.: Evolution of the top quark mass prediction from electroweak precision data (●) and direct measurements (CDF: ▲, DØ: ▼) with time. The world average from direct measurement is shown as ■. Furthermore, the lower bounds from hadron colliders (dashed lines) and e^+e^- colliders (solid line) are presented. (Updated: Sept. 2005 by Chris Quigg from [24]).

2.2.2. Properties of the Top Quark

Top Quark Mass

The top quark mass is a fundamental parameter of the Standard Model. The importance of its precision measurement will be detailed in the following. Currently, the world average top quark mass including preliminary results is [10]:

$$m_{\text{top}}^{\text{publ.+prel.}} \quad = \quad 171.4 \pm 2.1\,\text{GeV}(\text{stat.} + \text{syst.})\,.$$

Before the direct measurement by both Tevatron collider experiments in 1995 [8, 9], the top quark mass has been inferred using the Standard Model prediction manifest in radiative corrections to the W-boson mass with electroweak precision data. The theoretical background is briefly outlined in the following. In Fig. 2.5 the evolution of the top quark mass is shown [24].

To leading order, the electroweak interaction depends solely on a set of 3 independent parameters. Conveniently, these three parameters are chosen to be the electromagnetic coupling constant α which is precisely measured in low-energy experiments, the Fermi constant G_F determined in weak decay experiments, and the mass of the Z boson m_Z measured at LEP with a high precision. With these parameters, the mass of the W boson can be expressed as:

$$m_W^2 = \frac{\frac{\pi\alpha}{\sqrt{2}G_F}}{\sin^2(\theta_W)}\,, \tag{2.1}$$

where $\sin^2(\theta_W) := 1 - \frac{m_W^2}{m_Z^2}$ defines the Weinberg angle θ_W.

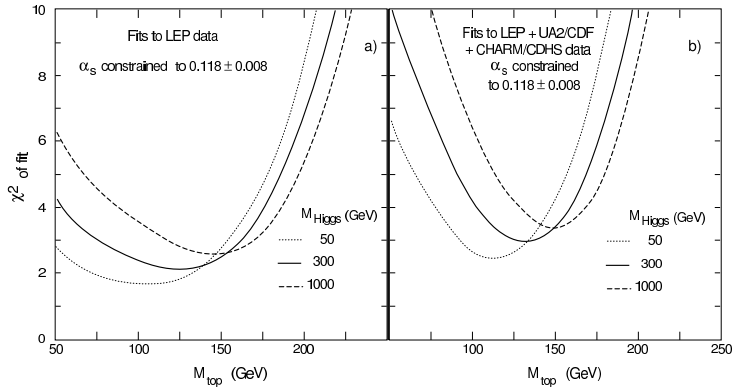

Figure 2.6.: The χ^2 of the Standard Model fit to the electroweak precision measurements as a function of the top quark mass using the data of LEP I only (left) and data from LEP, neutrino and hadron collider experiments (right) [25]. The curves are displayed for 3 Higgs boson masses: 50 GeV (the limit from direct searches at LEP I), 300 GeV, and 1000 GeV (the upper limit allowed by the theoretical framework of the Standard Model). The minima of these curves are close together due to the logarithmic dependence on the Higgs mass, whereas the top quark mass enters quadratically.

With loop corrections in next-to-leading order included, contribution to the self-energy of the W-boson stemming from the virtual top quark and the Higgs boson are to be included, and Eqn. 2.1 modifies to:

$$m_W^2 = \frac{\frac{\pi\alpha}{\sqrt{2}G_F}}{\sin^2(\theta_W)(1-\Delta r)}\,,$$

where Δr represents the next-to-leading order corrections. These corrections to the W and Z boson mass originate from the following Feynman diagrams:

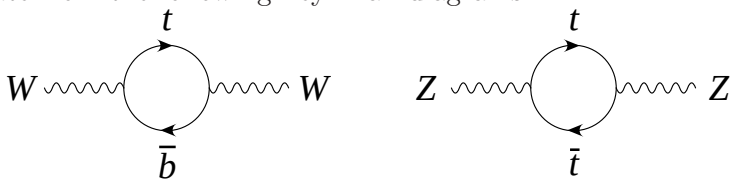

and yield:

$$(\Delta r)_{\text{top}} \simeq -\frac{3G_F}{8\sqrt{2}\pi^2 \tan^2\theta_W} \cdot m_{\text{top}}^2\,. \tag{2.2}$$

For the Higgs boson, the virtual corrections

result in logarithmic contributions due to the different loop type which accounts for the scalar nature of the Higgs boson. Numerically, the correction is:

$$(\Delta r)_h \simeq \frac{11G_F m_Z^2 \cos^2\theta_W}{24\sqrt{2}\pi^2} \cdot \ln\frac{m_h^2}{m_Z^2}\,. \tag{2.3}$$

It is important to stress, that the contribution of Eqn. 2.2 is quadratic, whereas the contribution of Eqn. 2.3 is logarithmic and thus rather weak. Therefore, the top quark mass contributes much stronger to the self-energy of weak bosons than the Higgs boson. This instance was successfully

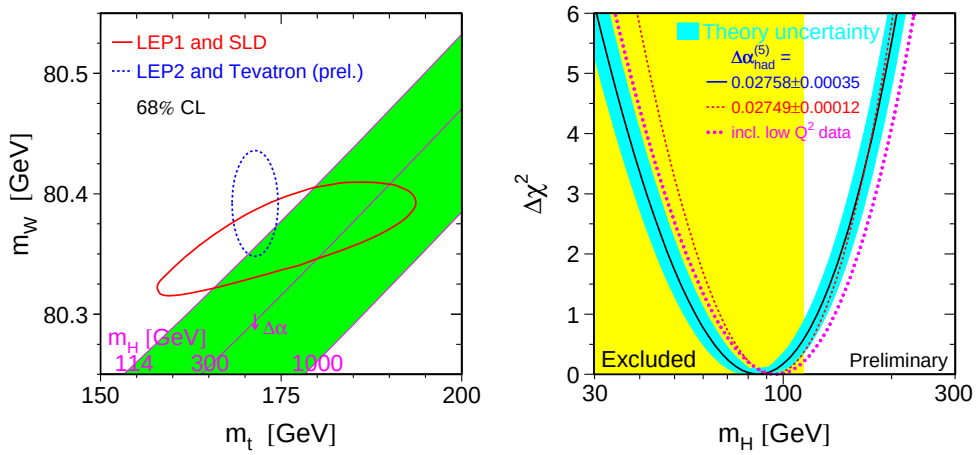

Figure 2.7.: The left hand side shows the lines of constant Higgs mass for 114, 300, and 1000 GeV in the W-boson mass versus top quark mass plane. Further, as a dotted ellipse, the 68% confidence level for the direct measurements of m_W and m_{top} is shown. The solid ellipse is the 68% confidence level for the indirect measurement of m_W and m_{top} from precision electroweak data. The right hand side demostrates the so-called Blueband plot, showing the Higgs boson mass as determined from electroweak precision data together with the 95% confidence level lower limit from direct searches. The yellow region marks Higgs masses exclueded with LEP direct search results [28]. Both plots are from [29].

used to predict the top quark mass using electroweak precision measurements, as shown in Fig. 2.6 [25]. It is remarkable, that in 1992, 3 years before the discovery of the top quark, its mass was predicted with a relatively high precision and fully confirmed later. The most recent indirect measurements of the top quark mass yield [26, 27]:

$$m_{\text{top}} = 179.4\ ^{+12.1}_{-\ 9.2}\,\text{GeV}\,,$$

and are in a good agreement with the world average top quark mass.

Now, after the discovery of the top quark and the precision measurement of its mass (which is constrained to 1.2% regarding the world average top quark mass including published and preliminary results [10]), the mass of the elusive Higgs boson can be predicted from the precision measurement of the W-boson mass. For the Run II of the Tevatron, for the the W-boson mass an uncertainty of 20 MeV is expected. In terms of the projected uncertainty on the Higgs boson mass, this corresponds to an error on the top quark mass of $\sim$3 GeV. This goal has already been overachieved. The left hand side of Fig. 2.7 shows the W-boson mass versus top quark mass plane, with lines of constant Higgs boson masses at 114 GeV (values of under 114.4 GeV have been excluded by LEP [28]), 300 GeV and 1000 GeV (excluded as the limit of validity of the Standard Model). As a dotted ellipse the direct measurements of the top quark and W-boson mass are shown, the solid ellipse represents electroweak precision data results. It can be clearly seen that these measurements favor a light Higgs mass. The plot on the right hand side of Fig. 2.7 shows the Higgs mass prediction from all electroweak precision data together with the 95% confidence level lower limit from direct searches. This fit yields 85^{+39}_{-28} GeV [29] for the Higgs mass which is slightly below the limit excluded in the direct search for a Standard Model Higgs at LEP.

The Decay Width of the Top Quark

Due to its large mass, the top quark has a very short life time of $\tau_{\text{top}} \simeq 0.5 \times 10^{-24}\,\text{s}$ or, alternatively, a decay width of $\Gamma_{\text{top}} \simeq 1.5\,\text{GeV}$ [30]. This makes the top quark an interesting study object, since it is the only known quark with a life time lower than the hadronisation time scale $\mathcal{O}(10^{-23}\,\text{s})$, estimated by $\Lambda_{\text{QCD}}^{-1} \simeq 200^{-1}\,\text{MeV}^{-1}$. This means that the top quark decays via the weak interaction before it hadronises and that no bound states like $t\bar{q}$ etc. can be formed. Therefore, by measuring the final state in the detector the physics properties of a "naked" quark can be studied for the first time in the history of Elementary Particle Physics. In particular, this is true for quantum numbers of the top quark like the spin.

W-Helicity Measurements

The preserved spin information of the top quark provides a unique possibility to verify the $V-A$ nature of the Wtb coupling. As a fermion, the bottom quark must be left-handed in the massless limit, which forbids right-handedness for the W-boson: then the total angular momentum would be 3/2 in the top rest frame, whereas the Standard Model top quark has spin 1/2. Therefore, a measurement of the fraction f_+ of right-handed W-bosons is an important test of the Standard Model. For the fraction of longitudinally polarised W-bosons

$$f_0 = \frac{m_{\text{top}}^2/2m_W^2}{1 + m_{\text{top}}^2/2m_W^2} \simeq 70\%$$

according to the Standard Model. Various approaches are used at DØ and CDF to measure the fractions f_0, f_+, and f_-. The latest Run II results are:

$$\begin{array}{lcll} f_+ & < & 0.24\ (95\%\ \text{CL}) & (\text{DØ, [31, 32]}) \\ f_+ & < & 0.27\ (95\%\ \text{CL}) & (\text{CDF, [33]}) \\ f_0 & = & 0.74\ ^{+0.22}_{-0.34} & (\text{CDF, [33]})\,. \end{array}$$

Spin Correlations of $t\bar{t}$ Pairs

Since the top quark decays before hadronisation due to its large mass, its spin is experimentally accessible. The beams at the Tevatron are not polarised. However, the spin information can be inferred from the correlation of the t and the $\bar{t}$ in strong top pair production. For the dilepton channel, the relevant angular distribution of charged leptons coming from the top and the anti-top is

$$\frac{1}{\sigma}\frac{\text{d}^2\sigma}{\text{d}(\cos\theta_+)\text{d}(\cos\theta_-)} = \frac{1 + \kappa \cdot \cos\theta_+ \cos\theta_-}{4}\,,$$

where θ_+, θ_- are the angles of the charged leptons with respect to a particular quantisation axis in the top rest frame, at the Tevatron conveniently chosen to be the beamline axis. For a centre-of-mass energy of $\sqrt{s} = 1.96\,\text{GeV}$ ($\sqrt{s} = 1.8\,\text{GeV}$), the correlation coefficient κ is expected to be $\kappa \simeq 93\%$ (88%) [11, 20, 19]. DØ has measured the spin correlation using dilepton events in Run I [34], and found a weak preference for the Standard Model prediction. A limit of $\kappa > -0.25$ is quoted at 68% confidence level. In Run II of the Tevatron, an observation of spin correlations is expected, and at DØ efforts are underway [11].

Electric Charge of the Top Quark

The electric charge of the top quark is measured at the Tevatron in order to exclude a non-Standard Model quark Q_4 with a charge of $-4/3$ and the $Q_4 \to W^- b$ decay mode. This t-Q_4 ambiguity is present at both Tevatron collider experiments, since the pairing of the b-quarks and the W-bosons is not determined in the strong top quark production $p\bar{p} \to t\bar{t} \to W^+W^-b\bar{b}$. Canonically, the charge of the top quark could be easily accessed at an e^+e^- collider by measuring the ratio $R = \frac{e^+e^- \to \text{hadrons}}{e^+e^- \to \mu^+\mu^-}$ below and above the top quark production threshold. At the Tevatron, different approaches have to be taken: either the charge of the decay products, or the photon radiation rate has to be determined in $t\bar{t}$ events. So far, the top quark charge has been investigated by DØ only and the Q_4-scenario can be ruled out at 94% level [35].

2.3. Background Processes

The main *background physics processes* contributing in all three dileptonic channels are:

- Drell-Yan: $Z/\gamma^* \to \tau\bar{\tau} \to l_1\bar{\nu}_{l_1}\bar{l}_2\nu_{l_2}$, where $l_i = e, \mu$, with two or more associated jets from initial or final state radiation.
- Di-boson production: $W^+W^- \to l_1\bar{\nu}_{l_1}\bar{l}_2\nu_{l_2}$, again with two associated jets. The yields for the WZ and ZZ processes are an order of magnitude lower [36, 37]. Therefore, they are not considered in this analysis.

Due to the presence of neutrinos, the processes above contain real[6] missing energy $\not\!\!E_T$.

One has to consider, especially for the ee and $\mu\mu$ channels, another class of background events, the so-called *instrumental background* events. These are physics processes where a physics object is mis-measured, for example $\not\!\!E_T$, due to its finite resolution or mis-reconstruction.

The by far largest contribution to the instrumental background comes from $Z/\gamma^* \to e\bar{e}, \mu\bar{\mu}$ with associated jets. The final yield of these processes is comparable to $Z/\gamma^* \to \tau\bar{\tau}$, since the low probability for a mis-measurement of the Gaussian distributed $\not\!\!E_T$ in $Z/\gamma^* \to e\bar{e}, \mu\bar{\mu}$ is compensated by a branching ratio of unity for $e \to e$, $\mu \to \mu$, whereas $\tau \to e = 17.84\%$, $\tau \to \mu = 17.36\%$ [20] for $Z/\gamma^* \to \tau\bar{\tau}$.

Another significant source of instrumental background in all 3 channels is the production of multijet final states (QCD multijet background). So for instance an electron can be faked by a π^0, and a secondary muon coming from within a jet can be isolated and thus survive the selection cuts due to mis-reconstruction.

[6] "Real" in this context refers to "not faked".

3. Experimental Setup

The data used for the top quark mass measurement in the dilepton channel presented in this thesis originates from the DØ experiment at the Tevatron – a proton-antiproton collider hosted by the Fermi National Accelerator Laboratory in the vicinity of Chicago, USA.
The DØ experiment [38] is a multi-purpose, nearly hermetic detector aimed at studying high transverse momentum physics with an emphasise on the identification of leptons and jets.
The Tevatron [39] is at present the world's highest energy collider [20], featuring a centre of mass energy of $\sqrt{s} = 1.96\,\text{TeV}$.

DØ and CDF, the two collider experiments at the Tevatron, have collected an integrated luminosity[1] of approx. $\int \mathrm{d}t\,\mathcal{L} = 125\,\text{pb}^{-1}$ at a centre of mass energy of $\sqrt{s} = 1.8\,\text{TeV}$ during the data taking period ranging from 1992 to 1996, denoted as Run I. The highlight of the Run I was the discovery of the top quark in 1995 and a preliminary mass measurement by both DØ [8] and CDF [9] and later the precise measurement of its mass [40, 41, 42].

Between 1996 and 2001, the Tevatron and its two main experiments have been significantly upgraded. In March of 2001 a new data taking period, Run II, has begun. Until the shutdown in March 2006 approx. $1.2\,\text{fb}^{-1}$ of data were collected. Besides the discovery of the top quark and insights into its properties, the Run I and II physics programs yielded a precision measurement of the mass of the W boson, new insights into B-physics, detailed analyses of gauge boson couplings and studies of jet production. Further, they improved the limits on characteristic quantities of New Physics like leptoquarks and SUSY.

In spring of 2006, the DØ detector went through several upgrades, the major one being the installation of an additional layer (Layer 0) to the silicon tracker, which will help to improve the track reconstruction and the b-tagging capabilities.

In the following, the Fermilab accelerator complex and the DØ detector will be described in turn.

3.1. The Fermilab Accelerator Complex

The Fermilab accelerator complex is a series of machines, the most powerful being the Tevatron – a $p\bar{p}$ collider with a centre of mass energy of $\sqrt{s} = 1.96\,\text{TeV}$. They are schematically displayed in Fig. 3.1. In the following, the Tevatron [39] and each of its 7 pre-accelerators will be described.

The protons used for operating the Tevatron come from a hydrogen source, which delivers single negatively charged hydrogen ions. These are brought to 750 keV energy by a Cockroft-Walton

[1] the integrated luminosity values given in this section are understood to be per experiment.

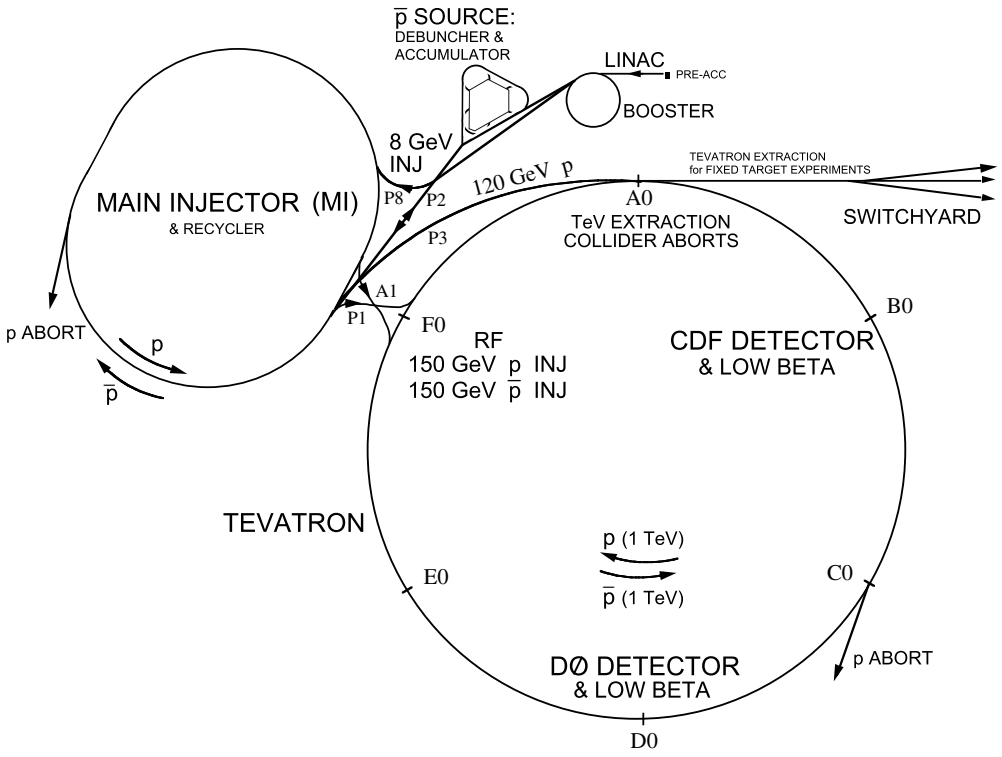

Figure 3.1.: A schematic display of the Fermilab accelerator complex

accelerator, from which they are injected into a LINAC (LINear ACcelerator), where their energy is increased to 400 MeV. From the LINAC, the negatively charged hydrogen atoms are stripped off their two electrons by shooting them through a thin graphite window. This is a widely used technique in linear accelerators to increase the energy gain by using the electric potential difference twice. In the next step, the produced protons are fed into the Booster, a synchrotron which brings their energy to 8 GeV. From the Booster, the protons are sent into the Main Injector to be accelerated to 150 GeV and get the Tevatron collision mode time structure. It consists of 36 bunches with a spacing of 396 ns, which are grouped into 3 superbunches (of 12 bunches each) with a time gap of 2 μs between them. Finally, the protons are either injected into the Tevatron or are used for the production of antiprotons. In the first scenario they are accelerated to 980 GeV while their populated parameter space is decreased by low-beta quadrupoles. After that, the particles are stored for a time in the order of 1 day.

The anti-proton production chain is begun by the second scenario for protons in the Main Injector: they are shot on a nickel-copper target and produce, among other particles, antiprotons. The target material is optimised for this purpose, and the energy/momentum spectrum of $\bar{p}$'s produced in the mean field of the lattice peaks at 8 GeV. The secondaries are focused by a solenoidal magnetic field produced by a lithium coil driven by a current of $\sim$650 kA. Subsequently, a pulsed dipole magnet selects 8 GeV negatively charged particles. In the next step they are fed into the Debuncher and the Accumulator. The purpose of the Debuncher is to reduce the momentum spread by applying stochastic cooling techniques. In the Accumulator, the produced antiprotons are stacked for the next "store" – a collision-mode run of the Tevatron. Accumulating the typical $\bar{p}$ number of $\sim 10^{12}$ takes several hours. At the beginning of each new

store, the antiprotons are transferred from the Accumulator to the Main Injector, where they are accelerated in the same way as the protons, described above.

The production efficiency for antiprotons, being $\sim 10^{-5}$, is the main limiting factor for the Tevatron luminosity. The increasing ability to control the production process is responsible for the consequent rise of the initial store luminosity in recent years.

At the Tevatron accelerator, six interaction points are marked for proton-antiproton collisions, with the DØ and CDF experiments situated at the D0 and B0 interaction points, respectively.

3.2. The DØ Detector

The DØ detector is a general-purpose, nearly hermetic detector aimed at studying high transverse momentum physics at the Tevatron with an emphasis on the identification of leptons and jets [38]. It weighs 5500 tons and measures 13 m × 11 m × 17 m (height × width × length). The design was first proposed in 1983 and this initial version of the detector was collecting data between 1992 and 1996, the so-called Run I. A full description of Run I DØ detector can be found in [43]. Its significant contribution to modern high energy physics peaked in the discovery of the top quark together with the CDF collaboration in 1995 [8, 9].

The DØ detector [38] has undergone major upgrades for Run II [44, 45], to accommodate the decrease in bunch spacing from 3.56 μs in Run I to 396 ns in Run II. Figure 3.2 shows a schematic side view of the Run II DØ detector.

The upgraded DØ detector consists of three primary detector systems as one moves from inside to outside: inner tracker, calorimeter, and muon system. The inner tracking system has been completely replaced, and sits inside a 2 T magnetic field provided by a super-conducting solenoid, allowing for charge and transverse momentum measurement of the particles produced, and also for b-tagging. The calorimeter remains unchanged, new readout electronics have been installed and the data acquisition system has been upgraded. A preshower detector has been added between the solenoid and the calorimeter (CPS – Central PreShower detector) to compensate for the upstream energy loss in the solenoid and to improve electron identification and e/π rejection by minimising the energy escaping from the electromagnetic section of the calorimeter. Another preshower detector (FPS – Forward PreShower) was installed in front of the end-cap section of the calorimeter. A new luminosity monitoring system has been added to the detector. The muon system has been partially replaced on both hardware and readout side to improve the coverage and to increase the precision of the momentum measurement, as well as to provide a fast muon trigger. A new, faster and more sophisticated 3-level trigger system and data acquisition system with a 50 Hz rate-to-tape are used to cope with the increased luminosity environment.

The Tevatron defines a Cartesian right-handed coordinate system canonically used in collider accelerators: with the z-axis along the proton beam direction and the x-axis pointing towards the centre of the ring. As common in hadron collider detectors, at DØ polar coordinates are

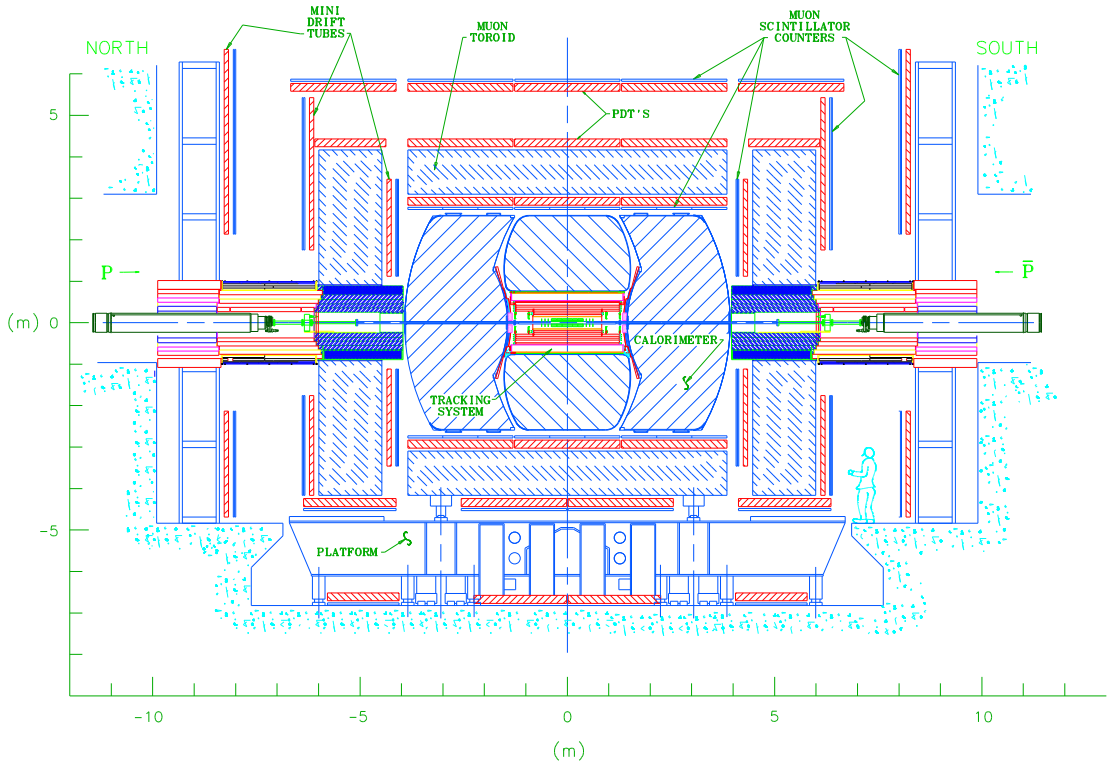

Figure 3.2.: Isometric view of the DØ detector showing the three main systems: the central tracking and vertexing detector, the calorimeter, and the muon system.

used:

$$\begin{aligned} r &= \sqrt{x^2+y^2}\,, \\ \phi &= \arctan\frac{x}{y}\,, \\ \eta &= -\ln\tan\frac{\theta}{2}\,, \qquad \text{where } \cos\theta = \frac{z}{\sqrt{x^2+y^2+z^2}}\,. \end{aligned}$$

The variable η is called pseudorapidity. In the massless limit for a given particle, i.e. $\gamma \gg 1$ and $p \to E$, the rapidity y defined as

$$y := \frac{1}{2}\ln\frac{E+p_z}{E-p_z}\,,$$

approaches the pseudorapidity. The main advantage for the use of η is that in minimum bias[2] proton anti-proton collisions the particle multiplicity is constant in y for a given interval Δy. In the following, η measured with respect to the interaction point will be referred to as physics-η, and to the detector centre as detector-η. In general, $\eta_{\text{phys}} \neq \eta_{\text{det}}$, as the interaction area is spread around the centre of the detector, with a width of $\sigma_z \simeq 28\,\text{cm}$ in the direction of the beam axis [46].

[2]Minimum bias events are events collected without any trigger requirement.

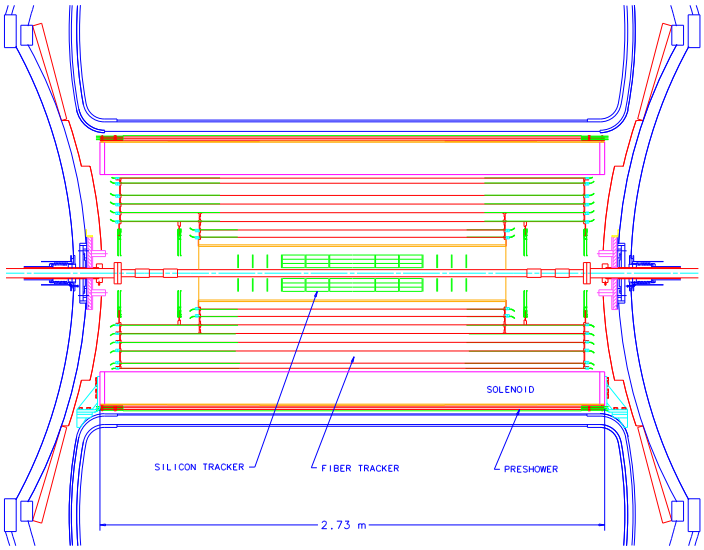

Figure 3.3.: Isometric view of the DØ detector tracking system with its three main components: the SMT, the CFT and the solenoid.

3.2.1. The Tracking System

The tracking system consists of 3 major components: the SMT (Silicon Microstrip Tracker) – a silicon vertex detector, the CFT (Central Fibre Tracker) – scintillating fibres in coaxial cylinder mantles and a solenoid magnet, in order of increasing radius. With such a setup, the momentum of charged particles can be measured: their trajectories are bent around the z axis by virtue of the magnetic field, and become a helix. The bending radius is directly proportional to the transverse momentum p_T of the particles:

$$r\,[\mathrm{m}] = \frac{p_T\,[\mathrm{GeV}]}{0.3 \cdot B\,[\mathrm{T}]} \tag{3.1}$$

where p_T is conveniently defined as:

$$p_T := \sqrt{p_x^2 + p_y^2}\,.$$

This definition makes sense, since this is the only meaningful component of the momentum vector for a given interaction in a hadron collider, where the total p_z of the event remains undetermined due to the constituent structure of the proton. For a single particle in the final state, however, a p_z component is provided by the measurement of η. The tracking system is shown in Fig. 3.3.

Tracking performance

From the Eqn. 3.1 follows, that the uncertainty on the transverse momentum measurement σ_{p_T} is proportional to the inverse of the momentum p_T^{-1}. More precisely, the relation holds:

$$\frac{\sigma_{p_T}}{p_T} = C \cdot p_T \oplus S\,, \tag{3.2}$$

where S accounts for the multiple scattering term and C represents the resolution term. The parameters used in this analysis are given in Chap. 5.

The Silicon Microstrip Tracker

The part of the tracker closest to the designed interaction point is the SMT [46]. It is used to reconstruct the tracks of particles produced in a collision with a high precision, due to a high spatial resolution of its layers. This allows for a precise momentum measurement, the ability to cope with high particle multiplicities and b-tagging. As the name says, the SMT system is made of silicon microstrip detectors of 300 μm wafers mounted around the beampipe in barrel and disk geometries. Refer to Fig. 3.4 for a 3-dimensional visualisation. This design is motivated by the fact, that the interaction region is Gaussian distributed along the z-axis with respect to the detector centre with $\sigma_z \simeq 28\,\text{cm}$. With such a setup, most of the tracks are perpendicular to the surfaces of the silicon microstrip wafers for any point of the interaction region. For low η, tracks are reconstructed predominantly with the barrels, and for high η with the disks.

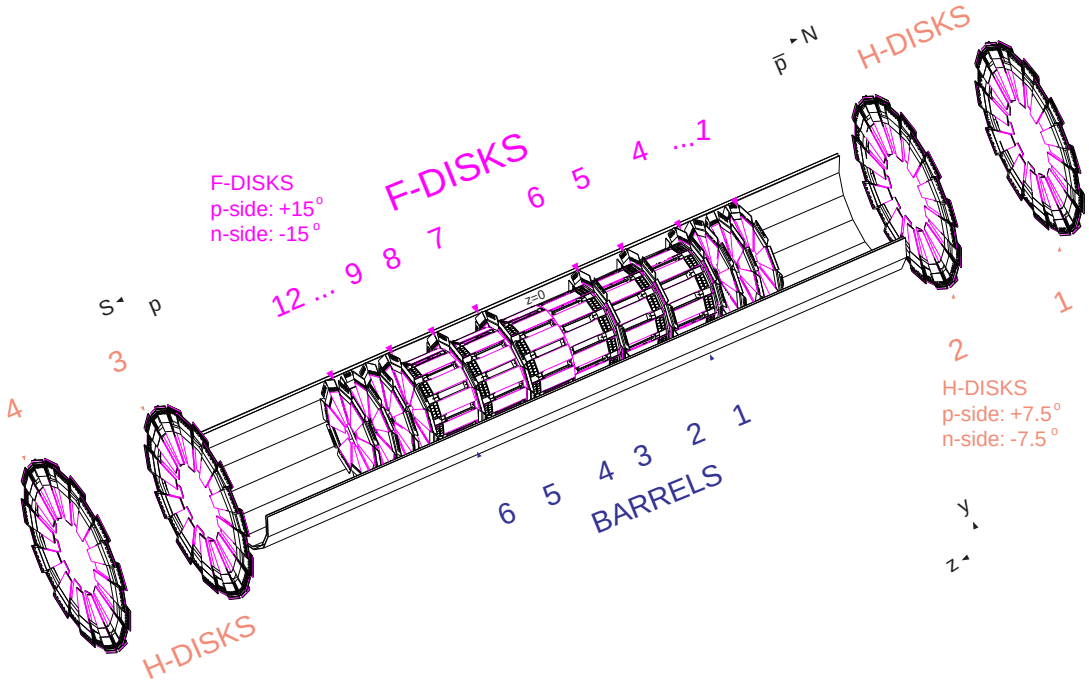

Figure 3.4.: Three dimensional view of the SMT together with beryllium bulkheads and carbon fibre support structure.

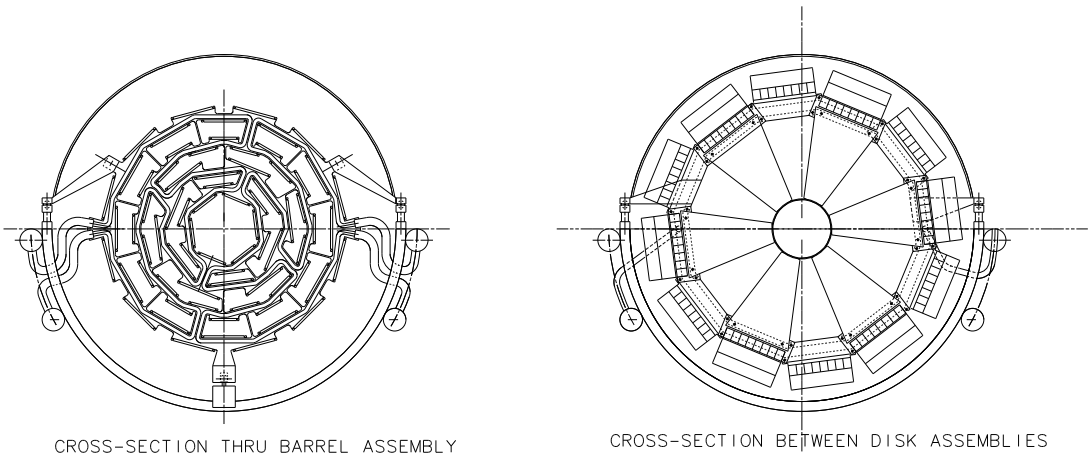

Figure 3.5.: Cross sectional view on the Silicon Vertex Detector. **Left:** Barrel, **right:** F-disk.

There are 6 barrel sections, each 12 cm long and containing 4 layers. See Fig. 3.5 for a cross sectional view. The first and the third layers of the inner 4 barrels are double wafers with their microstrip structures rotated by 90° to each other with pitches of 50 μm for axial strips and 153.5 μm for radial ones. The two outer barrels have single wafers with an axial pitch of 50 μm in layers 1 and 3. The second and fourth layer in all barrels are double-sided, having axial and 2 stereo strips, with 50 μm and 62.5 μm pitch, respectively. This combination of rectangular and small angle stereo allows a good pattern recognition and a good separation of primary vertices for events with several interactions. The spatial resolution for the barrels in $r\phi$ is approximately $\sim 10\,\mu$m , and in z about 40 μm for 90° stereo detectors.

In the SMT central region, the barrels are interspersed with F-disks (Fig. 3.5), which consist of 6 wedges of double-sided detectors with ±15° stereo strips at 50 μm and 62.5 μm pitch, respectively. At the outer ends of the SMT there are two H-disks, which have larger radii and cover high-η regions. They consist of 12 double sided wedges with ±7° stereo strips and a 80 μm pitch.

Averaged over the SMT and the integration region, the approximate vertex resolution is:

$$\begin{aligned} \sigma^{r\phi}_{\text{vtx}} &\simeq 40\,\mu\text{m} \\ \sigma^{rz}_{\text{vtx}} &\simeq 100\,\mu\text{m} \ . \end{aligned}$$

The Scintillating Fibre Tracker

The next downstream component of the tracking system is the CFT [47]. It covers a region of $|\eta_{\text{det}}| < 2.0$ and is based on scintillating fibre technology with a Visible Light Photon Counter (VLPC) readout. The CFT consists of 8 coaxial layers, see Fig. 3.6. Each of them features 2 fibre doublets in zu or zv configuration, where z stands for axial fibres, and u, v for ±3° stereo fibres. Each doublet consists of 2 layers with 830 μm diameter fibres with an average spacing of 870 μm depending on the layer, offset by approximately half the spacing.

The scintillating fibres are cladded with normal plastic featuring a low refraction index to minimise optical total reflection losses on their surface. They are supported on carbon fibre cylinders.

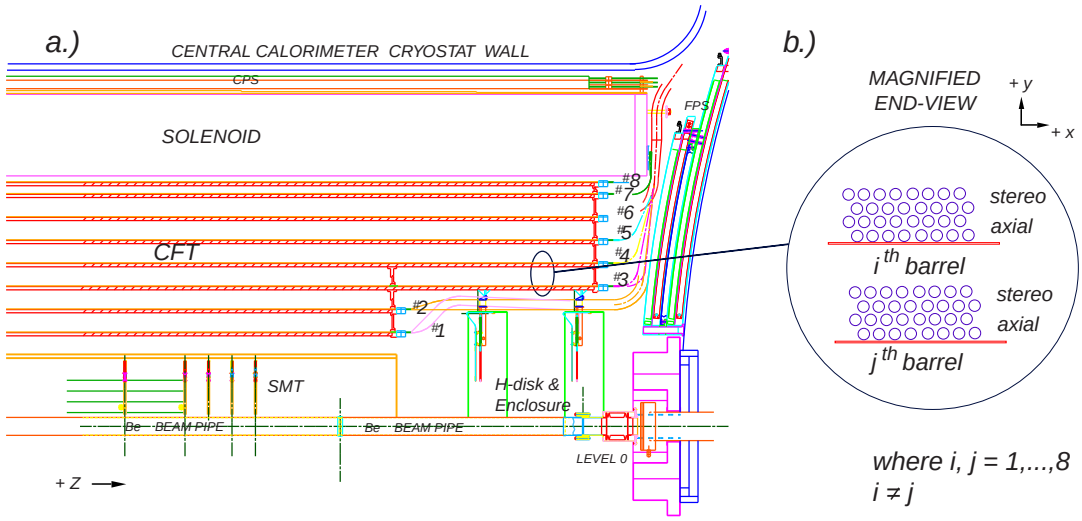

Figure 3.6.: Cross sectional view in rz-plane of the CFT with symbolic layer details

This setup provides a good efficiency and a position resolution of

$$\sigma_{r\phi} \simeq 100\,\mu\text{m} \quad .$$

The fibres are up to 2.5 meters long and the light is piped out by clear fibres of 7-11 m length to the VLPC's, which are maintained at 9 K in a cryostat outside of the tracking volume. The VLPC's are solid state devices with a pixel size of 1 mm, the same as the fibre diameter. They feature a fast rise time, a rate capability of 40 MHz, a high gain of 40,000 electrons for one converted photon and a high quantum efficiency of 70%. The CFT has a total of about 77,000 channels.

The Solenoid

The solenoid magnetic field of 2 T inside of the tracking system is provided by a superconducting magnet 2.73 m in length and 1.42 m in diameter. Its uniformity is better than 99.5%, which is ensured by higher currents at the end of the coil. It is wound with two layers of multifilamentary Cu:NbTi wires stabilised with aluminium. The thickness of the magnet is slightly less than 1 radiation length[3] X_0.

3.2.2. The Calorimeter

The DØ Calorimeter [48] is a sampling liquid argon calorimeter with depleted uranium as sampling material. Its main role is to measure the energy and direction of final state particles. Further, it is crucial for the identification of electromagnetic objects – electrons and photons, as well as hadronic ones – jets and pions. From the imbalance of the transverse energy E_T the presence of neutrinos and other non-interacting particles can be inferred.

[3] X_0 is defined as the distance, where on average electron energy is reduced to $1/e \cdot E_0$.

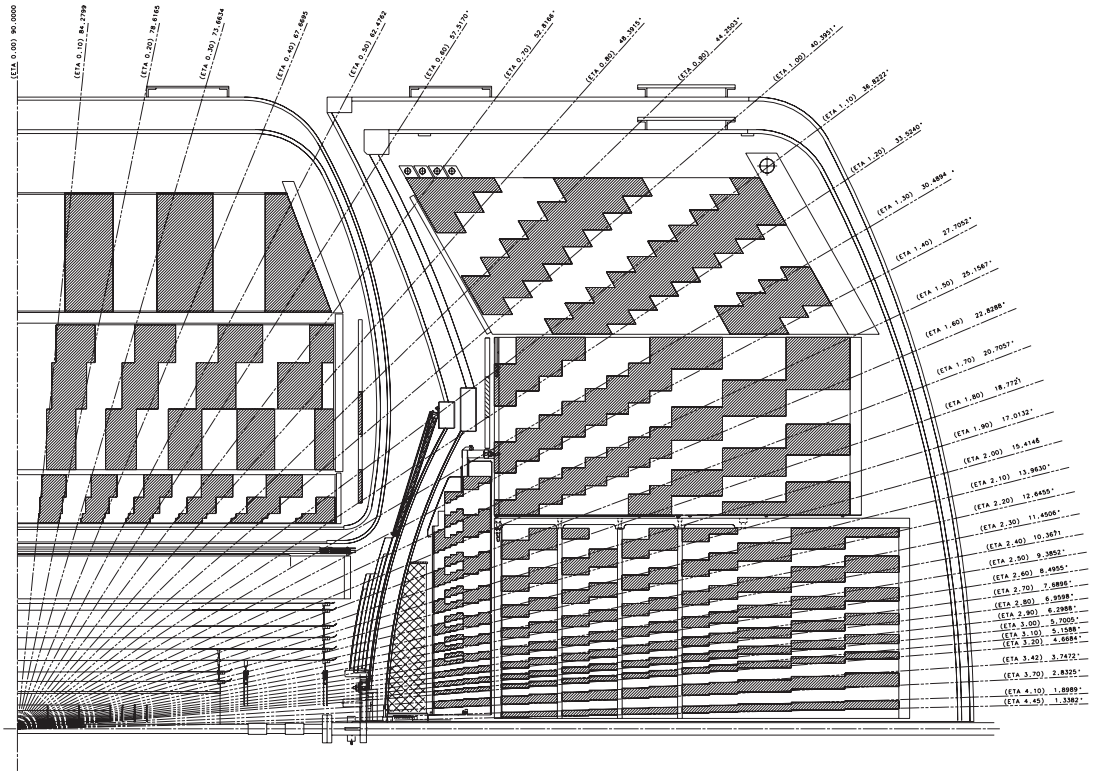

Figure 3.7.: Cross sectional view in rz-plane of a calorimeter quadrant. Each of the towers has a size of approximately $\Delta\eta \times \Delta\phi = 0.1 \times 0.1$.

The identification of electromagnetic and hadronic objects utilises the fact, that electromagnetic and hadronic showers develop differently, due to the difference in the underlying interacion. The electromagnetic interaction mechanism features three main processes: Bremsstrahlung in the presence of an electromagnetic field ($e \to e + \gamma$), photon pair production ($\gamma \to e^+e^-$), and, less important for high energies, Compton scattering ($e\gamma \to e'\gamma'$). The electron interaction is characterised by the radiation length X_0, being $X_0 = 0.32\,\text{cm}$ for ^{238}U. The more an electromagnetic shower develops with rising multiplicity of secondary electrons and photons produced by the two processes above, the stronger is the actual signal measured via ionisation processes. Since at high energy, the emission angle of secondaries is small and the shower develops primarily in the direction of the incident particle. A hadronic shower is dominated[4] by inelastic collisions with nuclei and the multiparticle production of slow pions or kaons, characterised by an interaction length $\lambda_I = 10.5\,\text{cm}$. The mean transverse momentum for secondaries produced in hadronic interactions is 350 MeV. Therefore, on average, a hadronic shower will develop on a longer distance in radial direction and will be more spread out laterally than an electromagnetic one, which is the key to the distinction of the two processes employing the event shape versus cluster fraction and the strength of the electromagnetic response over the strength of the hadronic response e/h. Due to the low cross section for weak processes, there is no detector component for the detection of particles which only interact weakly like neutrinos.

The main constituent part of the calorimeter is the Uranium Liquid Argon Calorimeter, but

[4] approx. 1/3 of the secondary particles produced in a hadronic interaction are π^0's, which mainly give photons via $\pi^0 \to \gamma\gamma$ with a subsequent conversion of photons to electrons and thus an electromagnetic signal when decaying.

there also are the Central and Forward Preshower Detectors (FPS, CPS) as well as Intercryostat Detectors (ICD). Refer to Fig. 3.7 for a visualisation. Most important components will be dealt with after a brief discussion of the uncertainty on the energy measurement.

Uranium Liquid Argon Calorimeter

The part of the Run I DØ detector which was almost kept in its entirety is the Uranium Liquid Argon Calorimeter [49]. As can be seen from Fig. 3.7 and 3.8, it is divided into 3 parts, kept at a temperature of 80° K in separate cryostats: the Central Calorimeter (CC), and the two End Caps (EC). The central calorimeter covers an η region of $|\eta_{\text{det}}| < 1.3$. Together with the end caps, a rapidity region of $|\eta_{\text{det}}| < 4.2$ is covered. The featured calorimeter design with separated CC and EC sections has its drawback in form of a region of limited response in the η-range of approx. $0.8 \lesssim \eta_{\text{det}} \lesssim 1.1$.

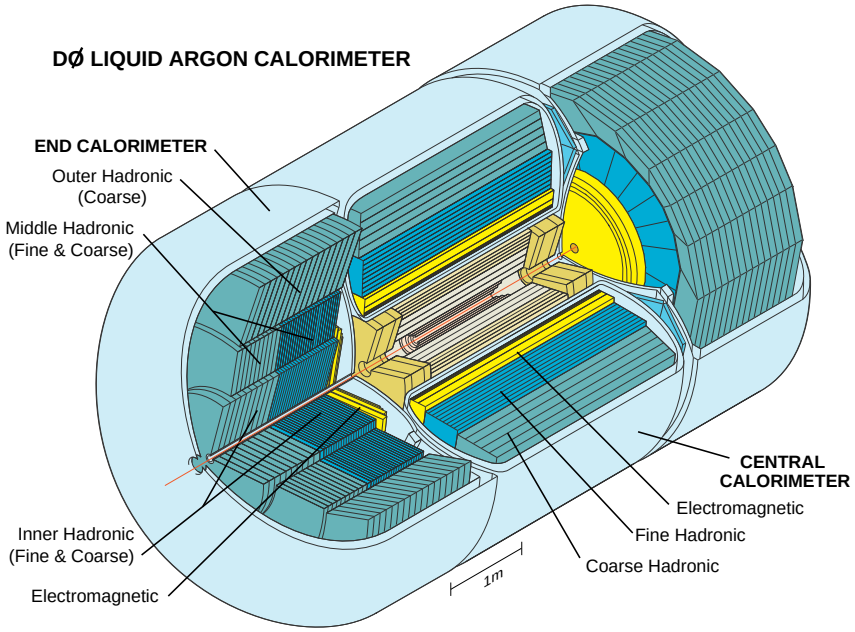

Figure 3.8.: Three dimensional cut away view of the DØ Calorimeter.

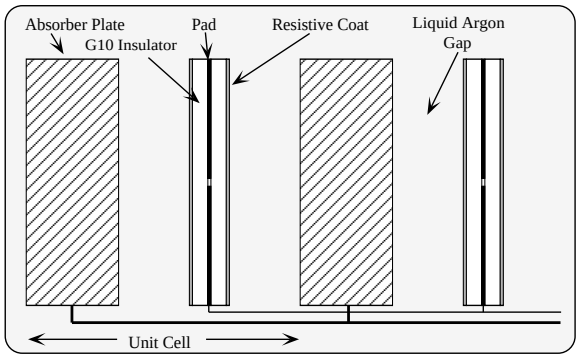

Figure 3.9.: Schematic view of a liquid argon calorimeter cell.

Following from the differences in shower development for electromagnetic and hadronic objects as discussed above, a radial division of the calorimeter in an electromagnetic part featuring a length of $\sim 20\,X_0$ and a hadronic part of $\sim 7.2\,\lambda_I$ is favourable. The segmentation in η is $\Delta\eta = 0.1$. In ϕ, there is a lateral granularity of $\Delta\phi = 2\pi/64 \simeq 0.1$. Thus, there is an overall segmentation $\Delta\eta \times \Delta\phi = 0.1 \times 0.1$, which is true for all floors except for EM3, where a two times finer granularity is needed, in order to locate an electromagnetic object most precisely at the maximum of its shower development. The choice of $\Delta\eta$ and $\Delta\phi$ is motivated by an average jet cone size of $\Delta R := \sqrt{\Delta\eta^2 + \Delta\phi^2} \simeq 0.5$. The segmentation of the calorimeter in the rz plane is shown in Fig. 3.7.

The DØ LAr calorimeter is a so-called sampling calorimeter with a sandwich structure in radial direction, which features high-density shower inducing material with a depth of $\mathcal{O}(5\,\mathrm{mm})$, sliced by gaps where the actual signal is registered. In fact, it is not a continuous registration, rather the signal is sampled from gap to gap, giving the structure its name. A calorimeter cell is symbolically depicted in Fig. 3.9. The shower inducer is almost pure depleted ^{238}U for the EM calorimeter, in the hadronic calorimeter a Uranium-Niobium alloy was used. The registration units are drift chambers with liquid argon as active medium. An electric field of approx. 1.6 kV is applied, and the charge is collected with laminated copper plates. The average signal charge collection time across the 2.3 mm LAr gap is of the order of $\mathcal{O}(500\,\mathrm{ns})$.

Energy Resolution

The measurement of the energy in the calorimeter utilises the charge produced by ionisation processes induced by a particle or its secondaries in a shower, independent of the electromagnetic or hadronic nature of it. In other words, the amount of charge produced is a function of the energy of the incident particle. If there is no difference in the response of the calorimeter to electromagnetically or hadronically interacting particles, the calorimeter is called *compensating*. This favourable scenario applies with minor drawbacks to the DØ calorimeter: $1 < e/\pi < 1.05$ above 30 GeV.

The relative error on the energy is parametrised as

$$\frac{\Delta E}{E} = C \oplus \frac{1}{\sqrt{E}} \cdot S \oplus \frac{1}{E} \cdot N\,. \tag{3.3}$$

Additionally to the so-called *sampling fluctuation* error S due to fluctuations in the amount of ionisation charge produced, there is the *constant* term C, which accounts for the offset in the calorimeter response due to inhomogeneities, and the *noise* term N, which to the largest part stems from electronic readout devices. The error constants $C,\ S,\ N$ are summarised in Chap. 5.

3.2.3. The Muon System

The Muon System [50, 51, 52, 53] is the outermost of the main detector components. It is responsible for the detection of muons, which penetrate the tracker and calorimeter with little momentum loss, approximately 2 GeV on average.

As already mentioned in the introduction to the Calorimeter section, MIP's can traverse the whole calorimeter without losing much of their initial momenta. To be more specific, they must

be muons, as they have a sufficiently long path length (due to a half life of 1.6 μs) unlike the τ-leptons, and have a high mass, unlike electrons with $m_e \simeq 0.5\,\text{MeV}$. The much higher mass of $\sim$106 MeV is responsible for the fact, that the acceleration in the electromagnetic field of the atoms of the calorimeter material is smaller than for electrons, and so are the radiative energy losses via bremsstrahlung processes:

$$\frac{\mathrm{d}E}{\mathrm{d}x}\Big|_{\text{brems}} \propto \frac{1}{m^2}\,.$$

The momentum of the muons is measured by analysing their bending radius in a toroidal magnetic field of 1.8 T.

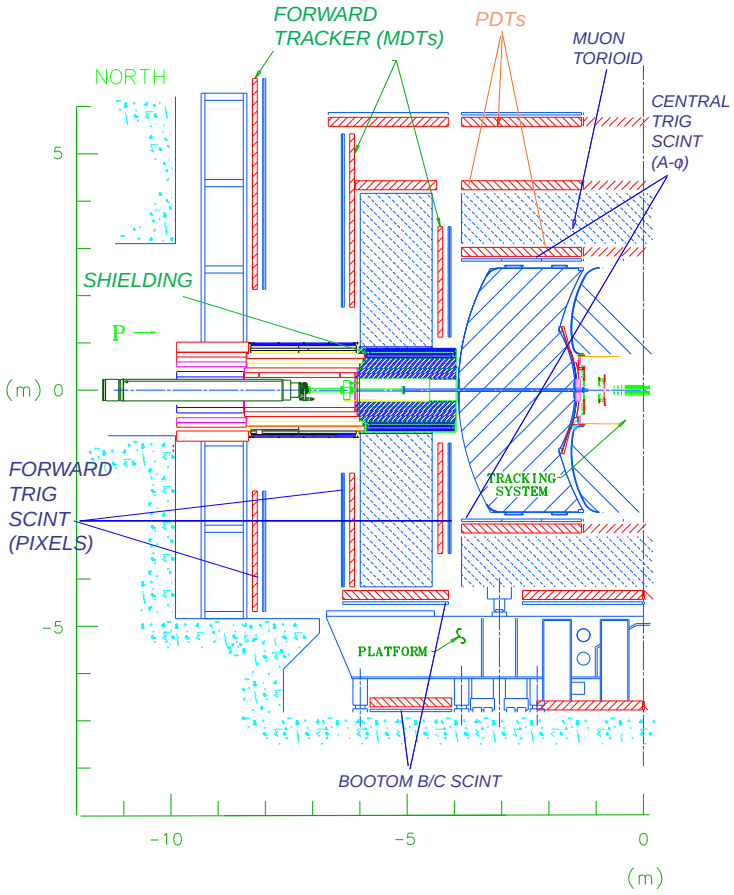

Figure 3.10.: An rz-plane half view of the Muon System. Components of both the Forward and the Wide Angle System are shown.

The Muon System is divided into the central [51] and forward [52] parts, as depicted in Fig. 3.10. They will be treated in the following.

The Central Muon System (WAMUS – Wide Angle MUon Spectrometer) provides a coverage for an η-region of approx. $|\eta_{\text{det}}| < 1$. It consists of three layers, denoted as A, B, C in downstream order. The layer A is inside of the toroidal magnetic field, whereas B and C are outside. All three central layers are made of Proportional Drift Tubes, which analyse the potential changes induced by the collection of the ionisation charge created by muons in the active medium. In contrary to the LAr calorimeter, the active medium is here a gas mixture Ar:CH_4:CF_4 (80%:10%:10%) operated at room temperature. The new mixture choice with respect to Run I is motivated

by a faster drift time. This decreases the maximum signal collection time to ∼450 ns, which results in a reduced occupancy, signal separation and improved triggering, essential for coping with the increased luminosity: on average 2 interactions per bunch crossing and a smaller bunch crossing time of 396 ns instead of 3.5 μs. The negative trade-off is a decreased spatial resolution due to diffusion, which is ∼375 μm, compared to 300 μm for the slower Run I gas. The readout electronics has been completely replaced for deadtimeless operation.

In front of the A-layer, just outside of the calorimeter, a layer of scintillation counters is installed. Its main purpose is to provide a fast trigger signal for the muons, as the mean response time of 1.6 μs is two orders of magnitude lower than for the PDT. Its time information is also used for the rejection of muons originating from cosmic interactions in the atmosphere and secondary interactions in the forward regions of the detector.

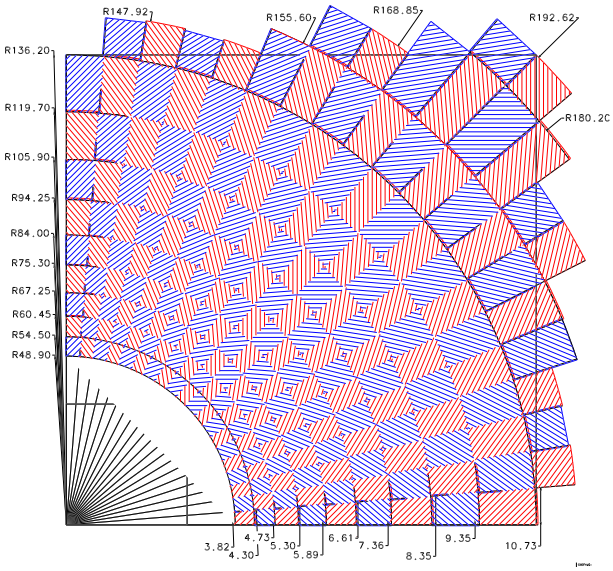

Figure 3.11.: An $r\phi$ view of the segmentation of the Forward Muon System scintillator counters.

The Forward Muon System (FAMUS – Forward Angle MUon Spectrometer) covers the region of approx. $1 < |\eta_{\text{det}}| < 2$. Similar to the central muon system, it is comprised of 3 layers of proportional drift tubes, called MDT's (Mini Drift Tubes). Their small dimensions of 1 cm × 1 cm allow an excellent pattern recognition and low occupancy, which was the reason for the complete replacement of the Forward Muon System for Run II. The active medium is the fast gas CF_4:CH_4 (90%:10%), featuring a maximum drift time of 60 ns. In contrary to the Central Muon System, each of the 3 layers has a scintillator layer attached [53], with a segmentation in ϕ of $\Delta\phi = 4.5$ and η segmentation of $\Delta\eta = 0.07, 0.12$ for the 3 inner and 9 outer rows, respectively, shown in Fig. 3.11.

An important part of the muon system is the shielding installed around the beam pipe in the forward regions. Its main purpose is to reduce backgrounds due to scattered p and $\bar{p}$ remnants interacting with the detector components and beam halo interactions. The shielding consists of 39 cm of iron, acting as a hadron and electromagnetic absorber, 15 cm of polyethylene, perfectly suited to moderate and absorb neutrons with its high hydrogen content, and, finally, 15 cm of lead to absorb gamma radiation.

3.2.4. The Trigger Framework

A big challenge for any hadron collider experiment is the selection of events interesting from a physics point of view, as far too many events occur to be written to tape: the Tevatron in its current configuration features a bunch crossing time of 396 ns, which corresponds to a rate of approx. 2.5 MHz, whereas the rate-to-tape is 50 Hz only. To fulfil this task and reduce the number of events by more than 4 orders of magnitude, online triggers are needed, which provide a fast decision if the event should be stored for future analysis or not. The DØ trigger consists of 3 stages denoted as Level 1 to 3, reducing the event rate in steps of 5-10 kHz (L1 → L2) and 1 kHz (L2 → L3). Figure 3.12 represents schematically the information flow from trigger to trigger. On average, each event consists of 250 kb of information. In the following, the 3 levels will be discussed in consecutive order.

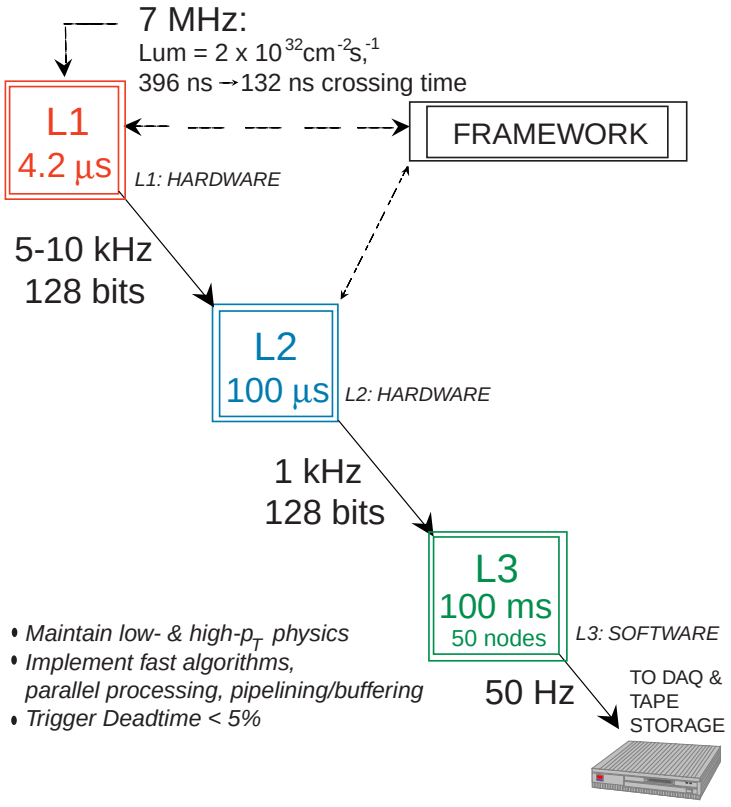

Figure 3.12.: A scheme of the DØ trigger framework.

Level 1

The Level 1 trigger is a hardware trigger, i.e. it employs the information coming directly from the detector electronics and performs very basic algorithms like forming energy towers in the calorimeter with $\Delta\eta \times \Delta\phi = 0.2 \times 0.2$ and comparing their energy content with thresholds as well as analysing hit patterns in the central fibre tracker, the preshower and the muon system. For electromagnetic objects, a range of $|\eta_{\text{det}}| < 2.5$ is considered, whereas for muons $|\eta_{\text{det}}| < 2.0$ is taken into account. The pass rate to Level 2 is in the range between 5 and 10 kHz.

Level 2

Level 2 is a a combination of a hardware readout and simple software trigger comprised of 2 parts – the preprocessor and the global processor stage. The former reads out the complete event information from the detector subsystems and forms physics objects. These are passed over to the global processor stage, which combines the physics objects and meets a pass/reject decision. The rate to Level 3 is fixed to 1 kHz by its handling speed limitation, whereas the pass rate of Level 3 *fluctuates* around the same value. To reduce information losses due to this inefficiency, the output of Level 3 is fed into a buffer system first.

Level 3

Different from the previous triggers, the Level 3 is a pure software trigger, which is run on a collection of 100 computer nodes. First, from the Level 2 information, the event is reconstructed and a decision is made on the basis of real physical quantities like the number of vertices or the E_T of the event. Events which pass the selection criteria are written to tape at a rate of 50 Hz and are available for offline analysis.

4. The Analysed Dataset

In this Chapter, the analysed dataset and the corresponding Monte Carlo simulation will be discussed in consecutive order. A special focus is placed on the selection criteria, which have been optimised for selecting a sample of events with dileptonic final states featuring a signal-to-background ratio as high as possible. A good selection guarantees that the full potential of the dileptonic $t\bar{t}$ decay channels with their low systematics be exploited. For all three channels, control plots for data and Monte Carlo with all cuts applied are shown.

4.1. The Dataset

The data analysed in this thesis corresponds to an approximate integrated luminosity of $\int \mathrm{d}t\, \mathcal{L} = 370\,\mathrm{pb}^{-1}$. It was reconstructed with version `p14` of DØ software. Additionally, in the $e\mu$ channel a data superset of approx. $835\,\mathrm{pb}^{-1}$ is considered, reconstructed with `p17`. Due to the much improved reconstruction software there is a significant difference between the two datasets. Therefore, they will be treated separately in the following.

4.1.1. The $370\,\mathrm{pb}^{-1}$ Dataset

The $370\,\mathrm{pb}^{-1}$ dataset was collected from August 2002 to August 2004. A breakdown in trigger list versions and the corresponding collected luminosity can be found in Tab. 4.1 [54, 55, 36, 37]. All samples have been reconstructed with `D0Reco` versions `p14.03.01` through `p14.06.00`. For production of the ROOT [56] ntuples used in the analysis the `Ipanema` [57] version of the `top_analyze` package [58] was employed. The skims used to select the data are summarised in Tab. 4.2. A more detailed skim description can be found in [59]. Duplicate events are removed

	$\int \mathrm{d}t\, \mathcal{L}[\mathrm{pb}^{-1}]$		
Trigger List	$e\mu$	ee	$\mu\mu$
`v8`	18.25	20.08	22.02
`v9`	21.26	30.75	21.22
`v10`	15.26	15.48	7.99
`v11`	57.26	57.38	57.26
`v12`	209.82	217.41	209.83
`v13`	45.82	42.97	44.31
total	367.7	384.1	362.6

Table 4.1.: Breakdown of integrated luminosities by trigger list version.

Skim	Requirement	Usage
EMU	≥ 1 medium electron AND ≥ 1 medium muon	Signal Sample for $e\mu$ analysis
EMU_EXTRALOOSE	≥ 1 loose electron AND ≥ 1 medium muon	Sample for $e\mu$ fake rate estimation
DIEM	≥ 2 medium electrons	Signal Sample for ee analysis; fake $\not\!\!E_T$ background estimation
DIEM_EXTRALOOSE	≥ 2 loose electrons	Sample for e fake rate estimation
DIMU	≥ 2 loose muons OR 2 medium muons,	Signal Sample for $\mu\mu$ analysis; fake μ background estimation

Table 4.2.: List of data subskims from the DØ Top Group used for the $370\,\mathrm{pb}^{-1}$ dataset. The definition of loose and medium electrons, and medium muon are detailed in Chap. III of [54].

from the analysis. Bad events are removed in units of bad luminosity blocks and bad runs. For the luminosity calculation and the data quality requirements named above the `top_dq` package `v00-05-01` was employed [60]. The definition and a detailed discussion of physics objects used in the `p14` dataset can be found in [54, 55]. The triggers in this analysis select events with dilepton candidate signatures at Level 1, as well as at Level 2 for the muons and at Level 3 for the electrons. The triggers were applied with `t04-00-03` version of the `top_trigger` package [61]. They are summarised in Tab. 4.3. The jets were calibrated to parton level using `JetCorr v5.3` [62]. The energy of all jets in Monte Carlo was scaled up by a factor of 1.034, to correct for differences between data and Monte Carlo, as found in [63].

The cuts applied to select the analysed events are described and control distributions are presented in Sec. 4.3.1.

4.1.2. The $835\,\mathrm{pb}^{-1}$ Dataset

In the $e\mu$ channel a dataset of $835\,\mathrm{pb}^{-1}$ collected from August 2002 until November 2005 is analysed. The $370\,\mathrm{pb}^{-1}$ data sample is a subset of the $835\,\mathrm{pb}^{-1}$ data. The latter was reconstructed with the `p17` version of the DØ software. This version features enhanced track reconstruction and track matching algorithms for the tracker and the muon system[64]: an adaptive vertex algorithm, new track refitting, muon time-to-distance relation; improved jet reconstruction algorithms, a more detailed model of the detector in GEANT [65] and more. The biggest advantage of the `p17` dataset is the calibration of both the electromagnetic [66, 67] and the hadronic calorimeter, which for example has improved the $\not\!\!E_T$ resolution by several GeV [68]. The data quality requirements were slightly changed [69].

Several events selected in the $370\,\mathrm{pb}^{-1}$ dataset reconstructed with the `p14` version of DØ software are not selected in `p17` and vice versa. This is mainly caused by improved reconstruction algorithms and the resulting changes in variables of physics objects rather than by data quality requirements [69].

The data sample is selected from the Common Samples Group EMU skim. After reconstruction

Channel	Trigger List	Trigger
$e\mu$	v8.2, v8.3	MU_W_EM10
	v8.4 - v11	MU_A_EM10
	v12	MATX_EM6_L12
	v13 - v13.3	MUEM2_LEL12
	v13.3 - v14	MUEM2_LEL12_TRK5
	v14	MUEM2_SH12_TRK5
ee	< v12	2EM_HI
	v12	Ex_2L20 OR Ex_2L15_SH15, x=1,2,3
	v13.1	E2x_2L20 OR E2x_2SH8 OR E2x_2L15_SH15, x=0,1,2
	v13.2	E2x_2L20 OR E2x_2SH10 OR E2x_2L15_SH15, x=0,1,2
$\mu\mu$	< v11	2MU_A_L2M0
	v11	2MU_A_L2M0_L3TRK10 OR 2MU_A_L2M0_L3L15
	v12	2MU_A_L2M0_L3TRK5 OR 2MU_A_L2M0_L3L6
	v13	DMU1_TK5, DMU1_LM6

Table 4.3.: Triggers used for the 370 pb^{-1} dataset. For the $e\mu$ channel the triggers for the 835 pb^{-1} dataset (> v14) are appended.

with the p17 version of D0Reco the data has been analysed with Tmbanalyze p18, and then processed with CAFe version p18-br-90 [70]. CAF trees were produced with version p18.05.00. The triggers used for the full dataset are listed in Tab. 4.3. Jets have been calibrated to particle level using JetCorr p18-br-05 of DØ software release p18.07.00 [62].

4.2. The Monte Carlo Samples

In this section information will be provided on the Monte Carlo samples used to estimate signal and background selection efficiencies and to calibrate the Neutrino Weighting Method for the top quark mass measurement. Again, there is a difference between the 370 pb^{-1} and the 835 pb^{-1}dataset, and the Monte Carlo sets will be discussed separately. A general discussion of contributing physics and instrumental background processes from the physics point of view is presented in Chap. 2, Sec. 2.3. Here, only technical details are given.

4.2.1. Monte Carlo for the 370 pb^{-1} Dataset

In the 370 pb^{-1} dataset the Monte Carlo samples for signal and background are generated with ALPGEN [71]. The fragmentation and decay is carried out with PYTHIA [72]. The τ leptons are decayed using TAUOLA [73] before further D0Sim processing of events. The detector response has been simulated with GEANT [65]. The specific samples are described in Tab. 4.4.

In the $e\mu$ channel, the single electron and the single muon trigger [74, 75] is simulated using a p_T-dependent efficiency, in the $\mu\mu$ channel the trigger efficiency for the muons is modelled in pseudorapidity bins. In the ee channel no such corrections are applied, since the electron trigger is nearly 100% efficient for $p_T^e > 15\,\mathrm{GeV}$.

Process	PDF	Underlying event	Parton Cuts	σ [pb]
$t\bar{t}$	CTEQ5L	tune A	-	7.0
$Z/\gamma^* jj \to \tau\tau jj;\ \tau \to e, \mu$	CTEQ5L	tune A	CAPS	2.90 ± 0.05
$Z/\gamma^* jj \to eejj$	CTEQ5L	tune A	CAPS	23.4 ± 0.4
$Z/\gamma^* jj \to \mu\mu jj$	CTEQ5L	tune A	CAPS	23.4 ± 0.4
$WWjj \to ll\nu\nu jj$	CTEQ4L	Pythia	-	0.29 ± 0.10

Table 4.4.: Monte Carlo Samples used in this analysis, together with the Parton Distribution Functions (PDF's) [23], underlying event model, parton level cuts and cross section. The samples for the $Z \to ll$ are for the central mass bin ($60 < m_{ll} < 120\,\text{GeV}$) and their cross sections are derived from the DØ measured cross section. $WW \to ll$ uses the theoretically predicted cross section. The parton level cuts referred as CAPS are explained in the text.

All background samples up to the diboson sample are generated with Monte Carlo settings and parton level cuts prescribed by the Common Samples Alpgen+Pythia Study (CAPS) group [76]. The CAPS samples are produced with version `v1.3.3` of ALPGEN. The parton level cut on leptons is $|\eta| < 10$, whereas for jets the parameters have to be restricted to $p_T > 6\,\text{GeV}$, $|\eta| < 3.5$ because of QCD infrared divergences. The minimum distance between two jets is $\Delta R_{\eta\times\phi}(j_1, j_2) > 0.4$. There is no cut on the minimum angular distance between a jet and a lepton. The momentum transfer scale[1] is $Q^2 = m_Z^2 + \sum p_T^2$ for CAPS samples and m_{top}^2 for signal samples.

The signal Monte Carlo is available with top quark masses ranging from 140 to 210 GeV in 5 GeV steps, and 4 additional samples with m_{top}=120, 130, 220, 230 GeV. Dileptonic signal Monte Carlo contains leptonic final states only, with inclusive τ decays.

All $Z/\gamma^* jj \to ll\nu\nu jj$ samples contain the full Drell-Yan interference structure. They were generated in 3 bins in the dilepton mass m_{ll}, but only the mass bin $60 < m_{ll} < 120\,\text{GeV}$ is used in this analysis. The samples with a lower dilepton mass $15 < m_{ll} < 60\,\text{GeV}$ are not considered since their selection efficiency is 2 orders of magnitude lower, whereas the cross section is similar. Samples with a high dilepton mass are not considered because their cross section is two orders of magnitude lower, with a similar selection efficiency. In one part of the $Z/\gamma^* jj \to \tau\tau jj$ sample, τ leptons are forced to decay to electrons and muons, in the other part features inclusive τ decays. To achieve proper normalisation, a cut on Monte Carlo truth level is to be applied to discriminate non-leptonic τ decays, as pointed out in [77].

The diboson sample includes $WWjj \to lljj$ processes, with $l = e, \mu, \tau$. The τ leptons decay inclusively. The diboson sample is the only background where a theoretical cross section is used for normalisation. The cross section for diboson production has been updated after the generation of the Monte Carlo sample from leading order to next-to-leading order, which is higher by a factor of 35% [78]. The cross section shown in Tab. 4.4 already contains this update.

[1] i.e. the scale at which the PDF's are evaluated.

4.2.2. Monte Carlo for the 835 pb^{-1} Dataset

Signal Monte Carlo event samples are generated with PYTHIA [72] in 5 GeV increments in the top quark mass range from 155 to 200 GeV. Parton Distribution Functions (PDF's) as provided by the CTEQ collaboration in version CTEQ6.1M are used [79]. All signal and background Monte Carlo samples are selected with the same cuts as in data, with the exception of a trigger requirement. Single electron [66, 67, 80] and muon efficiencies [64] were corrected p_T-dependent to account for differences to the measured efficiencies in data. Background Monte Carlo samples are also generated with PYTHIA. Backgrounds from $Z \to ll$ and $WW+2jet$ decays are simulated in these samples. For the $Z \to \tau\tau$ sample, to increase statistics of $\tau \to e, \mu$ with $p_T(e) > 10$ GeV and $p_T(\mu) > 10$ GeV, a production cut was applied at the generator level before reconstruction. Finally, jets in Monte Carlo have been modified using the smearing and removal prescription of the Jet Smearing, Shifting and Removal (JSSR) study [81]. This procedure is very important to obtain a good estimate of $\not\!\!E_T$ in Monte Carlo, since the Neutrino Weighting Algorithm relies heavily on it. GEANT was used to simulate the detector response [65].

4.3. Selection of the Data Sample

The analysis sample selection for the dilepton channel bases on the signature of dileptonic $t\bar{t}$ decays. As already discussed in Chap. 2, this signature consists of two leptons of opposite charge with a high p_T, two b-quark jets also with a high p_T and two neutrinos, which give rise to a high $\not\!\!E_T$ value. This is a unique signature, naturally rejecting most of the backgrounds, as argued in Chap. 2, Sec. 2.3.

It must be kept in mind that with the kinematic reconstruction in the Neutrino Weighting Algorithm two quadratic equations have to be solved. If these produce no real solutions for all possible constellations of smeared variables, the event is considered inconsistent with the $t\bar{t}$ decay hypothesis and removed from further analysis. This is the case for 0.2% of signal and 4.0% of background events [82]. In fact, this is an additional posterior cut.

4.3.1. Selection Criteria for the 370 pb^{-1} Dataset

For the 370 pb^{-1} dataset, the data quality requirements are the same in all three channels. Their detailed description is given in [54, 55]. In the following, the physics objects selection criteria which are common for all three channels are listed. A definition of the multivariate variables used at the DØ experiment like the H-matrix characterising the electron shower shape is given in [83].

- Leptons:
  - $p_T^l > 15$ GeV since we expect high-p_T objects,
  - The selected lepton pair must have opposite charge sign to reject QCD and bosonic backgrounds,
  - No common track for any electron and muon, where at least one of them is selected as the leading or next-to-leading lepton to suppress muon Bremsstrahlung processes,

  - Electrons:
    * high fraction of the energy must be deposited in the electromagnetic part of the calorimeter for discrimination against hadrons: $f_{\mathrm{EM}} > 0.9$,
    * the cluster in the electromagnetic calorimeter is to be isolated: $f_{\mathrm{iso}} < 0.15$,
    * the shower should have an electromagnetic-like shape: $\chi^2_{\mathrm{hmx7}} < 50$,
    * the electron likelihood value must be high to reject π^0's which mimic electrons: $\mathcal{L}^7_{\mathrm{EM}} > 0.85$,
    * there must be a matched track corresponding to the electromagnetic cluster in the calorimeter to reject photons: $p_{\chi^2_{\mathrm{trk}}} > -1$;
  - Muons:
    * the pseudorapidity region is restricted to $|\eta| < 2$ due to the limited acceptance of the muon system,
    * the muon must have medium quality (see [36, 54, 55] for the definition of this criterion) and be reconstructed using all 3 layers of the muon system,
    * timing cuts against cosmics are applied,
    * the muon must be matched with a central track,
    * the matched track must fulfil quality requirements: the Distance of Closest Approach (DCA) to the central vertex must be small: $|\mathrm{DCA}|/\sigma_{\mathrm{DCA}} < 3$, $\chi^2_{\mathrm{trk}} < 4$,
    * the isolation must be tight both in the calorimeter and the tracker: Rat11 < 0.12, Rattrk11 < 0.12;

- Jets:
  - 2 or more jets are required,
  - $p_T^j > 20\,\mathrm{GeV}$,
  - $|\eta| < 2.5$ due to the limited acceptance of the calorimeter and the rising multiplicity due to QCD events for high η,
  - The fraction of energy deposited in the electromagnetic part of the calorimeter be not too small to reject neutral hadrons as well as mis-reconstructed objects, and not too high to reject electrons and photons: $0.05 < f_{\mathrm{EM}} < 0.95$;

No b-tagging is applied. Rather, the leading and next-to-leading jets are selected for further analysis.

Besides the "natural" selection criteria listed above, a series of so-called topological cuts based on the topology of the event in the detector is introduced. Since the backgrounds and their relative contributions are different in the 3 channels, they are listed separately in the following.

The $e\mu$ Channel

The big advantage of the $e\mu$ channel is that the $Z \to ee, \mu\mu$ background is not present here and the cuts do not have to be chosen as aggressively as in the other two channels. In particular, the cut on $\not\!\!E_T$ can be omitted, resulting in a high yield and a high overall figure of merit, canonically defined as f.o.m. $:= \sqrt{\mathrm{signal}/(\mathrm{signal} + \mathrm{background})}$.

The topological cuts applied in the $e\mu$ channel are:

Process	Event yield	Stat. Err	Syst. Err
$Z/\gamma^* jj \to \tau\tau jj$	1.15	0.18	$^{+0.28}_{-0.35}$
$WWjj \to e\mu\nu\nu jj$	0.81	0.08	$^{+0.44}_{-0.47}$
QCD	0.31	$^{+0.36}_{-0.25}$	$^{+0.06}_{-0.09}$
total bgr	2.27	$^{+0.41}_{-0.32}$	$^{+0.53}_{-0.59}$
expected sig	11.02	0.15	$^{+1.22}_{-1.42}$
selected events	17	–	–

Table 4.5.: Final signal and background event yield [84, 77] in the $e\mu$ channel for $367.7\,\mathrm{pb}^{-1}$of DØ Run II data reconstructed in `p14`. A top quark mass $m_{\mathrm{top}} = 175\,\mathrm{GeV}$ and $\sigma_{t\bar{t}} = 7\,\mathrm{pb}$ have been assumed. Both the statistical and systematic error are given. All events produce solutions with the Neutrino Weighting Algorithm. The event yield stated for $WWjj \to e\mu\nu\nu jj$ includes the $WZjj$ process as well.

- One and only one electron fulfilling the electron selection criteria listed above is required. This cut was introduced to reject $Z \to ee$ background with underlying events and QCD processes.
- If several muons are present, the $e\mu$ pair to give the highest p_T sum is chosen, in order to reject muons from the decay of the b-quarks with a high p_T with respect to the momentum vector of the b-jet, which are faking their isolation.
- The H_T-parameter of the leading lepton l_1 is required to be sufficiently high: $H_T^{l_1} > 122\,\mathrm{GeV}$. This requirement is introduced to discriminate against the $Z \to \tau\tau$ background. Here, the H_T of the leading lepton is defined as: $H_T^{l_1} := p_T^{l_1} + \sum p_T^{j_i}$, where the sum runs over all jets to fulfil the requirements introduced above.

The main difference to the cross section analysis for the $e\mu$ channel is that for the top quark mass measurement a cut on the electron likelihood $\mathcal{L}^7_{\mathrm{EM}} > 0.85$ is applied. This is done since for a property measurement a pure sample is needed, whereas for a cross-section measurement a likelihood fit approach is adequate.

The QCD background sample is selected from the EMU_EXTRALOOSE data skim of the by requiring that the electron be of "extra-loose" quality. In particular, the cuts on the fraction of energy deposited in the electromagnetic calorimeter f_{EM}, on the isolation f_{iso}, on the shower shape χ^2_{hmx7}, and on the electron likelihood $\mathcal{L}^7_{\mathrm{EM}}$ are dropped. The QCD background selection is made orthogonal to the signal selection by demanding that no spatial track be matched to the cluster in the calorimeter. The requirements stated above select a sample of events with a high probability that the electromagnetic objects are faked by QCD processes involving π^0 production, and thus are a good estimate for the QCD class of events entering the signal selection. Applying the QCD background selection yields 107 events.

The final event yields for the $e\mu$ channel from the EMU skim of the $370\,\mathrm{pb}^{-1}$ dataset reconstructed with `p14` are given in Tab. 4.5 [84]. There, both the statistical and the systematic error are stated. For the signal part, $\sigma_{t\bar{t}} = 7\,\mathrm{pb}$ and a top quark mass $m_{\mathrm{top}} = 175\,\mathrm{GeV}$ have been assumed. Since the yields for the individual processes have decreased with respect to the numbers in the cross section note [55] due to the applied electron likelihood cut, the systematic error has been scaled by the relative ratio of the yields for a given process. It is important to note that the numbers for the WW process have been updated, as in the cross section analysis

the correction factor of 1.35 introduced in Sec. 4.2 was applied twice [77]. The control distributions are shown in Fig. 4.1. To within the statistics available no discrepancies are observed. All selected events can be reconstructed with the Neutrino Weighting Algorithm. A list of selected events with basic quantities of physics objects relevant for this analysis is presented in App. A.

It has been evaluated how well the QCD background selection describes non-signal processes. For this purpose, the QCD background selection efficiencies for four Monte Carlo signal samples have been determined:

Process	σ [pb]	$\varepsilon_{\mathrm{QCD}}$
$t\bar{t} \to ll\nu\nu jj$	0.67	0.00817
$t\bar{t} \to ll\nu\nu jj{+}j$	0.39	0.00046
$t\bar{t} \to l\nu jjjj$	2.68	0.00448
$t\bar{t} \to l\nu jjjj{+}j$	1.54	0.00036

Using the generated cross section numbers, the expected number of events for a luminosity of $367.7\,\mathrm{pb}^{-1}$ is calculated for each process. Multiplying these numbers by the selection efficiency estimates the signal event yield for the selection of the QCD multijet background to 4.78 events. Dividing this number by 107 – the number of selected QCD background events from the EMU_EXTRALOOSE skim – gives an estimate on the signal efficiency for the QCD background selection: $\hat{\varepsilon} = 4.5\%$. Thus, the estimated fraction of $t\bar{t}$ events in the QCD sample is 4.5%. This number verifies the validity of the chosen approach. In this study, no signal Monte Carlo sample representing the all-jets channel has been considered, since the selection efficiency of the QCD multijet background is expected to be very low due to the absence of high-p_T leptons in the final state.

The ee Channel

The most problematic background process for the ee channel is $Z/\gamma^* jj \to eejj$. To remove it and the other backgrounds the following topological cuts are applied:

- The so-called "Z-window" is cut: $80 < m_{l_1 l_2} < 100\,\mathrm{GeV}$.
- The $\not\!\!E_T$ value must be high: $\not\!\!E_T > 35\,\mathrm{GeV}$ for $m_{l_1 l_2} < 80\,\mathrm{GeV}$, $\not\!\!E_T > 40\,\mathrm{GeV}$ for $m_{l_1 l_2} > 120\,\mathrm{GeV}$. This rejects neutral current processes. The $\not\!\!E_T$ cut value above the Z window is chosen 5 GeV higher than below to reject the $Z \to \tau\tau$ background, which occupies this region.
- The sphericity must fulfil $S > 0.15$. The sphericity is defined as $S := 3(\varepsilon_1 + \varepsilon_2)/2$, where $\varepsilon_{1,2}$ are the 2 smallest eigenvalues of the normalised momentum tensor calculated using all leptons and jets satisfying the criteria above. High S-values are typical for $t\bar{t}$ production events. The contrary is true for the backgrounds. The normalised momentum tensor is defined as $T_{ij} := p_i p_j / \sum_k p_k^2$, where i, j, k indices refer to all leptons and jets satisfying the selection criteria listed at the beginning of this section.

The QCD background sample has been selected from the DIEM_EXTRALOOSE skim in a similar fashion as for the $e\mu$ channel. For both selected leading electrons the same cuts are

Process	Event Yield	Stat. Err	Syst. Err
$Z/\gamma^* jj \to eejj$	0.45	0.15	0.00
$Z/\gamma^* jj \to \tau\tau jj$	0.31	0.06	$^{+0.08}_{-0.13}$
$WWjj \to ee\nu\nu jj$	0.22	0.07	$^{+0.08}_{-0.13}$
QCD	0.09	0.03	$^{+0.03}_{-0.03}$
total bgr	1.07	0.18	$^{+0.11}_{-0.18}$
expected sig	3.51	0.08	$^{+0.34}_{-0.39}$
selected events	5	–	–

Table 4.6.: Final signal and background event yield [84, 77] in the ee channel for $384.1\,\mathrm{pb}^{-1}$of DØ Run II data reconstructed in `p14`. A top quark mass $m_{\mathrm{top}} = 175\,\mathrm{GeV}$ and $\sigma_{t\bar{t}} = 7\,\mathrm{pb}$ have been assumed. Both the statistical and systematic error are given. For all events a solution exists with the Neutrino Weighting Algorithm. The event yield stated for $WWjj \to e\mu\nu\nu jj$ includes the $WZjj$ process as well.

dropped as listed for the $e\mu$ channel. However, a slightly different approach is taken here. For both electrons the absence of a spatially matched track is allowed, but not required. Regarding this, the selected QCD background sample is made orthogonal "by hand", ruling out 2 events with the same run and event number as in the selected data sample. The QCD background selection yields 10 events.

In Tab. 4.6 the final yields for the ee channel determined using the DIEM skim of the $370\,\mathrm{pb}^{-1}$ dataset reconstructed with the `p14` version of DØ software are shown [84]. The control distribution plots are presented in Fig. 4.2. With the statistics available no problematic behaviour is observed. All events selected in the ee channel have solutions with the Neutrino Weighting Algorithm. A list of selected events with basic quantities of physics objects relevant for this analysis is presented in App. A.

The final yield for the $Z \to ee$ process has been determined using simulated Monte Carlo events up to the topological cuts. The efficiency of the combined Z-window and $\not\!\!E_T$ cut however has been determined in data due to a significant difference in the shape of jet p_T spectra in data and Monte Carlo and the resulting differences in the $\not\!\!E_T$ distribution. The efficiency of the consecutive sphericity cut was measured in Monte Carlo again.

The $\mu\mu$ Channel

As in the ee channel, the main background for the $\mu\mu$ channel is the $Z/\gamma^* jj \to \mu\mu jj$ process. A slightly different approach to discriminate it and the other backgrounds is taken here:

- The $Z \to \mu\mu$ background is rejected based on the χ^2 value of a kinematic fit of the event to a $Z \to \mu\mu$ process hypothesis: $\chi^2 > 2$. The exact definition of the χ^2 variable can be found in [54],
- The value of $\not\!\!E_T$ must be high to reject instrumental backgrounds: $\not\!\!E_T > 35\,\mathrm{GeV}$,
- A so-called "triangular" cut is applied to reject all backgrounds. This name refers to the shape of the cut in the $\not\!\!E_T$, $\Delta\phi(p_T^{\mu_1}, \not\!\!E_T)$ plane. The events with $\Delta\phi(p_T^{\mu_1}, \not\!\!E_T) \in [175°, 185°]$

Process	Event Yield	Stat. Err	Syst. Err
$Z/\gamma^* jj \to \mu\mu jj$	0.95	0.14	$^{+0.17}_{-0.31}$
$Z/\gamma^* jj \to \tau\tau jj$	0.15	0.02	$^{+0.08}_{-0.13}$
$WWjj \to \mu\mu\nu\nu jj$	0.20	0.03	$^{+0.08}_{-0.07}$
QCD	0.13	0.03	$^{+0.03}_{-0.03}$
total bgr	1.43	0.15	$^{+0.27}_{-0.39}$
expected sig	2.54	0.07	$^{+0.30}_{-0.30}$
selected events	2	–	–

Table 4.7.: Final signal and background event yield [84, 77] in the $\mu\mu$ channel for $362.6\,\mathrm{pb}^{-1}$of DØ Run II data reconstructed in `p14`. A top quark mass $m_{\mathrm{top}} = 175\,\mathrm{GeV}$ and $\sigma_{t\bar{t}} = 7\,\mathrm{pb}$ have been assumed. Both the statistical and systematic error are given. One of the selected events has no solution with the Neutrino Weighting Algorithm. The event yield stated for $WWjj \to e\mu\nu\nu jj$ includes the $WZjj$ process as well.

are discriminated against, as this region is densely populated by events with severely misreconstructed muons. Further, two corners of the plane are cut out, where the cut value for the $\not\!\!E_T$ linearly depends on the $\Delta\phi(p_T^{\mu_1}, \not\!\!E_T)$ value: $\not\!\!E_T > \Delta\phi(p_T^{\mu_1}, \not\!\!E_T) \cdot (-1\,\mathrm{GeV}) + 90\,\mathrm{GeV}$, $\not\!\!E_T > \Delta\phi(p_T^{\mu_1}, \not\!\!E_T) \cdot 1\,\mathrm{GeV} - 90\,\mathrm{GeV}$.

The QCD background is selected from the DIMU skim, by requiring anti-isolation for at least one of the leading muons: rat11 > 0.12, rattrk11 > 0.12. This requirement selects predominantly events with muons originating from electroweak decays in jets rather than coming from the primary interaction vertex. The selection requirements yield an appropriate sample for QCD background, since it must include processes where muons are produced in jets with a high p_T with respect to the jet momentum and with a resulting fake muon isolation to enter the selection. The final yield of the QCD background selection is 8 events.

The final yield for the $\mu\mu$ channel determined with the DIMU skim of the $370\,\mathrm{pb}^{-1}$ dataset reconstructed in `v14` is given in Tab. 4.7 [84]. In Fig. 4.3 the control distributions for various kinematic variables of physics objects as well as topological variables are presented. To within the statistics available no significant deviations between data and Monte Carlo prediction are observed. One of the selected events has no solution with the Neutrino Weighting Algorithm and is therefore dropped from further analysis. A list of selected events with basic quantities of physics objects relevant for this analysis is presented in App. A.

The figures for the $Z \to \tau\tau$ process are updated with respect to the cross section note [77]. In this note for the determination of the $Z \to \tau\tau$ selection efficiencies a mixture of samples with inclusive and leptonic τ decays has been used. Since the branching ratio for the former is 1 and 0.1239 for the latter, this results in a bias if no proper normalisation is applied. To fix this problem an event tagger on Monte Carlo truth level must be applied to select events where both τ-s decay leptonically, as pointed out in [77].

4.3.2. Selection Criteria for the $e\mu$ Channel of the 835 pb^{-1} Dataset

Decay candidates are selected [12, 13, 85] using most of the cuts employed by the $e\mu$ cross-section analysis [69]. The most important cut changes are:

- Added cut on the improved electron likelihood [86] of $\mathcal{L}_{\mathrm{EM}} > 0.85$ to significantly reduce instrumental backgrounds originally from electron mis-identification;
- Omitted cut on $\not\!\!E_T$ since it has a low figure of merit in the $e\mu$ channel.

Again, all event-wide quality and particle identification requirements are the same as in [69]. Unlike for the 370 pb^{-1}dataset, the instrumental background is not included in this part of the analysis (estimated to be 14% of the total background yield in Tab. 4.8). Below, a summary of the kinematic and particle identification selection cuts is given:

- Electron:
  - cut on the transverse momentum: $p_T(e) > 15$ GeV,
  - cut on the pseudorapidity: $|\eta| < 1.1$ or $1.5 < |\eta| < 2.5$,
  - require a high energy fraction in electromagnetic part of the calorimeter: $f_{\mathrm{EM}} > 0.9$,
  - isolated cluster in the electromagnetic calorimeter: $f_{\mathrm{iso}} < 0.15$,
  - shower shape cut: $\chi^2_{\mathrm{hmx7}} < 50$,
  - cut on the improved electron likelihood [86] discriminant $\mathcal{L}_{\mathrm{EM}} > 0.85$,
  - one track with $p_T > 5$ GeV matched to the EM cluster,
  - no common track with a muon,
  - veto on a second electron,
- Muon:
  - $p_T(\mu) > 15$ GeV, $|\eta| < 2$,
  - medium quality with required hits in layers A and B or A and C of the muon system,
  - timing cuts against cosmics,
  - matched with central track,
  - cut on Distance of Closest Approach (DCA): |DCA| < 0.02 cm for tracks with SMT hits, |DCA| < 0.2 cm for tracks without SMT hits,
  - Track and Calorimeter Isolation cuts: track_iso/$p_T < 0.15$ and energy_iso/$p_T < 0.15$,
- Electron and highest p_T muon in the event must have opposite charge,
- Require 2 or more jets with $p_T(j) > 20$ GeV and $|\eta| < 2.5$,
- $H_T^l = \max(p_T(e), p_T(\mu)) + p_T(j_1) + p_T(j_2) > 120$ GeV,

Applying the selection cuts results in 28 selected events for the $835\,\mathrm{pb}^{-1}$ dataset. They all produce solutions with the Neutrino Weighting Algorithm. A list of selected events with basic quantities of physics objects relevant for this analysis is presented in App. A. 15 events are selected in the $370\,\mathrm{pb}^{-1}$ dataset, 7 of them are the also selected with `p14`. This difference is due to improved reconstruction algorithms and quality criteria. The expected signal and background yields are presented in Tab. 4.8. For the signal part, they have been produced for a top quark mass of $m_{\mathrm{top}} = 175\,\mathrm{GeV}$ with an assumed cross section $\sigma_{\mathrm{top}} = 7\,\mathrm{pb}^{-1}$. The yield errors shown contain both the statistical and the systematic errors added in quadrature. The systematic error was calculated from the values stated in [69] by scaling them with the ratio of selected Monte Carlo events for a given sample. The expected signal-to-background ratio is approx. 3.85.

$t\bar{t} \to e\mu$	WW	$Z \to \tau\tau$	fake e	background	total	observed
20.2 ± 2.7	$1.24^{+2.2}_{-0.5}$	$2.7^{+1.5}_{-1.3}$	0.4 ± 0.2	$4.4^{+2.6}_{-1.4}$	$24.6^{+3.8}_{-3.0}$	28

Table 4.8.: Expected and observed $e\mu$ event yield for signal and background after application of all cuts as in [12, 13, 85]. For the signal, $\sigma_{t\bar{t}} = 7.0\,\mathrm{pb}$ and $m_{\mathrm{top}} = 175\,\mathrm{GeV}$ have been assumed. Both the statistical and the systematic error are included.

Control plots for data and Monte Carlo have been produced and are demonstrated in Fig. 4.4, as in [85]. To within the statistics available, no discrepancies are observed. It should be noted that in the sample supporting this analysis, DØ currently observes some disagreement between the expected yields estimated with Monte Carlo and observed in data in the 0- and 1-jet bin. An estimate on the systematic uncertainty associated with this number is given in Sec. 9.

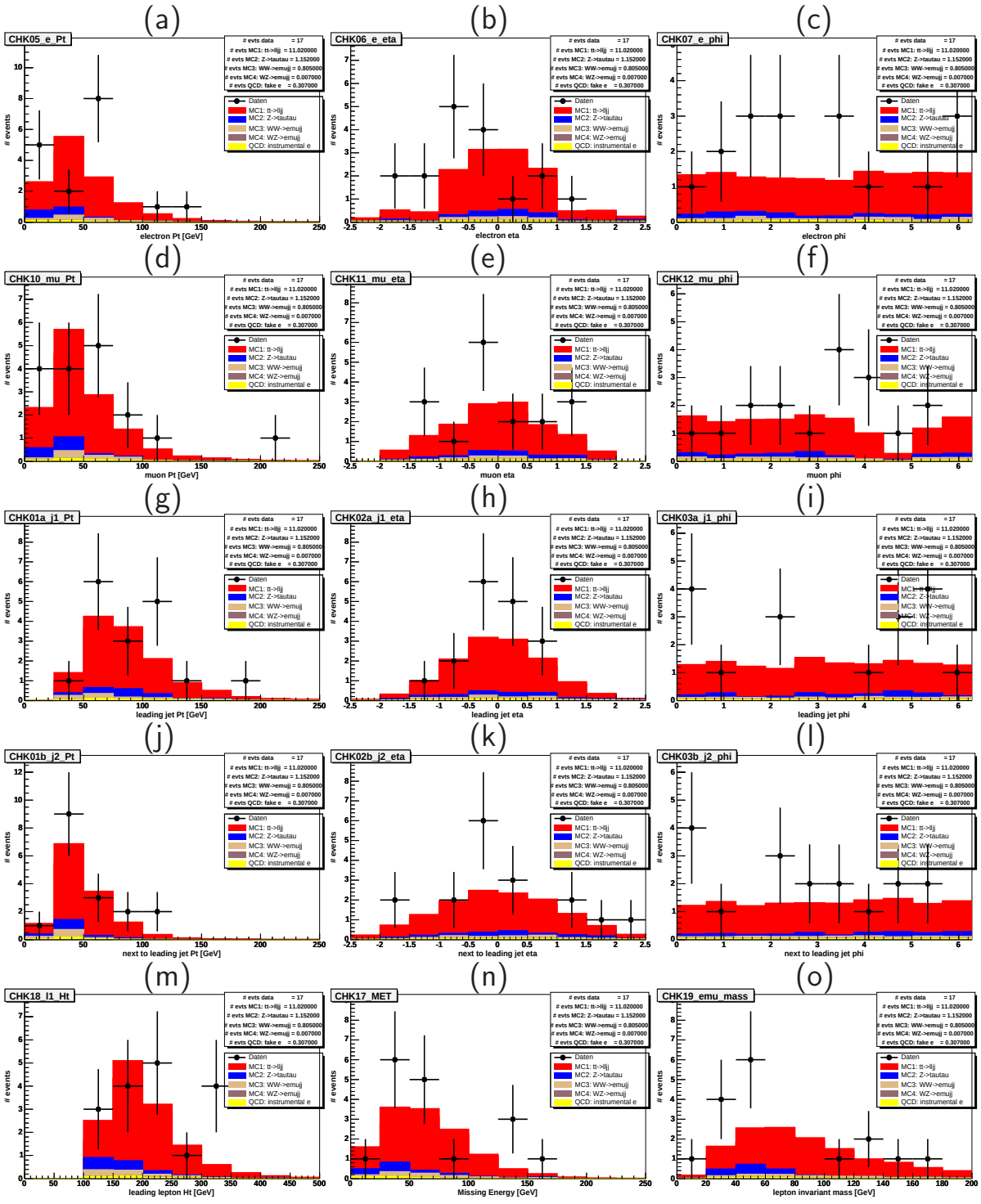

Figure 4.1.: Control plots for data and Monte Carlo for the $e\mu$ channel of the 370 pb^{-1} dataset, as in [84]:
(a), (b), (c) electron p_T, η, and ϕ
(d), (e), (f) muon p_T, η, and ϕ
(g), (h), (i) leading jet p_T, η, and ϕ
(j), (k), (l) next-to-leading jet p_T, η, and ϕ
(m), (n), (o) H_T^l, $\not{E}_T$, $m_{l_1 l_2}$.

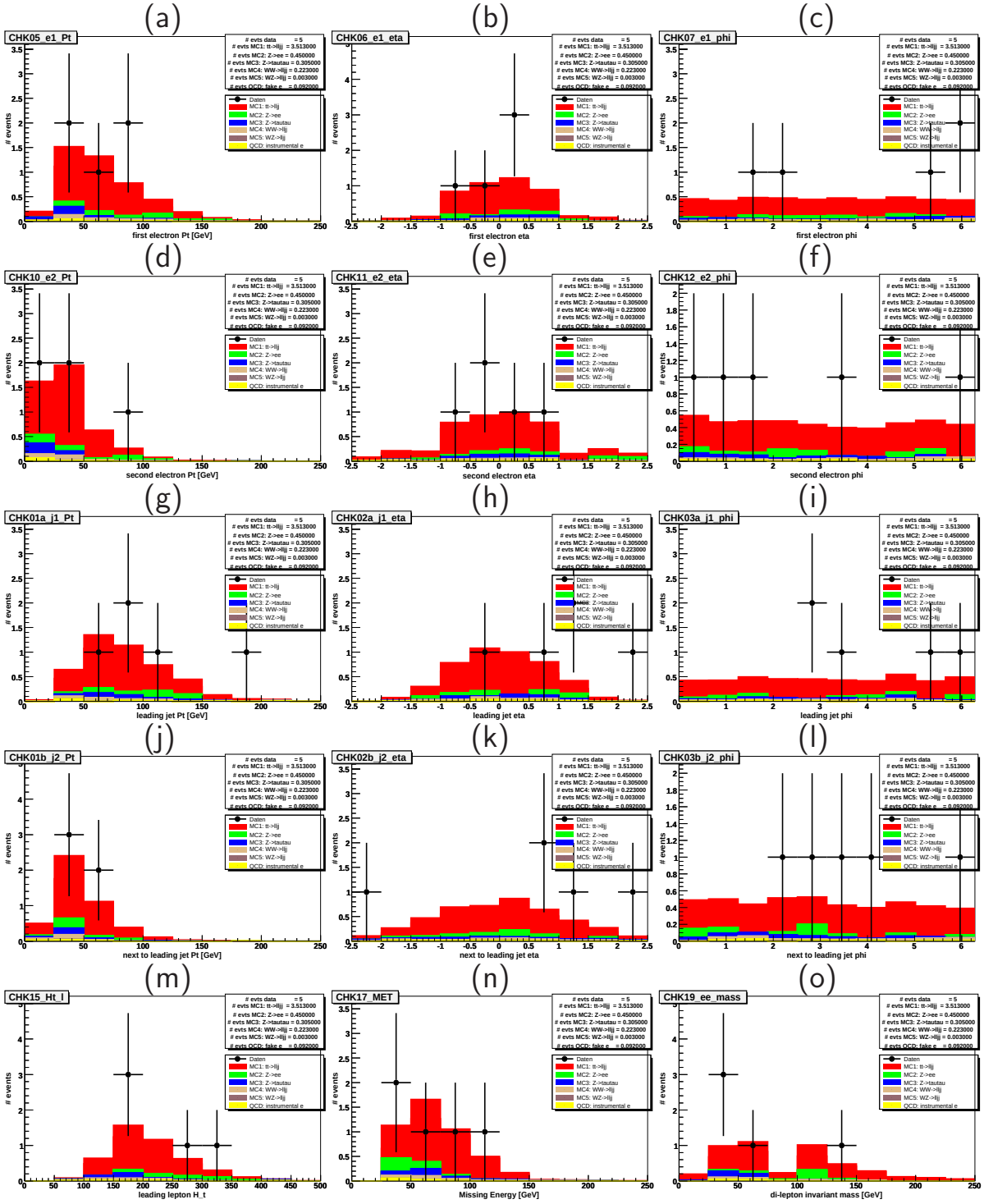

Figure 4.2.: Control plots for data and Monte Carlo for the *ee* channel of the $370\,\mathrm{pb}^{-1}$ dataset, as in [84]:
(a), (b), (c) leading electron p_T, η, and ϕ
(d), (e), (f) next-to-leading p_T, η, and ϕ
(g), (h), (i) leading jet p_T, η, and ϕ
(j), (k), (l) next-to-leading jet p_T, η, and ϕ
(m), (n), (o) H_T^l, $\not{E}_T$, $m_{e_1e_2}$.

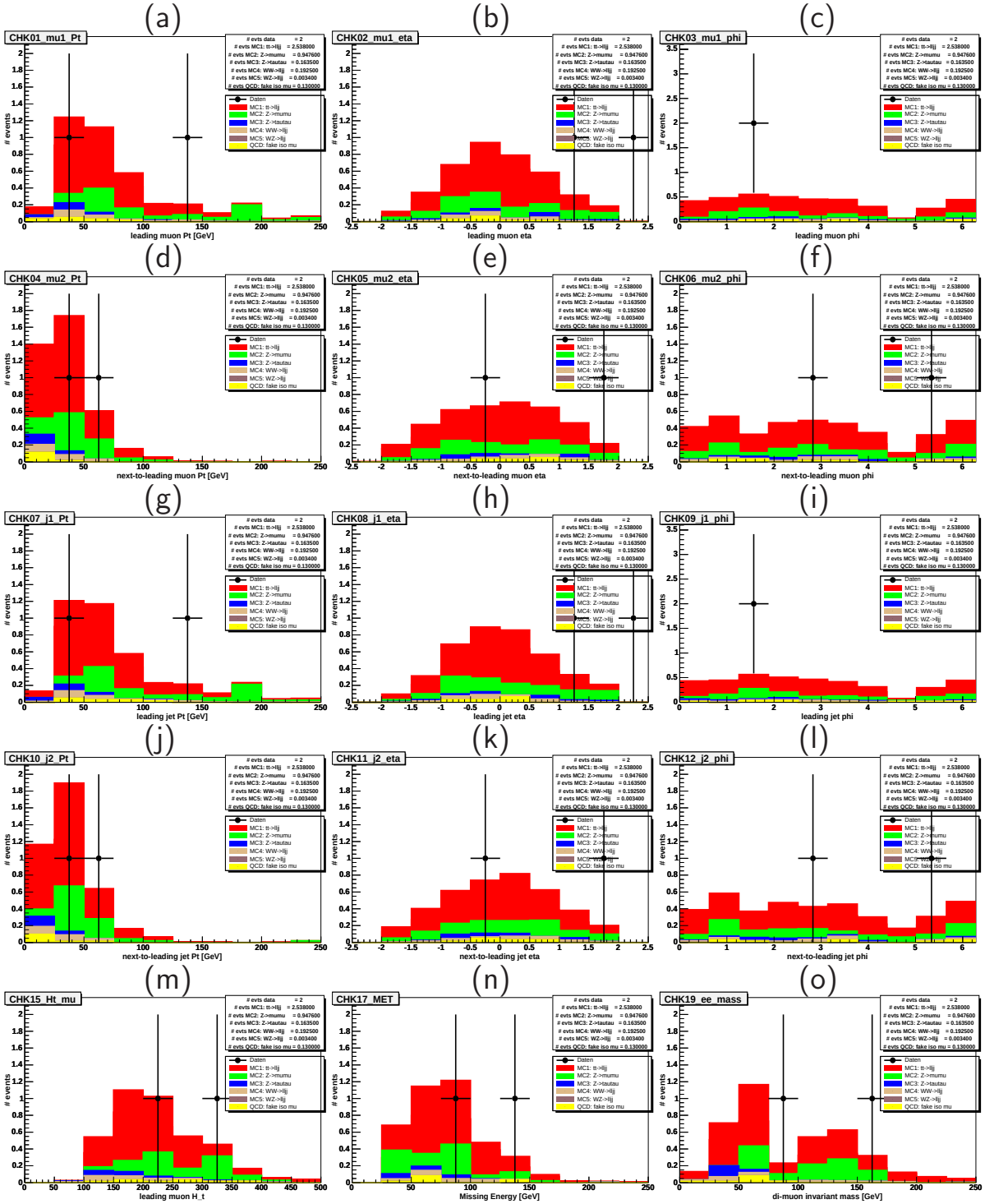

Figure 4.3.: Control plots for data and Monte Carlo for the $\mu\mu$ channel of the 370 pb^{-1} dataset, as in [84]:
(a), (b), (c) leading muon p_T, η, and ϕ
(d), (e), (f) next-to-leading muon p_T, η, and ϕ
(g), (h), (i) leading jet p_T, η, and ϕ
(j), (k), (l) next-to-leading jet p_T, η, and ϕ
(m), (n), (o) H_T^l, $\not\!\!E_T$, $m_{\mu_1\mu_2}$.

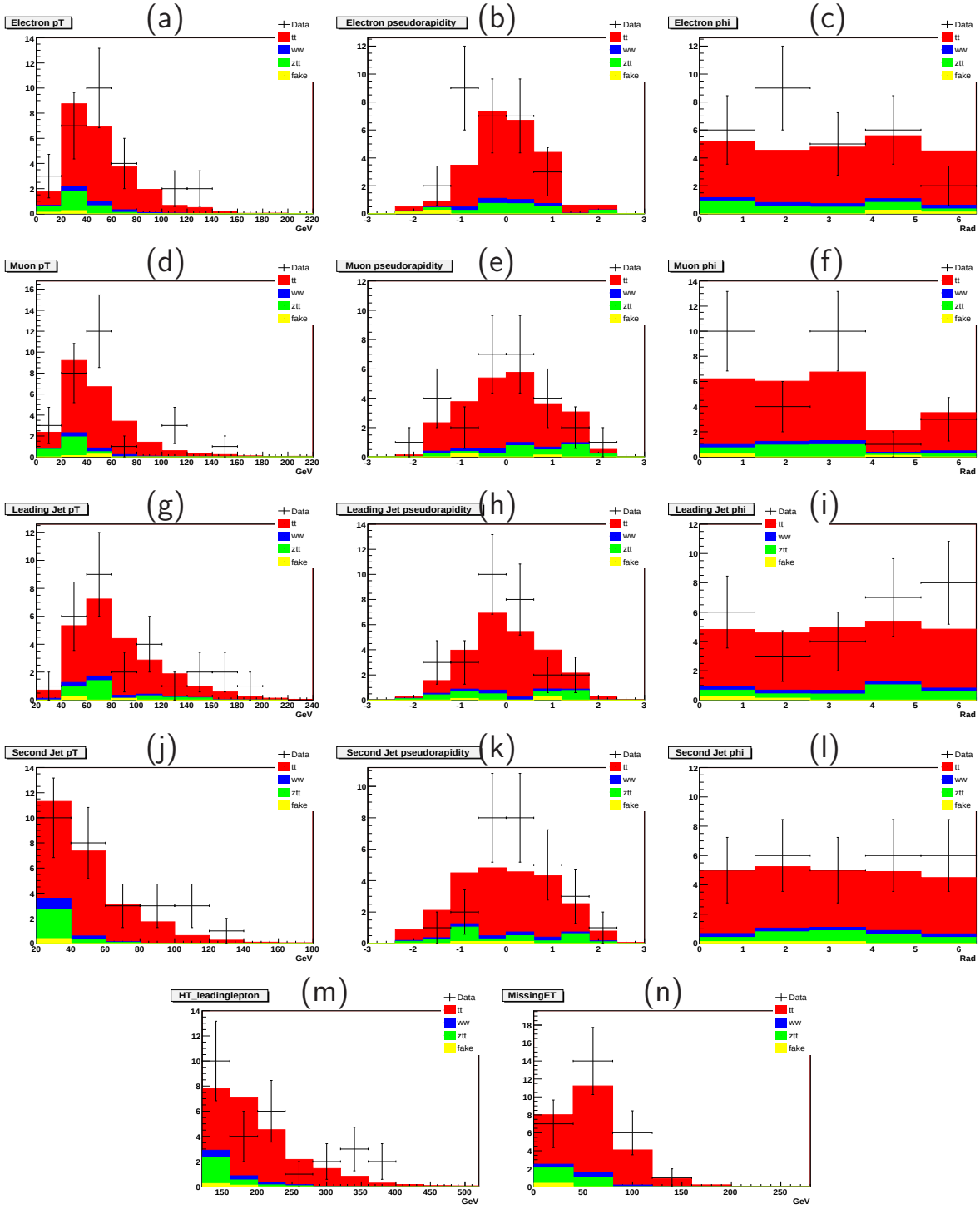

Figure 4.4.: Control plots for data and Monte Carlo for the $835\,\mathrm{pb}^{-1}$ dataset, as in [85]:
(a), (b), (c) electron p_T, η, and ϕ
(d), (e), (f) muon p_T, η, and ϕ
(g), (h), (i) leading jet p_T, η, and ϕ
(j), (k), (l) next-to-leading jet p_T, η, and ϕ
(m), (n) H_T^l, $\not{E}_T$.

5. The Neutrino Weighting Method

In this chapter the Neutrino Weighting algorithm will be introduced. It was suggested by Kondo [87, 88] in 1988, and successfully adapted by DØ in Run I [89, 90]. In Run II of the Tevatron, it has been used by both DØ and CDF [12, 13, 82, 91]. In this chapter, a special focus is placed on the characteristics of dileptonic $t\bar{t}$ decays and the Neutrino Weighting algorithm itself. The effect of the detector resolution will be discussed.

5.1. Characteristics of Dileptonic $t\bar{t}$ Decays

A general introduction to dileptonic $t\bar{t}$ decays was given in Chap. 2. Following its arguments, in the simplest scenario there will be 6 particles in the final state: 2 charged leptons (either $e\mu$, or ee, or $\mu\mu$), 2 neutrinos of the corresponding flavor, and two b-quarks. With the 4-momenta of these particles and their masses as a constraint this results in $6 \times (4-1) = 18$ degrees of freedom. In the detector, the 4-momenta of the charged leptons and the b-quarks are measured and $4 \times 3 = 12$ degrees of freedom are eliminated, provided the identification of the particles. Further, the $\not\!\!E_T^x$ and $\not\!\!E_T^y$ measurement supplies the transverse components of the sum of the two neutrino momenta: $p^x_{\nu\bar{\nu}}$ and $p^y_{\nu\bar{\nu}}$. This totals in 14 measured degrees of freedom being eliminated by measurement. Two additional constraints are supplied if input from the Standard Model is used and the masses of the W bosons are introduced:

$$m_{W^-} = m_{l^-\bar{\nu}} \quad \Rightarrow \quad m^2_{W^-} = (E_{\bar{\nu}} + E_{l^-})^2 - (\vec{p}_{\bar{\nu}} + \vec{p}_{l^-})^2 \tag{5.1}$$

$$m_{W^+} = m_{l^+\nu} \quad \Rightarrow \quad m^2_{W^+} = (E_{\nu} + E_{l^+})^2 - (\vec{p}_{\nu} + \vec{p}_{l^+})^2 \,. \tag{5.2}$$

If the equality of masses for the top and the anti-top quark is assumed, another constraint can be placed:

$$\begin{aligned} m_t = m_{\bar{t}} \quad &\Leftrightarrow \quad m_{l^+\nu b} = m_{l^-\bar{\nu}\bar{b}} \\ \Rightarrow (E_\nu + E_{l^+} + E_b)^2 - (\vec{p}_\nu + \vec{p}_{l^+} + \vec{p}_b)^2 \quad &= \quad (E_{\bar{\nu}} + E_{l^-} + E_{\bar{b}})^2 - (\vec{p}_{\bar{\nu}} + \vec{p}_{l^-} + \vec{p}_{\bar{b}})^2 \,. \end{aligned} \tag{5.3}$$

With Eqn. 5.1, 5.2, and (5.3) three more constraints are supplied and thus only one degree of freedom remains: one is facing a system of 17 equations with 18 unknown variables. This renders a simple kinematic fit impossible, different to the dileptonic $t\bar{t}$ decay channel to the lepton+jets or all-jets channel, where such a fit can be done. A statistical approach – the Neutrino Weighting Method – was developed to infer the mass of the top quark from the available information [87]. For each event a mass weight function is derived, which is a measure for the probability density for a $t\bar{t}$ pair to decay to the observed final state as a function of the hypothesised top quark mass.

The basic idea to extract the top quark mass is to compare the mass weight functions of the events in the data sample with the weight functions from simulated Monte Carlo events generated

for different top mass hypotheses. For this purpose the Maximum Likelihood Fit formalism combined with the so-called Maximum Method is applied, which will be introduced in Chap. 6.

5.2. The Mass Weight Function

In the ideal situation, the probability density for a $t\bar{t}$ pair to decay to a given final state described by the set of measured observables in the final state $\{v_{\text{meas}}\}$ given the mass of the top quark m_{top} would be computed analytically using the theoretical framework of the Standard Model. This probability is proportional to:

$$P(\{v_{\text{meas}}\}|m_{\text{top}}) \propto \int \mathrm{d}^{18}\Phi \mathrm{d}x \mathrm{d}\bar{x} \cdot f(x) f(\bar{x}) \cdot p(\{v_{\text{meas}}\}|\{v_{\text{part}}\}) \cdot \delta^4 \cdot |\mathcal{M}_{t\bar{t}\rightarrow \text{dilepton}}|^2 \,, \qquad (5.4)$$

where $\{v_{\text{part}}\}$ is the set of observables in the final state at parton level and $\mathrm{d}^{18}\Phi$ their differential. The matrix element $\mathcal{M}_{t\bar{t}\rightarrow \text{dilepton}}$ is understood to describe the process

$$q\bar{q},\, gg \rightarrow t\bar{t} + X \rightarrow l^- \bar{\nu} \bar{b} l^+ \nu b + \tilde{X}$$

with its full interference structure. $\tilde{X}$ denotes any additionally produced particles. The parton density functions for (anti-) quarks or gluons of momentum fraction x in the proton and for (anti-) quarks and gluons with momentum fraction $\bar{x}$ in the anti-proton are represented by $f(x)$ and $f(\bar{x})$, respectively. The mapping $p(\{v_{\text{meas}}\}|\{v_{\text{part}}\})$ gives the DØ-specific probability to measure the set of observables in the final state $\{v_{\text{meas}}\}$ given the set of observables at parton level $\{v_{\text{part}}\}$. The 4-dimensional δ-function represents the constraints of Eqn. 5.1, 5.2, and 5.3 in this calculation with the finite mass width of the W boson and the b-quark neglected:

$$\delta^4 := \delta(m_{W^-} - m_{l^-\bar{\nu}}) \times \delta(m_{W^+} = m_{l^+\nu}) \times \delta(m_t - m_{l^-\bar{\nu}\bar{b}}) \times \delta(m_t - m_{l^+\nu b}) \,.$$

In practice, the calculation of the probability $P(\{v_{\text{meas}}\}|m_{\text{top}})$ via Eqn. 5.4 is complicated and very intensive in terms of computation time, not only because the full matrix element has to be calculated, but because the full available phase space $\mathrm{d}^{18}\Phi$ has to be integrated over numerically. The situation is additionally complicated by the need to include the matrix elements for initial and final state radiation. Therefore, the Neutrino Weighting Method does not attempt to calculate Eqn. (5.4) precisely. Rather, a simpler weight is introduced which retains sensitivity to the top quark mass. The effects arising from this simplification are calibrated by comparing the weight functions in data to weight functions obtained with Monte Carlo. However, a Matrix Element dilepton analysis is in preparation at DØ, which will follow the approach described in the paragraph above using a simplified calculation for the full matrix element $\mathcal{M}_{t\bar{t}\rightarrow \text{dilepton}}$ and approximate integration techniques.

5.3. The Neutrino Weighting Method

The core of the Neutrino Weighting Method is that the unknown neutrino momentum components are not solved for, but rather the neutrino pseudorapidity space is sampled and a weight is calculated based on how consistent the sampled phase space is with the measured $\not\!\!E_T$ vector.

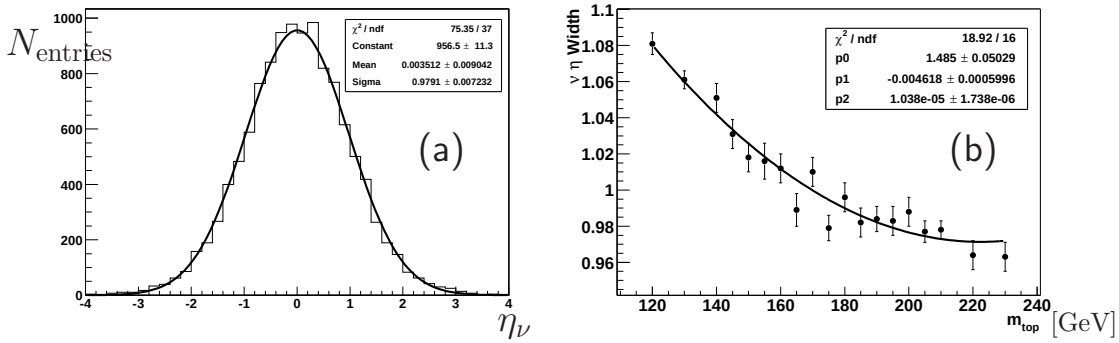

Figure 5.1.: (a): distribution of the neutrino pseudorapidity as determined for pure signal Monte Carlo for a top quark mass of $m_{\text{top}} = 175\,\text{GeV}$. (b): the dependence of the σ-parameter of Gaussian fits to neutrino pseudorapidity distributions for different top quark masses. Both plots are from [82].

Assuming values for the pseudorapitidy of the neutrino η_ν and the anti-neutrino $\eta_{\bar{\nu}}$, as well as for the top quark mass m_{top}, taking the measured momenta of the charged leptons and b-quarks, the missing transverse energy vector $\not{E}_T^{\text{calc}}$ is calculated and compared to the measured value $\not{E}_T^{\text{meas}}$. For each of the two neutrinos, 10 pseudorapidity assumptions are made in such a way, that each of them represents 1/10 of the total surface under the pseudorapidity distribution. That is, each assumption represents 10% of signal Monte Carlo events. The kinematical calculation of $\not{E}_T^{\text{calc}}$ [92] is lengthy but straight forward. It is given in App. B for reference. Since the calculation leads to two quadratic equations with up to 2 real solutions for each of the decaying top quarks, there is an up to 8-fold ambiguity, taking into account the two possible pairings of the charged leptons with jets. This pairing ambiguity is due to the fact that the charge of the jets resulting from the hadronization of the b-quarks is not measured. These two weights are summed with the assumption that the configuration closest to the situation at parton level will outweight any others.

For the i-th solution, the weight is calculated according to the formula

$$\omega_i(m_{\text{top}}) := \exp\left(\frac{-(\not{E}_x^{\text{calc}} - \not{E}_x^{\text{obs}})^2}{2\sigma^2_{\not{E}_x}}\right) \times \exp\left(\frac{-(\not{E}_y^{\text{calc}} - \not{E}_y^{\text{obs}})^2}{2\sigma^2_{\not{E}_y}}\right) . \tag{5.5}$$

This weight definition assumes the $\not{E}_T$ to be Gaussian distributed with σ-parameters $\sigma^2_{\not{E}_x}$, $\sigma^2_{\not{E}_y}$ in x and y direction. In other words, a weight is assigned depending on how consistent the $\not{E}_T^{\text{calc}}$ value resulting from the calculation is to the measured one. The σ-parameters are summarised in Sec. 5.4.

The assumptions for the neutrino pseudorapidities are made in the following way: it happens that the neutrino pseudorapidity is Gaussian distributed with a σ-parameter of approximately 1, as displayed on the left hand side of Fig. 5.1. On the right hand side of the same figure the weak dependence of the σ-parameter on the top quark mass is depicted. This dependence is parametrised as a quadratic function of the top quark mass:

$$\langle\eta\rangle(m_{\text{top}}) = 1.48 - (4.62 \times 10^{-3})m_{\text{top}} + (1.04 \times 10^{-5})m^2_{\text{top}}\,,$$

as found in [82].

The weight is calculated for 125 top quark mass hypotheses m_{top} ranging from 80 to 330 GeV in 2 GeV steps. For each of the top quark masses, the weights $\omega_i(m_{\text{top}})$ are summed over all

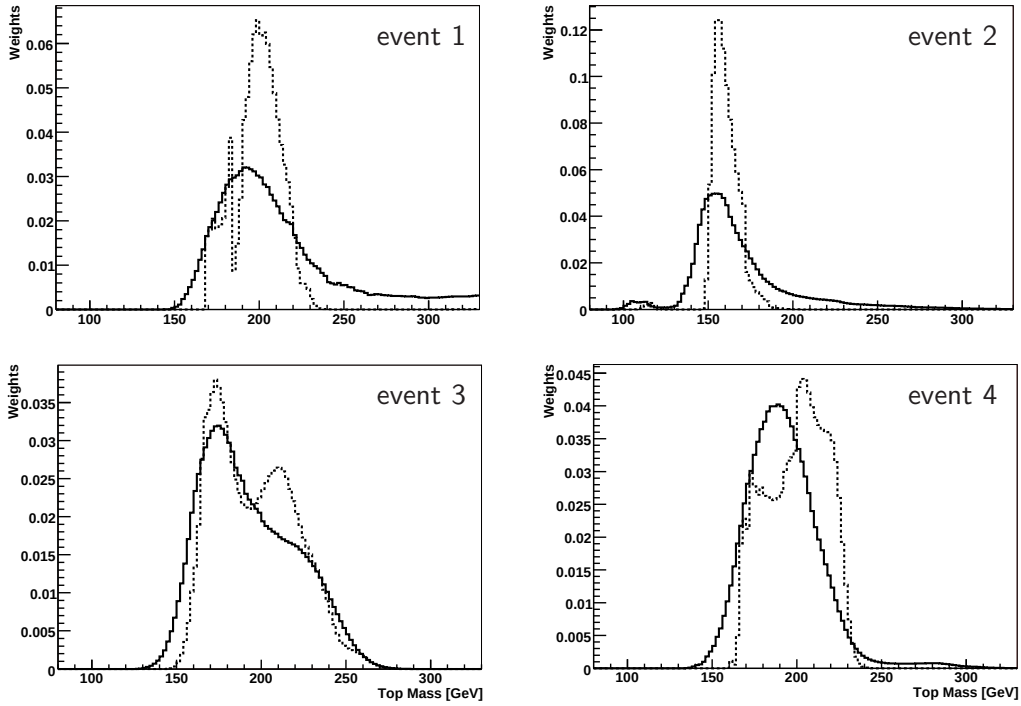

Figure 5.2.: Normalised mass weight distributions for randomly chosen signal Monte Carlo events with $m_{\text{top}} = 175$ GeV, as produced with the Neutrino Weighting Method. The dashed distribution has no detector smearing, while the solid distribution results when the physics objects of an event have been fluctuated according to their resolutions and the Neutrino Weighting algorithm has been applied for 150 times, see Sec. 5.4 for details.

$10 \times 10 = 100$ assumptions for the pseudorapidity of the neutrino and the anti-neutrino, and over up to 8 solutions resulting from the calculation of the $\not\!\!E_T$ and the ambiguity in lepton-jet assignment. Therefore, the total weight can be written as:

$$\omega(m_{\text{top}}) = \sum_{\eta_\nu} \sum_{\eta_{\bar{\nu}}} \sum_{i=1}^{8} \omega_i(m_{\text{top}}) \,. \tag{5.6}$$

Finally, the calculated weight is normalised to unity to ensure that all events are treated in an equal way.

Some examples of weight distributions for individual $t\bar{t}$ events with detector simulation are shown as dashed lines in Fig. 5.2. However, from these distributions it is not obvious that the weights produced by the Neutrino Weighting Method indeed retain a top quark mass dependence. This most important property is demonstrated in Fig. 5.3, where a sum over many normalised mass distributions is shown for signal Monte Carlo with a top quark mass of 160, 175, and 190 GeV. A correlation of the peak, the mean, and the shape of the distribution with the top quark mass is manifest. One of the methods to measure the top quark mass using the mass weight distribution produced by the Neutrino Weighting Method is the subject of this thesis – the Maximum Method. Other approaches at DØ based on the Neutrino Weighting Method can be found in [12, 13, 82].

There are two important prerequisites for the Neutrino Weighting Method to work:

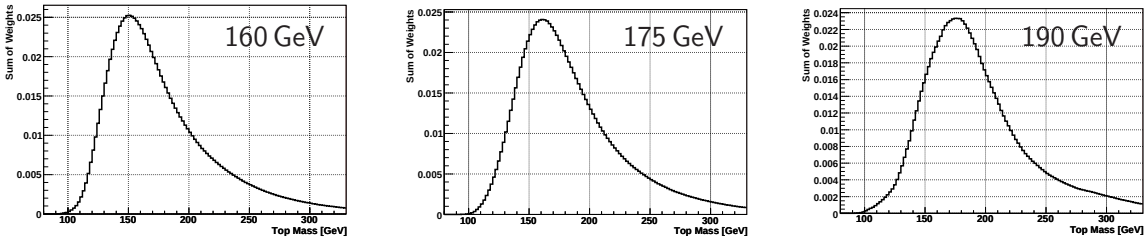

Figure 5.3.: Sum of event weights for $t\bar{t}$ Monte Carlo samples ($\mathcal{O}(10\,\text{k events})$) for a top quark mass of 160, 175, and 190 GeV.

- The Monte Carlo simulation must describe the same processes that produce the $t\bar{t}$ events in data; i.e., the assumptions made by the Standard Model are indeed realised in Nature.
- The kinematic properties of physics objects and their resolutions must be well-modelled in simulated Monte Carlo events. This is especially true as the $\not\!\!E_T$ reconstruction relies heavily on the measurement of the individual physics objects.

The first assumption is tested by the CDF and DØ $t\bar{t}$ cross section measurements in dilepton final states [37, 93], showing that the measured cross sections are consistent with the Standard Model expectation. However, in the $835\,\text{pb}^{-1}$ data sample supporting the analysis in this note, DØ currently observes some disagreement between observed yields in data and the expectation in the 0- and 1- jet bins, as detailed in Chap. 4. The second assumption above, concerning the modelling of quantities of physics objects and their resolutions, is also tested in [82].

5.4. Detector Resolutions in the Neutrino Weighting Method

The previous discussion of the weight curve calculation with the Neutrino Weighting Algorithm accounts for the detector resolution of the $\not\!\!E_T$ measurement, but it basically assumes that the physical quantities measured in the detector v_{meas} equate the quantities on parton level v_{part} and thus ignores the fact that jets and leptons may also be mis-measured.

To accommodate detector resolutions, the following approach is chosen: in each event all jets and leptons are independently fluctuated, or "smeared" according to their known resolutions, and the resulting kinematic configuration is solved with the Neutrino Weighting algorithm. This procedure is iterated N times and the resulting weight distributions for each iteration are added to obtain the total weight:

$$w_{\text{total}}(m_{\text{top}}) = \sum_{s=1}^{N} w_s(m_{\text{top}})\,,$$

where $w_s(m_{\text{top}})$ is the mass weight distribution as found for the s-th solution by virtue of Eqn. 5.6. The $\not\!\!E_T$ value of the event is corrected for the overall shift in the total momentum of jets and leptons due to the smearing. It is important to stress the difference in the use of the word "smearing" here with respect to the more conventional context – the generation of simulated Monte Carlo events.

If the procedure as described above is not applied, the weight distribution will be biased, since solutions which are consistent with the measured kinematics within the detector resolution are

not accounted for, even if they produce a higher weight. Moreover, some kinematics configurations of dileptonic $t\bar{t}$ events as measured in the detector will not have a solution with the Neutrino Weighting algorithm at all. The effect of smearing on the mass weight distribution can be seen for some randomly chosen signal Monte Carlo events in Fig. 5.2. The number of smears N was chosen to be 150 times for Monte Carlo events and 2000 times for data, as detailed in Chap. 8.

With the assumption that the observed value v is Gaussian distributed, its smearing to the new value $\tilde{v}$ is done in the following way:

$$\tilde{v} = v + \sigma_v \cdot x \,,$$

where σ_v is the resolution of v, and x a normal distributed variable. In the following, for the individual physics objects – electrons, muons, and jets – the corresponding smearing variables v will be named and their resolutions σ_v will be given. The smearing of a momentum 4-vector p^κ for a physics object is understood to be done depending on v in the following way: all of its components are recalculated for new $\tilde{v}$ after smearing.

5.4.1. Resolution Parameters for the 370 pb^{-1} Dataset and `p14`

In this section, the resolutions of the physics objects relevant for this analysis are summarised for the 370 pb^{-1} dataset reconstructed using version `p14` of the DØ software. All figures are from [94], unless stated otherwise.

Missing Transverse Energy Resolution

The resolution for the $\not\!\!E_T$ is not the most important variable for this analysis, since it affects only the width of the neutrino weight distribution. The weight defined in Eqn. 5.5 is calculated in the same way for both data and Monte Carlo, and it is in this sense that its influence is limited. Nevertheless, it is important that this value reflects the situation in data. The resolution for $\not\!\!E_T$ is parametrised in terms of scalar transverse energy S_T (the total energy of the event calculated from a scalar sum of all energy values measured by all detector components):

$$\begin{aligned} \sigma_{\not\!\!E_x} &= 6.85\,\text{GeV} + 0.035 \cdot S_T\,[\text{GeV}] \\ \sigma_{\not\!\!E_y} &= 7.43\,\text{GeV} + 0.021 \cdot S_T\,[\text{GeV}]\,. \end{aligned}$$

Electron Smearing

For an electron energy larger than approximately 15 GeV a more precise measurement of this observable can be obtained by using the calorimeter rather than the tracker. Therefore, the resolution for the electron energy is parametrised ac codring to Eqn. 3.3 as:

$$\sigma(E_e) = C \oplus \frac{S}{\sqrt{E_e}} \oplus \frac{N}{E_e}\,,$$

where C is the constant, S the signal and N the noise parameter. The $\oplus$-sign implies a Gaussian (quadratic) sum. The parameters are dependent on the η_{det} of the electron. The table below summarises them:

Range	C	S [$\sqrt{\text{GeV}}$]	N [GeV]
$\lvert\eta_{\text{det}}\rvert < 1.1$	0.044	0.23	0.21
$1.5 < \lvert\eta_{\text{det}}\rvert < 2.1$	0.032	0.26	0.20

Muon Smearing

The momentum of the muon is measured in the central tracker and in the muon system. The resolution of the muon transverse momentum is parametrised according to Eqn. 3.2 as:

$$\frac{\sigma_{p_T}}{p_T} = C \cdot p_T \oplus S\,,$$

where C again is the constant parameter, whereas S is the parameter for the sampling term. Their η_{det}-dependence is documented below:

Range	C [$\sqrt{\text{GeV}}$]	S
$\lvert\eta_{\text{det}}\rvert < 1.62$	0.00152	0.0279
$\lvert\eta_{\text{det}}\rvert > 1.62$	0.00226	0.0479

Jet Smearing

The jets are measured in the calorimeter. Therefore, the resolution for their transverse momentum is parametrised in the same way as in Eqn. (3.3) for electrons. Below, the parameters as they apply to jets are given:

Range	C	S [$\sqrt{\text{GeV}}$]	N [GeV]
$\lvert\eta_{\text{det}}\rvert < 0.5$	0.0893	0.753	5.05
$0.5 < \lvert\eta_{\text{det}}\rvert < 1.0$	0.0870	1.200	0.00
$1.0 < \lvert\eta_{\text{det}}\rvert < 1.5$	0.1350	0.924	2.24
$1.5 < \lvert\eta_{\text{det}}\rvert$	0.0974	0.000	6.42

5.4.2. Resolution Parameters for the 835 pb^{-1} Dataset and `p17`

In this section, the resolutions are summarised for the 835 pb^{-1} dataset reconstructed using version `p17` of DØ software. For the muons the old resolutions have been used. This is a minor effect compared to the energy resolution of the jets.

Missing Transverse Energy Resolution

The $\not\!\!E_T$ resolution for `p17` was obtained by examining $Z + 2j$ events. Such events were selected in data and in Monte Carlo. In both cases the $\not\!\!E_T$ resolution was studied as a function of the *unreconstructed* scalar E_T of an event. No dependence was found, therefore a constant resolution of $\sigma_{\not\!\!E_T} = 10.9\,\text{GeV}$ is used [95]. The larger size of the error with respect to `p14` and the fact

that it is constant is due to the fact, that the parametrisation was tried using the *unclustered* energy deposit in the calorimeter, without taking into account reconstructed physics objects, i.e. electrons, muons and jets. Meanwhile better approaches to parametrise the $\not\!\!E_T$ resolution have been found. The $\not\!\!E_T$ resolution is the same for the x and y direction, which is mainly due to the calibration of the calorimeter in `p17`.

Electron Smearing

The resolution of electrons used in this analysis was determined for the central calorimeter $|\eta_{\text{det}}| < 1.1$ and both of the endcaps $1.5 < |\eta_{\text{det}}| < 2.5$ separately in [96, 97]. The electron resolution is calculated according to the Eqn. 3.3, with the sampling term given as a quadratic sum of the corresponding error terms for the preshower and the electromagnetic calorimeter. With `p17` the resolution is parametrised using a sophisticated function which takes into account the η_{phys} dependence of the resolution reflecting the η_{phys} dependence of the projected length of dead material a particle traverses. The exact form of this parametrisation is not given here, as it would exceed the scope of this thesis.

Jet Smearing

The resolution of jets with `p17` was calculated using jet transfer functions derived with Monte Carlo events. For the same reason as above, the parameters and further details are not given here. They can be found in [98].

6. The Maximum Method for the Top Quark Mass Extraction

A standard method to extract an estimate for a physical quantity like the top quark mass is the so-called Maximum Likelihood Fit [99]. In this chapter the likelihood function will be defined. A special focus is placed on the part of the likelihood responsible for the actual top quark mass extraction – the core of the Maximum Method.

6.1. Likelihood Definition

Despite the high signal-to-background ratio in dilepton final states, the background fraction has to be accounted for. This is done by fitting the number of signal and background events when maximising the likelihood with respect to the test top quark mass $m_{\text{top}}^{\text{test}}$. Regarding this, the per-channel likelihood is defined as

$$\mathcal{L}(m_{\text{top}}^{\text{test}}) := \mathcal{L}_{\text{Gauss}} \cdot \mathcal{L}_{\text{Poisson}} \cdot \mathcal{L}_{\text{shape}}(m_{\text{top}}^{\text{test}}) \,.$$

The *Gaussian* constraint,

$$\mathcal{L}_{\text{Gauss}}(n_{\text{bgr}}, \bar{n}_{\text{bgr}}, \sigma_{\text{bgr}}) := \frac{1}{\sqrt{2\pi}\sigma_{\text{bgr}}} e^{-(n_{\text{bgr}}-\bar{n}_{\text{bgr}})^2/2\sigma_{\text{bgr}}^2} \,,$$

forces consistency between the fitted number of background events, n_{bgr}, and their expected number, $\bar{n}_{\text{bgr}} \pm \sigma_{\text{bgr}}$, as determined in the cross section analyses. This accounts for the fact, that the error on the number of background events in the analysed data sample σ_{bgr} is finite due to systematic effects. These errors are Gaussian, and assymmetric yield errors given in Tab. 4.5, 4.6, 4.7, 4.8 are symmetrised using the arithmetic mean. The expected number of background events is the sum of individual backgrounds: $\bar{n}_{\text{bgr}} := \sum_i \bar{n}_{\text{bgr}_i}$, where i indexes the background sources for a given channel. Its error is a quadratic sum of the individual yield errors: $\sigma_b := \sum_i^{\oplus} \sigma_{\text{bgr}_i}$.

The *Poisson* constraint on the likelihood,

$$\mathcal{L}_{\text{Poisson}}(n_{\text{sig}} + n_{\text{bgr}}, N) := \frac{(n_{\text{sig}} + n_{\text{bgr}})^N e^{-(n_{\text{sig}}+n_{\text{bgr}})}}{N!} \,,$$

requires agreement between the observed number of events in the selected sample, N, and the total number of signal and background events $n_{\text{sig}}+n_{\text{bgr}}$. This part of the likelihood is introduced to account for the fact, that the number of selected events is subject to Poisson fluctuations.

The most essential part of the likelihood, $\mathcal{L}_{\text{shape}}$, sets up a relation between the Neutrino Weighting Algorithm and the top quark mass to be measured. The general strategy is the following: a finite vector of physical observables, $\vec{w}$, is defined to extract the information contained in the event weight distribution calculated with the Neutrino Weighting Algorithm. For this vector, the signal and background probability density functions, $f_{\text{sig}}(\vec{w} \mid m_{\text{top}}^{\text{test}})$ and $f_{\text{bgr}}(\vec{w})$, are calculated. It is important to note, that the signal probability function is evaluated for a given $m_{\text{top}}^{\text{test}}$, which introduces the dependence on the top quark mass.

Following these arguments, the $\mathcal{L}_{\text{shape}}$ part of the likelihood is defined as:

$$\mathcal{L}_{\text{shape}}(n_{\text{sig}}, n_{\text{bgr}}, m_{\text{top}}^{\text{test}}) := \prod_{i=1}^{N} \frac{n_{\text{sig}} f_{\text{sig}}(\vec{w}_i \mid m_{\text{top}}^{\text{test}}) + n_{\text{bgr}} f_{\text{bgr}}(\vec{w}_i)}{n_{\text{sig}} + n_{\text{bgr}}} \,.$$

For each event $i = 1, \ldots N$ in the sample the signal $f_{\text{sig}}(\vec{w}_i \mid m_{\text{top}}^{\text{test}})$ and background probability distribution $f_{\text{bgr}}(\vec{w}_i)$ are evaluated. The signal and background probability distribution functions are scaled by their relative contributions, n_{sig} and n_{bgr}.

To maximise the total likelihood, the following approach is chosen: instead of the likelihood function its negative logarithm $-\ln \mathcal{L}$ is taken, and is minimised with respect to the top quark mass. This is a valid approach, since the logarithm is a strictly monotonously rising function and thus bijective. The minimisation is done by calculating the logarithmic likelihood for a set of test top quark masses $m_{\text{top}}^{\text{test}}$ and performing a cubic fit to the resulting points. In the limit of infinite statistics and for a Gaussian distributed quantity the logarithmic likelihood is expected to take a parabolic shape [99]. A cubic fit accounts for possible deviations from this ideal case, which come about through an asymmetric form of the signal and background distribution function, but also the presence of background events. The number of fitted points is chosen to be 7, centred around the three neighbouring points of the likelihood to give the lowest sum of their $-\ln \mathcal{L}$ values. The number of fitted points corresponds to a total fit range of 15 GeV. This fit range value was found in an optimisation process with a small estimator bias being the figure of merit. Smaller fit range values tend to yield unstable results due to a small number of fitted points. With larger fit range values the likelihood is evaluated in the regions far away from the minimum, where distortions from the expected parabolic shape start to take a strong effect. The best estimate for the top quark mass $\hat{m}_{\text{top}}$ is the minimum of the fit to the likelihood points. The best estimate for the statistical uncertainty $\hat{\sigma}_{m_{\text{top}}}$ is the distance from the estimated top quark mass $\hat{m}_{\text{top}}$ to a top quark mass where the value of the negative logarithmic likelihood is half a unit higher than the minimal value $-\ln \mathcal{L}(\hat{m}_{\text{top}})$ [99]. When calculating the $-\ln \mathcal{L}$ value for each of the individual $m_{\text{top}}^{\text{test}}$ points, it is minimised using the MINUIT package [100] with respect to the free parameters n_{sig} and n_{bgr}.

6.2. The Maximum Method

With the likelihood function defined, a vector of input variables $\vec{w}$ remains to be chosen that characterises the weight distributions. Currently, DØ uses three such vectors [12, 13]:

- In the *Binned Template Method* a 4-dimensional event weight vector is analysed, obtained by coarsely re-binning the normalised event weight distribution into 5 bins of 50 GeV width

each and taking their values. The 5-th bin is dropped, since it is redundant due to the overall normalisation to unity. This method strongly relies on the shape of the event weight distribution.

- The *Moments Method* takes the mean and the root mean square, i.e. the first two moments of the weight distribution, which show a top quark mass dependence.
- The *Maximum Method* uses the maximum of the event weight distribution, which by definition is the top quark mass value most consistent with the kinematic configuration of the analysed event.

In this thesis, the third approach – the Maximum Method – is presented. In the following, the maximum of the weight distribution will be referred to as "reconstructed mass"

$$\vec{w} \equiv w := m^{\mathrm{rec}} .$$

For the events presented in Fig. 5.2, these are the values 192, 158, 176, 188 GeV, going from left to right and from top to bottom. Accordingly, the signal and background probability density functions are formed for the $\mathcal{L}_{\mathrm{shape}}$ part of the likelihood in terms of the reconstructed mass: $f_{\mathrm{sig,bgr}}(\vec{w}) := f_{\mathrm{sig,bgr}}(m^{\mathrm{rec}})$. The big advantage of the Maximum Method is that the signal and background probability density functions can be obtained in an analytic form with a reasonable effort by fitting. For the other two approaches, at the current stage of the analysis, the Probability Density Estimation (PDE) algorithm [101] is used to smooth the $m_{\mathrm{top}}^{\mathrm{rec}}$ dependence of the signal and background probability density functions. Problems arising with this approach are discussed in Sec. 6.4.

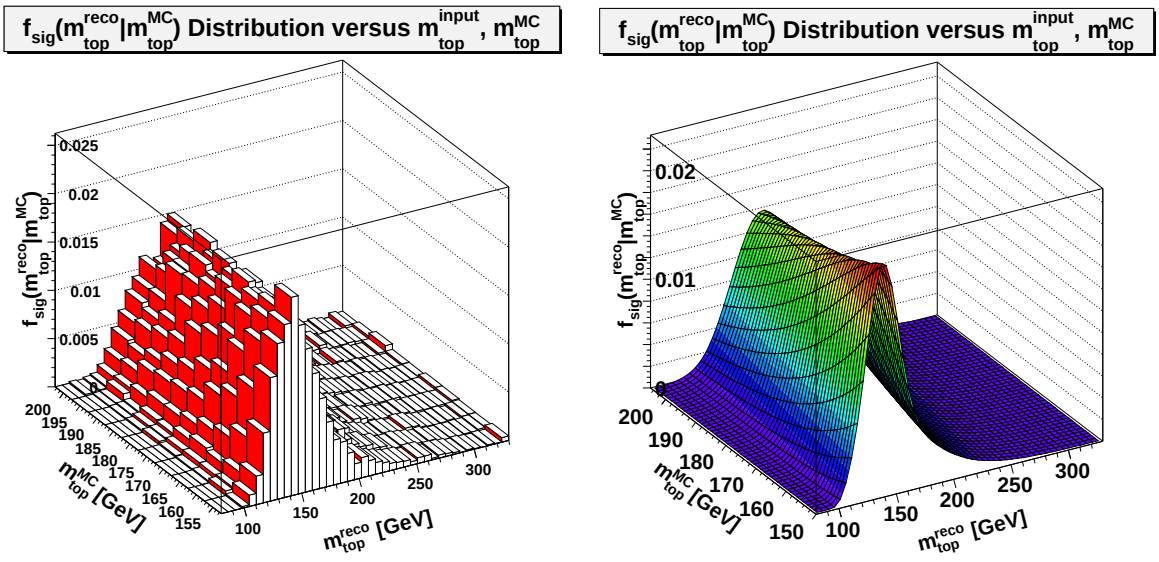

Figure 6.1.:
(left): combined histogram of reconstructed top quark masses $m_{\mathrm{top}}^{\mathrm{rec}}$ for different generated MC masses $m_{\mathrm{top}}^{\mathrm{MC}}$;
(right): fitted 2-dimensional signal probability distribution $f_{\mathrm{sig}}(m^{\mathrm{rec}}, m_{\mathrm{top}}^{\mathrm{MC}})$.

The signal probability density function f_{sig} is obtained in two steps:

- First, for each generated signal Monte Carlo mass point $m_{\mathrm{top}}^{\mathrm{MC}}$ a histogram is filled with reconstructed masses for all of its events. In the limit of infinite statistics and ideal Monte Carlo, this histogram corresponds to the $f_{\mathrm{sig}}(m^{\mathrm{rec}}|m_{\mathrm{top}}^{\mathrm{MC}})$ distribution, i.e. the $f_{\mathrm{sig}}(m^{\mathrm{rec}})$ distribution evaluated for a given generated Monte Carlo test top quark mass $m_{\mathrm{top}}^{\mathrm{MC}}$.
- In the next step, these histograms are combined for all available generated Monte Carlo top quark masses, e.g. $(m_{\mathrm{top}}^{\mathrm{MC}})_i = 155, \ldots 200\,\mathrm{GeV}$, which for the limit infinite statistics and infinitely small binning of generated Monte Carlo masses ($(m_{\mathrm{top}}^{\mathrm{MC}})_{i+1} - (m_{\mathrm{top}}^{\mathrm{MC}})_i \ll 1\,\mathrm{GeV}$) yields the 2-dimensional signal probability distribution $f_{\mathrm{sig}}(m^{\mathrm{rec}}, m_{\mathrm{top}}^{\mathrm{MC}})$. For the $e\mu$ channel of the `p17` version of DØ software this results in the plot on the left hand side of Fig. 6.1.

As the reality is far away from the ideal case described above, the 2-dimensional histogram is parametrised to approximate $f_{\mathrm{sig}}(m^{\mathrm{rec}}, m_{\mathrm{top}}^{\mathrm{MC}})$ by fitting it with an analytic function.

For a fixed $m_{\mathrm{top}}^{\mathrm{MC}}$, the signal probability density distribution is formed by the sum of a Gaussian and a dΓ part, which integrated gives the analytic Gamma-function:

$$f_{\mathrm{sig}}(m^{\mathrm{rec}}|m_{\mathrm{top}}^{\mathrm{MC}}) := \frac{\mathrm{d}\Gamma}{\mathrm{d}m^{\mathrm{rec}}}(m^{\mathrm{rec}}|m_{\mathrm{top}}^{\mathrm{MC}}) + g(m^{\mathrm{rec}}|m_{\mathrm{top}}^{\mathrm{MC}})\,, \tag{6.1}$$

with

$$\frac{\mathrm{d}\Gamma}{\mathrm{d}m^{\mathrm{rec}}}(m^{\mathrm{rec}}|m_{\mathrm{top}}^{\mathrm{MC}}) := \alpha_5 \cdot \frac{\alpha_2^{1+\alpha_1}}{\Gamma(1+\alpha_1)} \cdot (m^{\mathrm{rec}} - \alpha_0)^{\alpha_1} \exp(-\alpha_2(m^{\mathrm{rec}} - \alpha_0)) \cdot \Theta(m^{\mathrm{rec}} - \alpha_0)\,, \tag{6.2}$$

and the Gaussian part

$$g(m^{\mathrm{rec}}|m_{\mathrm{top}}^{\mathrm{MC}}) := (1-\alpha_5) \cdot \frac{1}{\alpha_4\sqrt{2\pi}} \exp\left(-\frac{(m^{\mathrm{rec}} - \alpha_3)^2}{2\alpha_4^2}\right)\,. \tag{6.3}$$

Here, $\Theta(x)$ is the Heaviside-function ($\Theta(x) = 1$ for $x \geq 0$, and $\Theta(x) = 0$ else). Up to the relative weighting factors α_5 and $(1-\alpha_5)$, $\alpha_5 \in [0,1]$ both the Gaussian and the dΓ part are normalised to unity. This particular choice of fitting functions was not derived by theoretical considerations, rather it was empirically found to describe the distribution well, as it consists of a central Gaussian peak part and an asymmetric part with a polynomial rise and an exponential decline. The idea for the functional form was inspired by [91]. Examples for the one-dimensional form of the signal probability density function for several generated top quark masses $m_{\mathrm{top}}^{\mathrm{MC}}$ are displayed in Fig. 6.4 for the $e\mu$ channel and `p17`.

The 2-dimensional signal probability density function $f_{\mathrm{sig}}(m^{\mathrm{rec}}, m_{\mathrm{top}}^{\mathrm{MC}})$ is formed from the 1-dimensional probability density function $f_{\mathrm{sig}}(m^{\mathrm{rec}}|m_{\mathrm{top}}^{\mathrm{MC}})$ by introducing a linear dependence of the parameters on the generated Monte Carlo top quark mass:

$$\alpha_i(m_{\mathrm{top}}^{\mathrm{MC}}) = \widetilde{\alpha}_i^0 + \widetilde{\alpha}_i^1 \cdot m_{\mathrm{top}}^{\mathrm{MC}}\,,\ i = 0, \ldots 5\,. \tag{6.4}$$

In fact, the particular functional form for $f_{\mathrm{sig}}(m^{\mathrm{rec}}|m_{\mathrm{top}}^{\mathrm{MC}})$ was chosen to allow this simple dependence for each of the parameters. Thus, when fitting the 2-dimensional histogram of reconstructed masses, a 2-dimensional fit with 12 free parameters $\tilde{\alpha}_i^j$, $i = 0, \ldots 5$, $j = 0, 1$ is performed.

The 2-dimensional histogram and the fit function are depicted in Fig. 6.1 for the $e\mu$ channel and the `p17` version of the DØ software. The 1-dimensional histograms of reconstructed masses and the 1-dimensional signal probability density function resulting from a 2-dimensional fit are shown in Fig. 6.4 for generated MC masses $m_{\mathrm{top}}^{\mathrm{MC}} = 155,\ 165,\ 175,\ 185,\ 200\,\mathrm{GeV}$ in the $e\mu$ channel and `p17`. The corresponding plots for $m_{\mathrm{top}}^{\mathrm{MC}} = 150,\ 165,\ 175,\ 185,\ 200\,\mathrm{GeV}$ for `p14` are depicted in Fig. 6.5, 6.6, and 6.7 for the $e\mu$, ee, and $\mu\mu$ channel, respectively. In all plots, as a blue fine-binned histogram line the result of the PDE approach to obtain the signal probability density function is shown. The fit parameter values for the $f_{\mathrm{sig}}(m_{\mathrm{top}}^{\mathrm{rec}}, m_{\mathrm{top}}^{\mathrm{MC}})$ are presented in the left hand side of Tab. 6.1.

The procedure for obtaining the background probability density distribution $f_{\mathrm{bgr}}(m^{\mathrm{rec}})$ is similar to the treatment of the signal. The main difference to the signal probability distribution is that now by definition there is no dependence on the top quark mass. Therefore for the $e\mu$ channel and the `p17` version of DØ software the same functional form as for the one-dimensional $f_{\mathrm{sig}}(m^{\mathrm{rec}}|m_{\mathrm{top}}^{\mathrm{MC}})$ function is chosen, dropping the linear dependence on $m_{\mathrm{top}}^{\mathrm{MC}}$ for the fit parameters: $\alpha_i(m_{\mathrm{top}}^{\mathrm{MC}}) \equiv \alpha_i$. However, for all dileptonic channels in `p14`, the available Monte Carlo statistics is not sufficient for such a fit with the functional form of Eqn. (6.1). The fit is overconstrained with too many degrees of freedom and thus unstable. Therefore, the Gaussian part (6.3) of the functional form is dropped by setting $\alpha_5 \equiv 1$ and the background density function is fitted with Eqn. (6.2) only.

To obtain the $f_{\mathrm{bgr}}(m^{\mathrm{rec}})$ function in a fit, one representative distribution of reconstructed masses for the background is used. It is comprised of reconstructed mass distributions for the individual backgrounds scaled according to their yields. This representative distribution is produced in the following way: one starts with the individual probability density distributions for each of the backgrounds, which are normalised to unity. In the next step, the individual probability density distributions are scaled relative to their expected yields $\hat{Y}$ with the factors

$$A_{\mathrm{bgr}_i} = \hat{Y}_{\mathrm{bgr}_i} / \sum_j \hat{Y}_{\mathrm{bgr}_j}$$

and added together. Their Poisson errors are scaled by the same normalisation factors. The resulting representative background distribution is fitted to yield the $f_{\mathrm{bgr}}(m^{\mathrm{rec}})$ function. The yields are as described in Chap. 4. The background density distribution is shown on the right bottom plot in Fig. 6.4 for the $e\mu$ channel in `p17` and in Fig. 6.5, 6.6, 6.7 for the $e\mu$, ee, and $\mu\mu$ channel in `p14`, respectively. The fit parameters for the $f_{\mathrm{bgr}}(m^{\mathrm{rec}})$ function are given on the right hand side of Tab. 6.1.

6.3. Discussion of the 2-dimensional Fit Approach

With the signal and background probability density distribution functions given in an analytic form as presented above, the likelihood can be calculated for *any* combination of m^{rec}, $m_{\mathrm{top}}^{\mathrm{MC}}$. In this sense one cannot strictly speak about a Monte Carlo test top quark mass $m_{\mathrm{top}}^{\mathrm{MC}}$. Nevertheless, the wording will be kept to avoid confusion. Regarding the analytic form of the likelihood, additional points are introduced between each two generated Monte Carlo mass points such that the step size for evaluation of $-\ln\mathcal{L}$ is 2.5 GeV. Another 3+3 points with the same step size are introduced to the left and to the right of the generated Monte Carlo mass range,

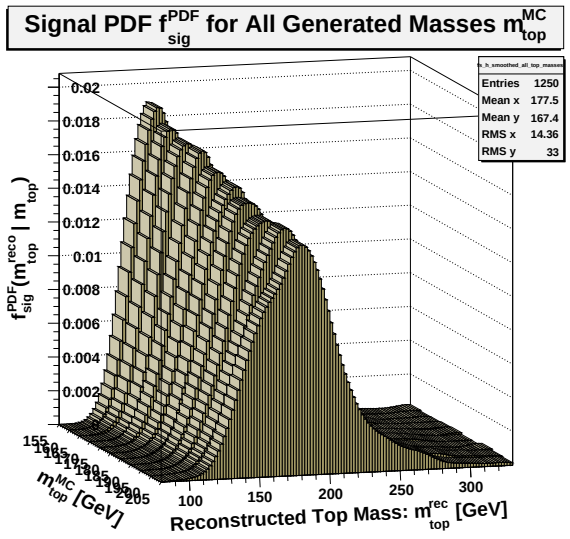

Figure 6.2.: The signal probability density distribution $f_{\mathrm{sig}}(m^{\mathrm{rec}}|m_{\mathrm{top}}^{\mathrm{MC}})$ for all generated MC masses as produced by the PDE approach for the $e\mu$ channel in `p17`. Each of the $f_{\mathrm{sig}}(m^{\mathrm{rec}}|m_{\mathrm{top}}^{\mathrm{MC}})$ is normalised to unity, their individual fluctuations are clearly visible.

thus extending the likelihood sampling region from $[155.0, 200.0]$ GeV to $[147.5, 207.5]$ GeV for `p17` and from $[120.0, 230.0]$ GeV to $[112.5, 237.5]$ GeV for `p14`. The extension of the likelihood sampling regions corresponds in its size to the width of the fit range of the cubic fit, which is performed to determine the minimum of $-\ln\mathcal{L}$. This minimises fit errors to a negligible level on the one hand and ensures that even when the maximum likelihood value $\mathcal{L}_{\max}$ is close to the boundaries of the range of generated Monte Carlo top quark masses, the cubic fit to the negative logarithmic likelihood is constrained by approximately the same number of points to the left and right side of the maximum to remove a possible systematic bias. This procedure reduces the number of failed fits to a negligible level. Refer to Fig. 7.1 for three randomly chosen $-\ln\mathcal{L}$ distributions produced with the 2-dimensional fit approach.

An alternative way to fully profit from the analytic form of the likelihood function, as described in the previous paragraph, would be to maximise the likelihood simultaneously with respect to the signal and backround yields, n_{sig} and n_{bgr}, and also with respect to the test top quark mass $m_{\mathrm{top}}^{\mathrm{MC}}$. This way, no fits are needed and the maximum likelihood value is basically determined with precision as allowed by numeric approximate calculations. This approach was not considered further in order to meet the summer 2006 conference deadlines and is therefore not included here.

6.4. The Probability Density Estimation Method as an Alternative Approach

Besides an analytic expression for the likelihood function, the more important advantage of the 2-dimensional fit method is that by simultaneous fitting of the $f_{\mathrm{sig}}(m^{\mathrm{rec}}, m_{\mathrm{top}}^{\mathrm{MC}})$ distribution to individual Monte Carlo samples with different generated top quark masses $m_{\mathrm{top}}^{\mathrm{MC}}$ all correlations

between them, like e.g. the position of the peak of the distribution, are fully accounted for. In the opposite case, that is if the signal probability density distributions are obtained for each generated Monte Carlo top quark mass $m_{\text{top}}^{\text{MC}}$ separately, they will reflect the individual character of the Monte Carlo samples for each generated top quark mass due to limited Monte Carlo statistics. In particular, this unwanted behaviour is observed with the Probability Density Estimation (PDE) smoothing approach used standard at DØ since Run I. Consequently, the difference in the $f_{\text{sig}}(m^{\text{rec}}|m_{\text{top}}^{\text{MC}})$ distributions for different $m_{\text{top}}^{\text{MC}}$ will result in fluctuations of the points of the likelihood distribution $\mathcal{L}_{\text{shape}}$. It is important to stress that these fluctuations are not of *statistical* nature, but introduce a *systematic* error to the measurement in form of the uncertainty on the fit to the likelihood distribution. Of course, this uncertainty is propagated to other distributions like the estimated top quark mass $\hat{m}_{\text{top}}$ distribution, the estimated statistical error $\hat{\sigma}_{m_{\text{top}}}$ distribution and the pull $(\hat{m}_{\text{top}} - m_{\text{top}}^{\text{MC}})/\hat{\sigma}_{m_{\text{top}}}$ distribution, to name a few.

The unwanted behaviour as described above will be demonstrated in the following on the example of the PDE approach used standard at DØ since Run I to smooth the $f_{\text{sig}}(m^{\text{rec}}|m_{\text{top}}^{\text{MC}})$ functions. This study was made using `p17` Monte Carlo pseudo-experiments in the $e\mu$ channel.

A combination of signal probability density functions for all available MC masses obtained with the PDE smoothing approach is presented in Fig. 6.2, where fluctuations for different values of $m_{\text{top}}^{\text{MC,input}}$ are clearly visible. Note that each of the distributions is normalised to unity and therefore the fluctuations are in fact fluctuations in the shape of the probability density functions.

The result of the fluctuations in the signal probability density distributions is demonstrated on the negative logarithmic likelihood distributions depicted in Fig. 6.3. There two *different* ensembles with a similar solution for the $-\ln\mathcal{L}_{\text{max}}$ point are presented. Each of the two ensembles is analysed with the PDE method (left hand side) and the 2-dimensional fit approach (right hand side). One can see that not only do the points fluctuate with the PDE method introducing uncertainties on the fits to the likelihood, moreover, these fluctuations are *not statistical*, but follow a certain pattern independent of the event ensemble, giving rise to a *systematic* error. If the parabola is taken as reference, for both ensembles the likelihood points determined with the PDE method lie for $m_{\text{top}}^{\text{MC}} = 165\,\text{GeV}$ on the parabola. For 170 GeV they both go down, after that up, up, and down again for 185 GeV. This yields a different minimum position for the PDE and 2-dimensional fit approach, but also biases the estimation of the statistical error. Historically, the observation of this behaviour was the main reason to study and introduce the 2-dimensional fit approach.

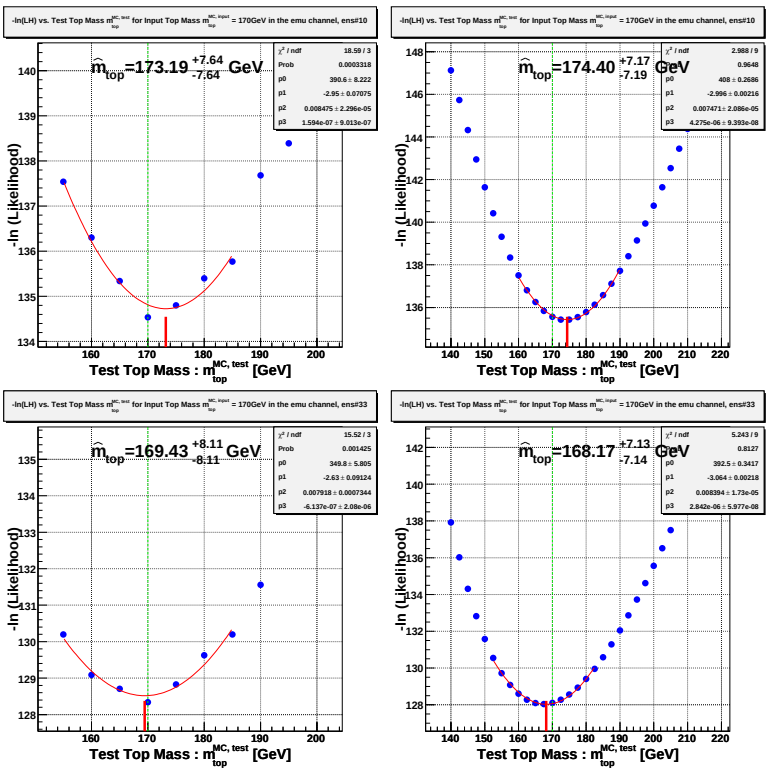

Figure 6.3.: Distributions of the negative logarithmic likelihood $-\ln\mathcal{L}$ as obtained using the PDE (left column) and the 2-dimensional fit approach (right column) for Monte Carlo events. In each row, the same pseudo-experiments designed with the same ensembles of events are shown. The ensembles on the top and bottom have their minimum for approximately the same m_{top} value. The fluctuations of their points follow the *same pattern* for the PDE method, which results in a systematic error on the fit. Details on Ensemble Testing with pseudo-experiments can be found in Chap. 7.

		Signal				Backgr.	
		$\widetilde{\alpha}_i^{j=0}$	$\Delta\widetilde{\alpha}_i^{j=0}$	$\widetilde{\alpha}_i^{j=1}$	$\Delta\widetilde{\alpha}_i^{j=1}$	α_i	$\Delta\alpha_i$
p17, $e\mu$	$i=0$	71.4	0.8	0.163	0.004	94.5	3.4
	$i=1$	-3.83	0.13	0.0415	0.0007	3.82	0.95
	$i=2$	0.0416	0.0024	6.18e-05	1.17e-05	0.0597	0.0093
	$i=3$	53.3	7.1	0.594	0.040	137	3.0
	$i=4$	-14.8	5.5	0.194	0.030	12.0	1.7
	$i=5$	1.07	0.21	-0.00377	0.00114	0.698	0.113
p14, $e\mu$	$i=0$	72.1	1.2	0.176	0.008	94.5	1.3
	$i=1$	-3.46	0.45	0.0567	0.0058	3.55	0.37
	$i=2$	0.0855	0.019	-2.97e-05	8.1e-05	0.0589	0.0059
	$i=3$	38.5	4.2	0.71	0.03	-	-
	$i=4$	-20.3	2.9	0.225	0.016	-	-
	$i=5$	0.93	0.20	-0.00369	0.00113	1	fixed
p14, ee	$i=0$	102	14	0.0094	0.076	85.9	20.1
	$i=1$	-0.185	1.8	0.015	0.01	4.5	2.8
	$i=2$	0.068	0.023	-0.00012	0.00012	0.058	0.018
	$i=3$	19.6	7.6	0.842	0.044	-	-
	$i=4$	-4.4	6.9	0.126	0.042	-	-
	$i=5$	0.47	0.38	-0.000384	0.0022	1	fixed
p14, $\mu\mu$	$i=0$	85.5	7.7	0.116	0.038	80	33
	$i=1$	4.54	5.23	-0.012	0.031	5.6	4.4
	$i=2$	0.147	0.063	-0.00064	0.00034	0.065	0.023
	$i=3$	26.0	8.0	0.799	0.044	-	-
	$i=4$	-17.6	6.0	0.22	0.03	-	-
	$i=5$	0.89	0.51	-0.0038	0.0026	1	fixed

Table 6.1.:
The $\widetilde{\alpha}_i^j$ fit parameters for the signal probability density function $f_{\mathrm{sig}}(m_{\mathrm{top}}^{\mathrm{rec}}, m_{\mathrm{top}}^{\mathrm{MC}})$ and the α_i fit parameters for the corresponding background probability density function $f_{\mathrm{bgr}}(m_{\mathrm{top}}^{\mathrm{rec}})$ for the $e\mu$ channel, version p17 of DØ software and all three dileptonic channels for p14.

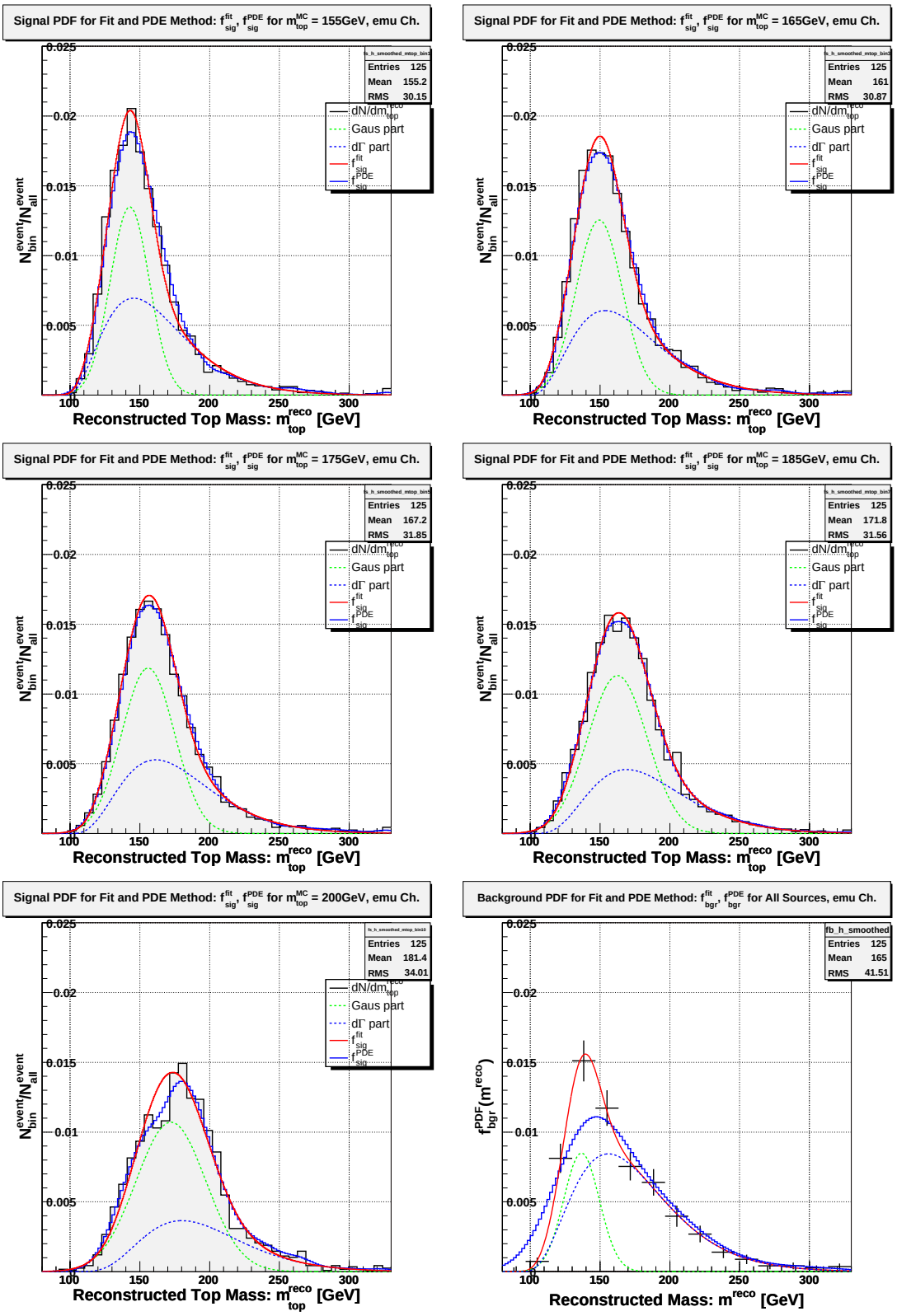

Figure 6.4.: The signal probability density function $f_{\mathrm{sig}}(m^{\mathrm{rec}}|m_{\mathrm{top}}^{\mathrm{MC}})$ (smooth solid red line) for $m_{\mathrm{top}}^{\mathrm{MC}} = 155,\ 165,\ 175,\ 185,\ 200\,\mathrm{GeV}$ and the background density function $f_{\mathrm{bgr}}(m^{\mathrm{rec}})$ (bottom right plot) for the $e\mu$ channel and version `p17` of DØ software. The results of the PDE approach are shown as a blue fine-binned histogram line.

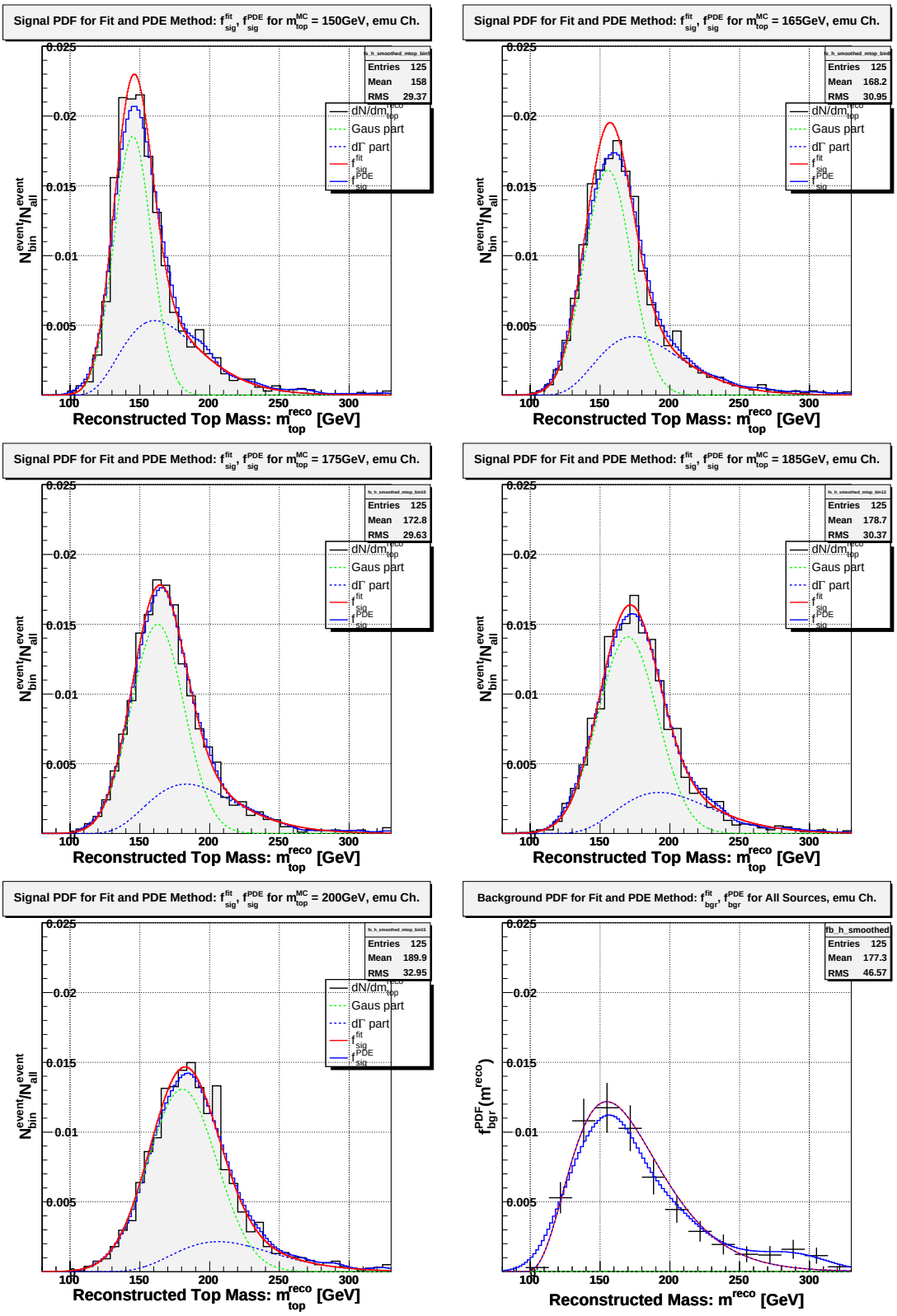

Figure 6.5.: The signal probability density function $f_{\mathrm{sig}}(m^{\mathrm{rec}}|m_{\mathrm{top}}^{\mathrm{MC}})$ (smooth solid red line) for $m_{\mathrm{top}}^{\mathrm{MC}} = 150,\ 165,\ 175,\ 185,\ 200\,\mathrm{GeV}$ and the background density function $f_{\mathrm{bgr}}(m^{\mathrm{rec}})$ (bottom right plot) for the $e\mu$ channel and version `p14` of DØ software. The results of the PDE approach are shown as a blue fine-binned histogram line.

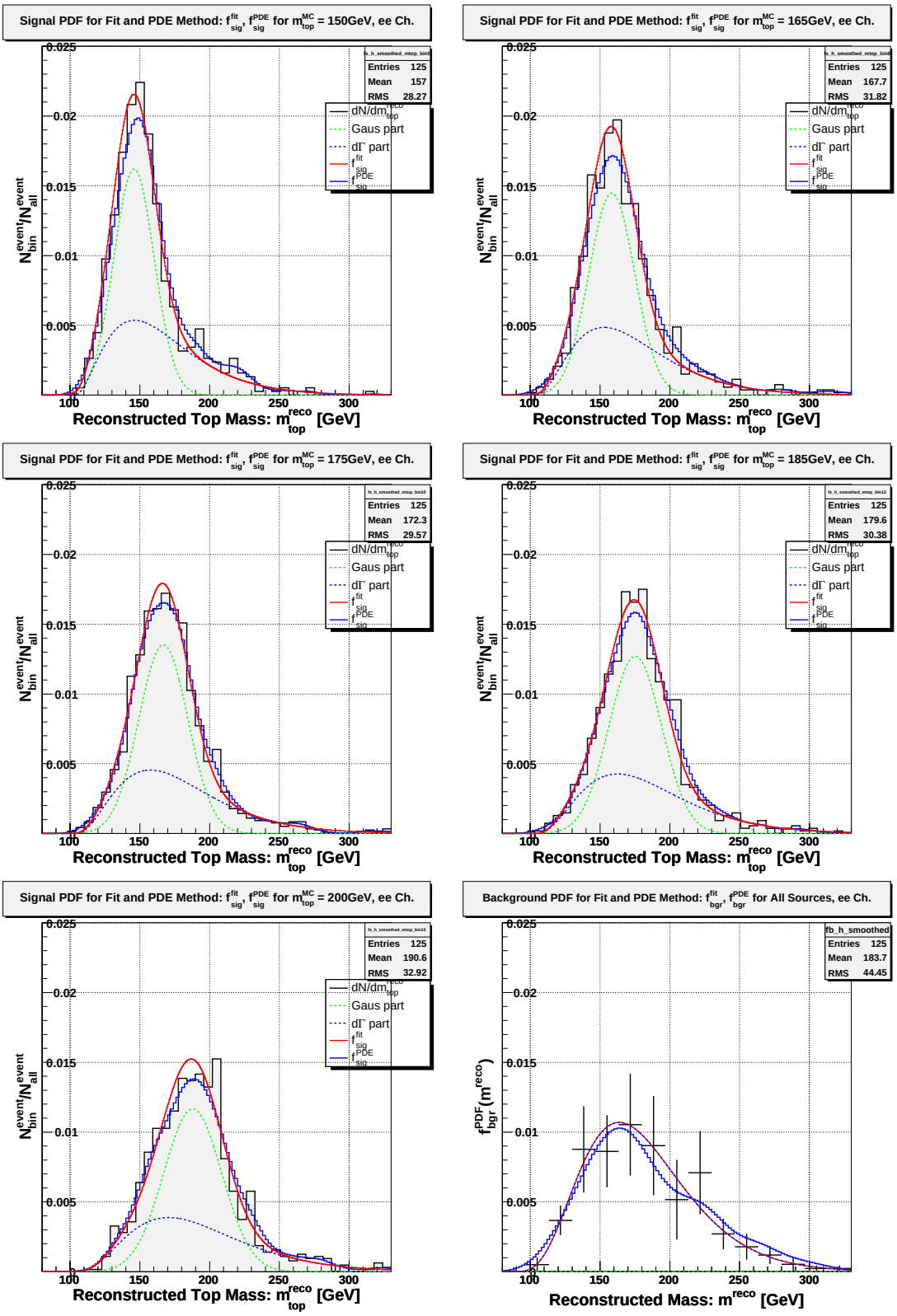

Figure 6.6.: The signal probability density function $f_{\mathrm{sig}}(m^{\mathrm{rec}}|m_{\mathrm{top}}^{\mathrm{MC}})$ (smooth solid red line) for $m_{\mathrm{top}}^{\mathrm{MC}} = 150,\ 165,\ 175,\ 185,\ 200\,\mathrm{GeV}$ and the background density function $f_{\mathrm{bgr}}(m^{\mathrm{rec}})$ (bottom right plot) for the *ee* channel and version `p14` of DØ software. The results of the PDE approach are shown as a blue fine-binned histogram line.

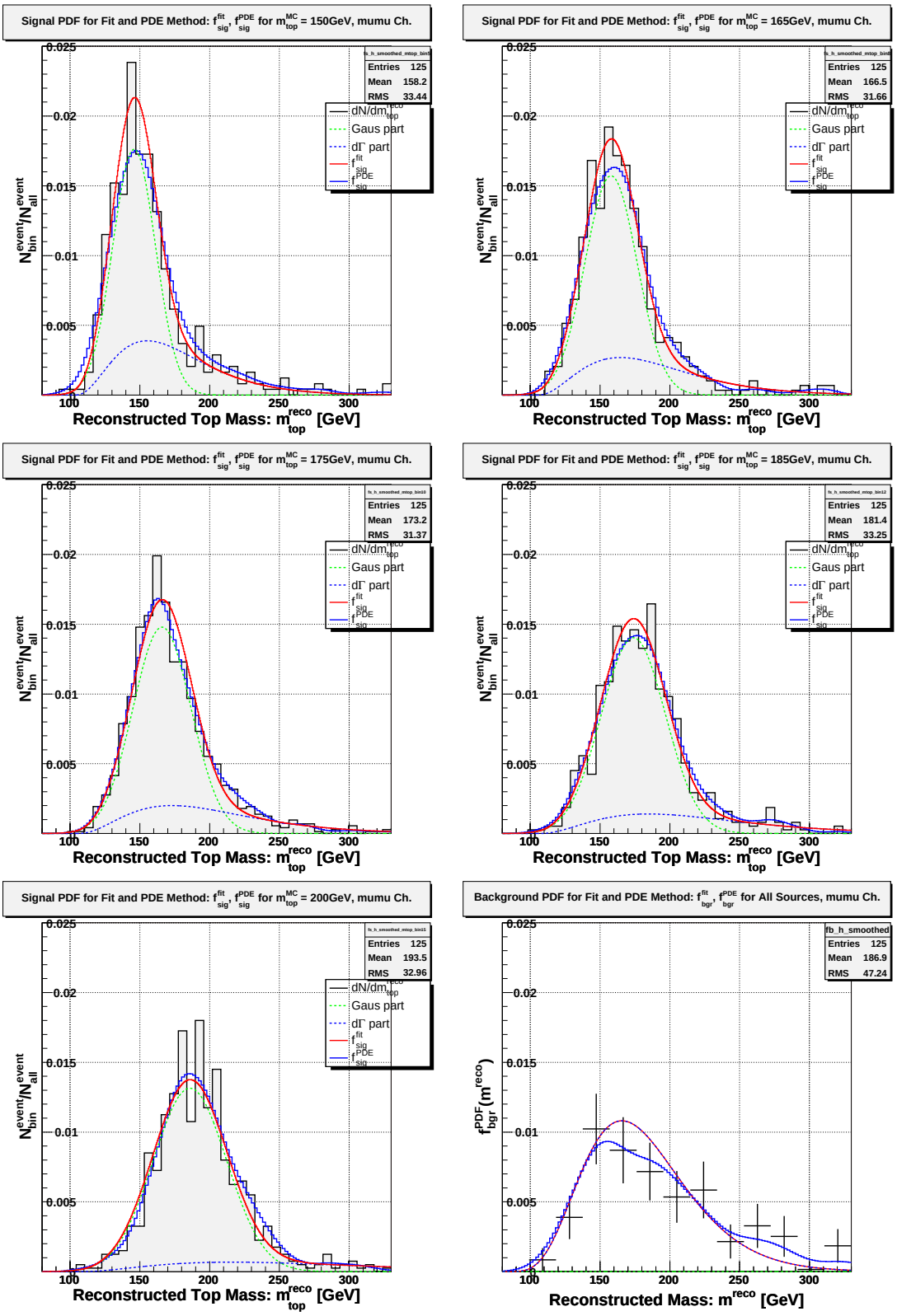

Figure 6.7.: The signal probability density function $f_{\mathrm{sig}}(m^{\mathrm{rec}}|m_{\mathrm{top}}^{\mathrm{MC}})$ (smooth solid red line) for $m_{\mathrm{top}}^{\mathrm{MC}} = 150,\ 165,\ 175,\ 185,\ 200\,\mathrm{GeV}$ and the background density function $f_{\mathrm{bgr}}(m^{\mathrm{rec}})$ (bottom right plot) for the $\mu\mu$ channel and version `p14` of DØ software. The results of the PDE approach are shown as a blue fine-binned histogram line.

7. Testing the Maximum Method with Pseudo-Experiments

With the likelihood function defined in Chap. 6, the developed mass extraction machinery is ready to be applied to the selected dataset. However, before proceeding with this step, the performance of the Neutrino Weighting Method combined with the Maximum Method must be evaluated. It has to be verified that the developed top quark mass estimator is unbiased and that the statistical error is estimated correctly as well (see [99] for the definition of a "good" estimator).

7.1. The Ensemble Testing Technique

A common tool of Particle Physics to validate an estimator is the so-called Ensemble Testing technique. In this approach, pseudo-experiments are designed from Monte Carlo events with a known top quark mass $m_{\mathrm{top}}^{\mathrm{MC}}$ and analysed in exactly the same way as the selected dataset. Ideally, the top quark mass estimate $\hat{m}_{\mathrm{top}}$ measured over many pseudo-experiments should on average be the same as the input top mass. In this analysis, 500 pseudo-experiments are used. A crucial point is to design the event ensembles for the individual pseudo-experiment in such a way that they reflect the situation in the data with respect to the expected signal and background yield.

The exact procedure for channel-wise pseudo-experiment generation is as follows: the size N of the event ensemble to make up a pseudo experiment is the same number of events as selected in data, i.e. $N = 23$ in `p14` and $N = 28$ in `p17`. The contribution from each signal/background source is subject to Poisson fluctuations. To reflect this, for each of its 28 event "slots" one subsequently decides, if it is filled from the signal Monte Carlo event pool or one of the background pools. The relative contribution of each background process i is calculated as

$$C_i := \frac{\hat{Y}_{\mathrm{bgr}_i}}{N}, \qquad C_0 \equiv 0\,,$$

with $\hat{Y}_{\mathrm{bgr}_i}$ and N given in Tab. 4.5, 4.6, 4.7, and 4.8. A random number x uniformly distributed in the interval [0,1] is drawn. If

$$x \in \left[\sum_{j=0}^{i-1} C_j, \sum_{j=0}^{i} C_j\right[\tag{7.1}$$

is true, an event is randomly chosen from the Monte Carlo pool for background i. If the condition of Eqn. 7.1 is not fulfilled for any of the background sources, an event is drawn from the signal sample for the tested input mass $m_{\mathrm{top}}^{\mathrm{MC}}$.

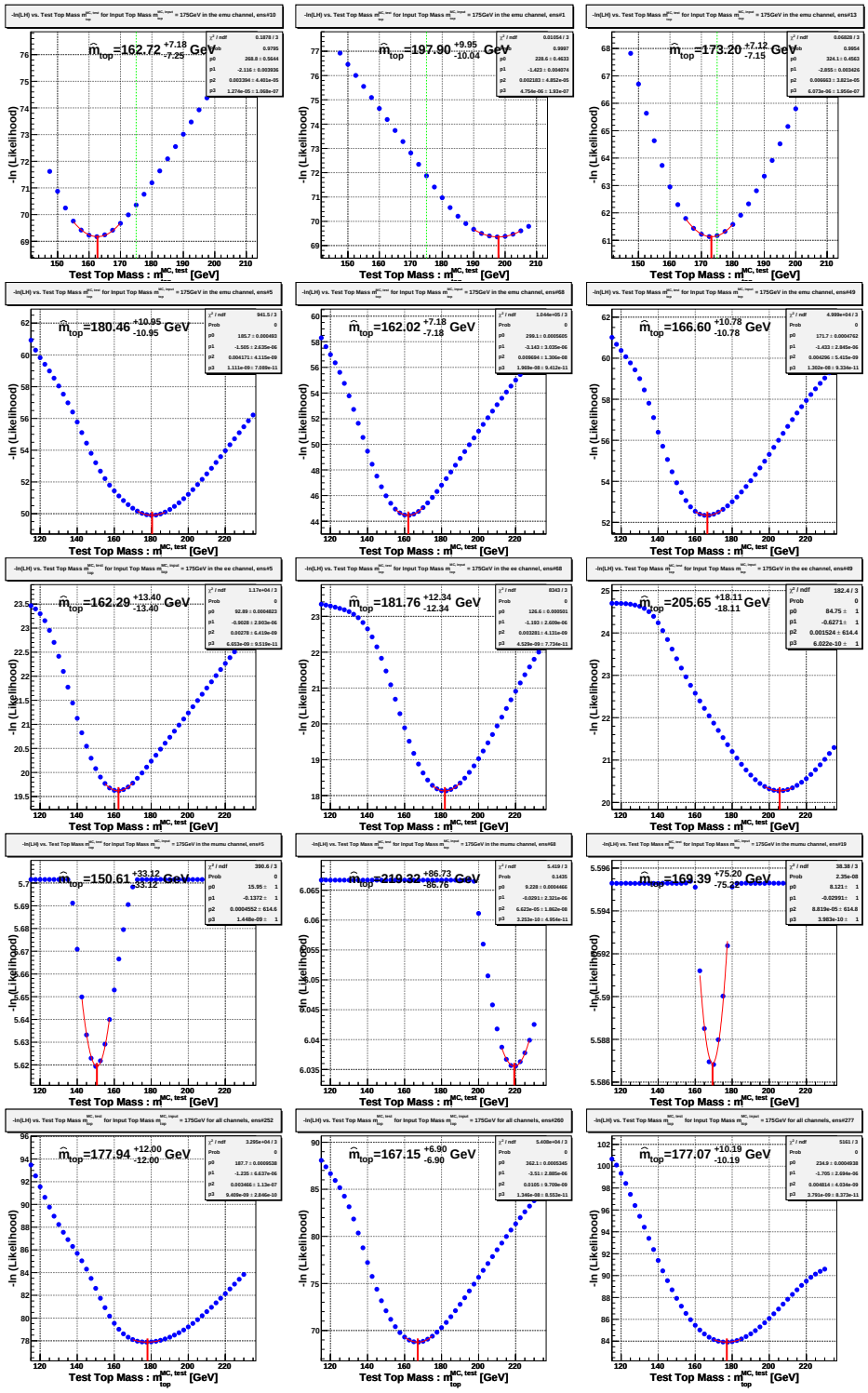

Figure 7.1.: Sample distributions of the negative logarithmic likelihood $-\ln\mathcal{L}$ for three randomly chosen ensembles for a generated top quark mass of $m_{\text{top}}^{\text{MC}} = 175\,\text{GeV}$ are shown in rows for the $e\mu$ channel and p17, the $e\mu$, ee, $\mu\mu$ channel and their combination in p14, going from top to bottom.

This algorithm inspired by [82, 102, 99] guarantees a Poisson distribution of drawn events for each of the considered physical processes on the one hand, on the other hand it does not depend on the yield of the top quark and thus not on its cross section. This is important because the cross section of the top quark is predicted to depend on its mass by the Standard Model and thus would require variable contributions $C_i = C_i(m_{\text{top}}^{\text{MC}})$ as well as further theoretical assumptions from the Standard Model, as detailed in Chap. 2 and Fig. 2.2.

The algorithm as described above is slightly changed for the $\mu\mu$ channel in `p14`. The yield in data after the reconstruction with the Neutrino Weighting Method is 1 event, whereas the sum of the expected yields for the backgrounds is 1.43. A blind application of the algorithm as described above would produce event ensembles comprised of background events only. Therefore, the scaling factors C_i are calculated as:

$$C_i := \frac{\hat{Y}_{\text{bgr}_i}}{\sum_j \hat{Y}_{\text{bgr}_j} + \hat{Y}_{\text{sig}}}, \qquad C_0 \equiv 0\,.$$

For the $370\,\text{pb}^{-1}$ dataset reconstructed in `p14` all three dileptonic channels are available. Here, a pseudo-experiment for all three channels is designed by simply taking three ensembles for the individual channels. The individual per-channel likelihood functions are calculated and added for each of the evaluation points in m_{top}. The final minimisation of the resulting 3-channel likelihood with respect to the top quark mass $m_{\text{top}}^{\text{MC}}$ is done in the same way as the minimisation for the per-channel likelihood.

In Fig. 7.1 random samples of the negative logarithmic likelihood for 3 pseudo-experiments are shown for the $e\mu$ channel and version `p17` of DØ software, as well as for the $e\mu$, ee, $\mu\mu$ channels, and their combination in `p14`. The event ensembles are designed using a generated top quark mass $m_{\text{top}}^{\text{MC,input}} = 175\,\text{GeV}$.

For small ensemble sizes, the increase of the statistical error is clearly visible. In these pseudo-experiments a kink-off behaviour of the negative logarithmic likelihood function far away from the minimum is observed, where it becomes almost flat. This happens when the signal and background probability density functions are sampled in very few points $m_{\text{top}}^{\text{rec}}$ lying close together and the fitted signal yield becomes much smaller than the background: $n_{\text{sig}} \ll n_{\text{bgr}}$. This preference of the signal/background fit can be explained in the following way: the background density function is much wider and has higher values in its flanks than a typical signal density function for a generated top quark mass $m_{\text{top}}^{\text{MC,input}}$. Therefore, when mass hypotheses $m_{\text{top}}^{\text{MC}}$ far away from the $m_{\text{top}}^{\text{rec}}$ are tested, the area under the background density function is higher than for the signal and naturally a high background contribution is preferred: $n_{\text{sig}} \to 0$, $n_{\text{bgr}} \to N$.

7.2. Testing the Top Quark Mass Estimator

For each of the pseudo-experiments designed using the algorithm introduced above the negative logarithmic likelihood $-\ln\mathcal{L}$ is minimised with respect to the top quark mass $m_{\text{top}}^{\text{MC}}$ as described in Chap. 6 to obtain estimates for the top quark mass $\hat{m}_{\text{top}}$ and its statistical error, $\hat{\sigma}_{m_{\text{top}}}$.

For an unbiased top quark mass estimator the average of the top quark masses measured in 500 pseudo-experiments, $\langle \hat{m_{\text{top}}} \rangle$, should trace the input top quark mass $m_{\text{top}}^{\text{MC,input}}$. This test is

D0Reco ver.	channel	α	$\Delta\alpha$	β [GeV]	$\Delta\beta$ [GeV]
p17	$e\mu$	0.99	0.01	0.18	0.15
p14	$e\mu$	0.99	0.01	0.86	0.14
p14	ee	0.86	0.01	0.86	0.30
p14	$\mu\mu$	0.39	0.02	-7.26	0.33
p14	all	0.98	0.01	0.09	0.11

Table 7.1.: The results of a linear fit as defined in Eqn. 7.2 to the ensemble test plots for the $\hat{m}_{\text{top}}$ estimator presented in Fig. 7.2. Preferable are α values close to unity and β close to 0.

repeated for every generated mass point. The results for

$$\begin{aligned} m'^{\text{MC,input}}_{\text{top}} &:= m^{\text{MC,input}}_{\text{top}} - 175\,\text{GeV}, \text{ and} \\ \hat{m}'_{\text{top}} &:= \hat{m}_{\text{top}} - 175\,\text{GeV} \end{aligned}$$

are shown in Fig. 7.2. Since every point in this plot is subject to statistical fluctuations, they are fitted with a linear ansatz:

$$\langle \hat{m}'_{\text{top}} \rangle = \alpha \cdot m'^{\text{MC,input}}_{\text{top}} + \beta\,. \tag{7.2}$$

In the ideal case, the slope should be close to unity: $\alpha \stackrel{!}{=} 1$, and the offset close to 0: $\beta \stackrel{!}{=} 0\,\text{GeV}$. The fit results are summarised in Tab. 7.1.

For the ee and the $\mu\mu$ channel in p14 the slope is far away from the ideal value: 0.86 for ee and 0.39 for $\mu\mu$. The reason for this behaviour is the small ensemble size of 5 or even only 1 event in these channels. For a small ensemble a large statistical error and Gaussian fluctuations of the measured top quark mass of the same magnitude are expected. With generated top quark masses $m^{\text{MC,input}}_{\text{top}}$ close to the boundary of the range of available Monte Carlo, for a significant fraction of ensembles only one flank of the $-\ln\mathcal{L}$ parabola is inside of the range. In such cases the fit algorithm tends to fit a flat polynomial or even a straight line through the points. Since, as discussed, this effect occurs for $\hat{m}_{\text{top}}$ on the outbound side of the top quark mass range only, $\langle \hat{m}_{\text{top}} \rangle$ is biased to the inbound side, resulting in smaller slope values α. One can tackle this problem by introducing additional points for evaluation of the likelihood, as discussed in Chap. 6. However, this is possible only to a limited extent, as for too small or too high generated top quark masses the Eqn. 6.4 loses its validity. One might assume that this problem is caused by a higher background fraction in the ee and $\mu\mu$ channel, but the calibration curve for pure signal in the ee channel in Fig. 7.2 (f) proves this wrong.

Since the linear curve defined by Eqn. 7.2 relates the average output top mass $\langle \hat{m}_{\text{top}} \rangle$ to the input top mass $m^{\text{MC,input}}_{\text{top}}$, it can be used to calibrate the measurement. The situation in data is the following: one wants to map the output top mass to the "input" top mass as found in Nature. Therefore, for the calibration of the measured top quark mass $\hat{m}_{\text{top}}$ Eqn. 7.2 is inverted:

$$\hat{m}^{\text{corr}}_{\text{top}} = (\hat{m}_{\text{top}} - 175\,\text{GeV}) \cdot \frac{1}{\alpha} - \frac{\beta}{\alpha} + 175\,\text{GeV}\,. \tag{7.3}$$

All figures to be shown in this Chapter will have this correction applied. Due to the problematic situation with small ensemble sizes, for the $370\,\text{pb}^{-1}$ dataset reconstructed with version p14 of DØ software all three channels combined will be considered, rather than individually.

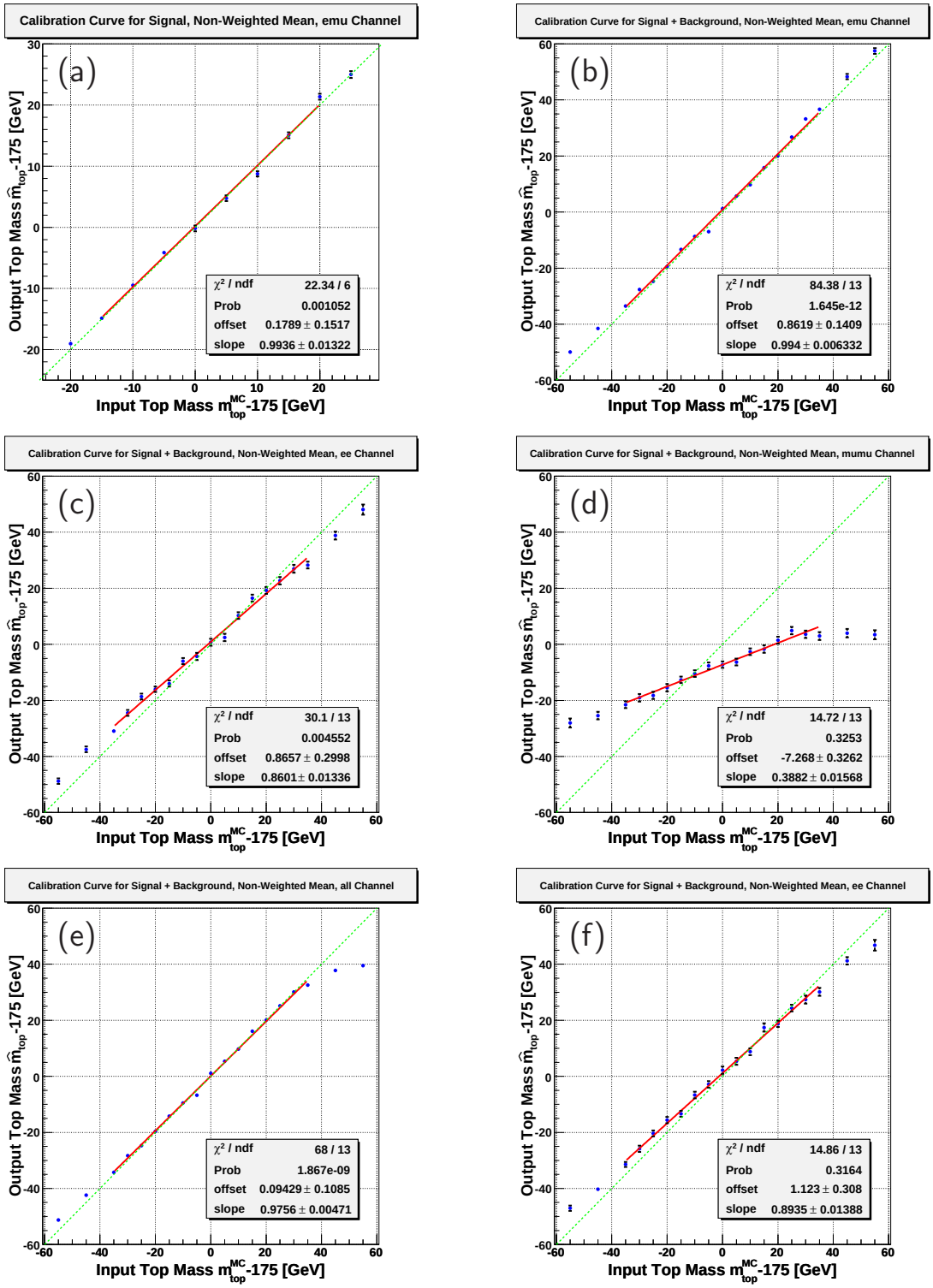

Figure 7.2.: The results of ensemble tests of the top quark mass estimator $\hat{m}_{\mathrm{top}}$: average top quark mass estimate $\langle \hat{m}_{\mathrm{top}} \rangle - 175\,\mathrm{GeV}$ vs. generated MC input top quark mass $m_{\mathrm{top}}^{\mathrm{MC,input}} - 175\,\mathrm{GeV}$. As a red solid line the linear fit as defined in Eqn. 7.2 is shown. The dashed line shows the ideal situation with a slope of unity and an offset of 0. In `p17`, the fits are made to Monte Carlo masses in the interval $[160, 195\,\mathrm{GeV}]$, and to the $[140, 210\,\mathrm{GeV}]$ mass range for `p14`. In (a) the $e\mu$ channel and `p17` is shown. In (b), (c), and (d) `p14` and the $e\mu$, ee, $\mu\mu$ channel are presented. The combination of all channels for `p14` is visualised in (e). The results for pure signal Monte Carlo in the ee channel of `p14` are depicted in (f).

D0Reco ver.	$\langle M_P \rangle$	$\Delta\langle M_P \rangle$	$\langle W_P \rangle$	$\Delta\langle W_P \rangle$	$\langle \hat{\sigma}_{m_{\text{top}}} \rangle$ [GeV]	RMS(Δm_{top}) [GeV]
p14	0.05	0.1	0.94	0.01	9.4	9.9
p17	0.04	0.1	0.99	0.01	8.0	8.2

Table 7.2.: Average pull mean $\langle M_P \rangle$ and pull width $\langle W_P \rangle$ values, the mean statistical error and the Root Mean Square of $\Delta m_{\text{top}} := \hat{m}_{\text{top}}^{\text{corr}} - m_{\text{top}}^{\text{MC,input}}$ are shown for both datasets. Where applicable, a Monte Carlo top quark mass closest to the value measured in data is chosen.

7.3. Testing the Estimator for the Statistical Error on the Top Quark Mass

To evaluate the validity of the estimator for the statistical error on the top quark mass $\hat{\sigma}_{m_{\text{top}}}$ as defined at the end of Chap. 6, the properties of pull distributions are analysed. The figures for the statistical error are already corrected using Eqn. 7.3.

The pull P is defined as:

$$P := \frac{\hat{m}_{\text{top}}^{\text{corr}} - m_{\text{top}}^{\text{MC,input}}}{\hat{\sigma}_{m_{\text{top}}}}, \tag{7.4}$$

where $\hat{m}_{\text{top}}^{\text{corr}}$ is the estimated top quark mass with the correction of Eqn. 7.3 applied. For a well-estimated error the pull distribution should have a Gaussian shape centred around 0 and a σ-parameter of approximately 1. For each of the Monte Carlo mass points Gaussians are fitted to the pull distribution. Their mean parameter together with the σ-parameter are analysed. These parameters will be referred to as "pull mean" M_P and "pull width" W_P in the following.

The pull distribution for a Monte Carlo top mass $m_{\text{top}}^{\text{MC,input}}$ closest to the value measured in data for the $e\mu$ channel of the $835\,\text{pb}^{-1}$ dataset reconstructed in p17 and for the combination of all dileptonic channels of the $370\,\text{pb}^{-1}$ dataset reconstructed in p14 are depicted in Fig. 7.3 (a) and (b), respectively. The pull mean for all generated top quark masses of the Monte Carlo sets is presented in (c) and (d) in the same order, the pull width in (e) and (f). The average pull mean $\langle M_P \rangle$ and pull width $\langle W_P \rangle$ are summarised in Tab. 7.3.

The average pull width for the $e\mu$ channel and p17 is consistent with unity, the statistical error is estimated correctly. For all dileptonic channels combined in p14 the pull width is 0.94, which means that the statistical error is overestimated by 6%. It is a common practice to correct the statistical error besides Eqn. 7.3 with the pull width: $\hat{\sigma}_{m_{\text{top}}}^{\text{corr}} = \langle W_P \rangle \cdot \hat{\sigma}_{m_{\text{top}}}$. However, here one would scale down the statistical error and pretend a precision which is not there. Thus the correction for the statistical error with the pull width is considered problematic and is omitted.

The average pull mean is slightly below 0 for the $e\mu$ channel in p17 and all channels in p14. This is explained by the fact that for the same generated Monte Carlo top quark mass m_{top}^{MC} the steepness of the likelihood parabola decreases for pseudo-experiments with higher $\hat{m}_{\text{top}}$ values, as expected for a decreasing sensitivity for higher masses due to broader $f_{\text{sig}}(m_{\text{top}}^{\text{rec}}|m_{\text{top}}^{MC})$ functions. This gives a small distortion due to the statistical error estimate $\hat{\sigma}_{m_{\text{top}}}$ in the denominator of the pull definition Eqn. 7.4.

For both datasets and D0Reco versions, the distribution of statistical errors and measured top

quark masses for a Monte Carlo top mass closest to the measured value, as well as the mean statistical errors for all masses available are presented in Fig. 7.4 and summarised in Tab. 7.3.

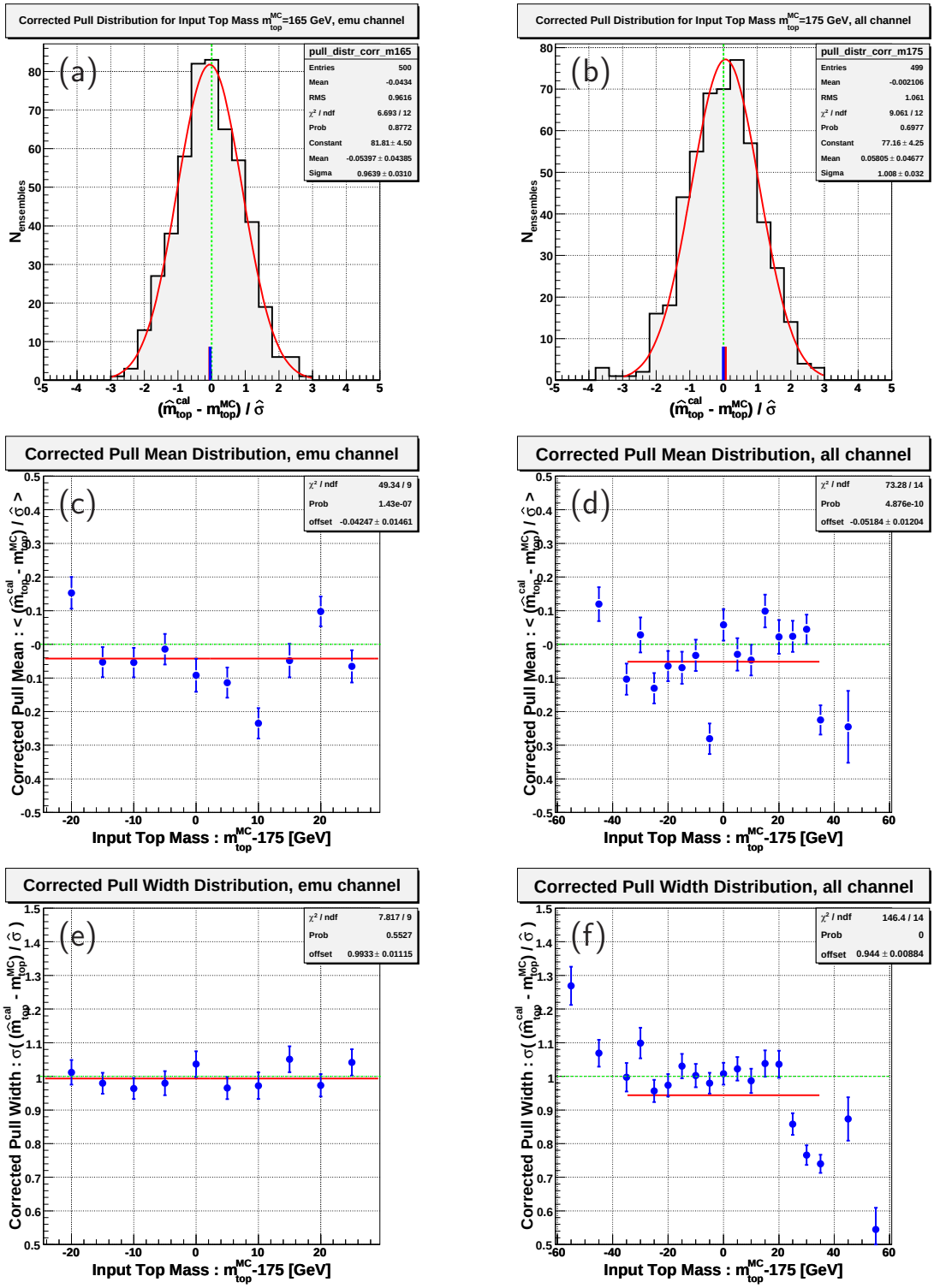

Figure 7.3.: In (a) the pull distribution for $m_{\text{top}}^{\text{MC,input}}$=165 GeV for the $e\mu$ channel and `p17` is shown, in (b) for $m_{\text{top}}^{\text{MC,input}}$=180 GeV for the combination of all dileptonic channels in `p14`. Both Monte Carlo mass points are closest to the top quark mass measured in data for the corresponding datasets. The red smooth curve is a Gaussian fit, the solid blue vertical line visualises its mean parameter. (c) and (d) depict the pull means for all available Monte Carlo top quark masses for the same datasets, (e) and (f) the pull width. The red solid lines in (c)-(f) are the mean values over all top quark masses in `p17` and in the range between 140 and 210 GeV for `p14`.
All plots are shown after calibration with Eqn. 7.3.

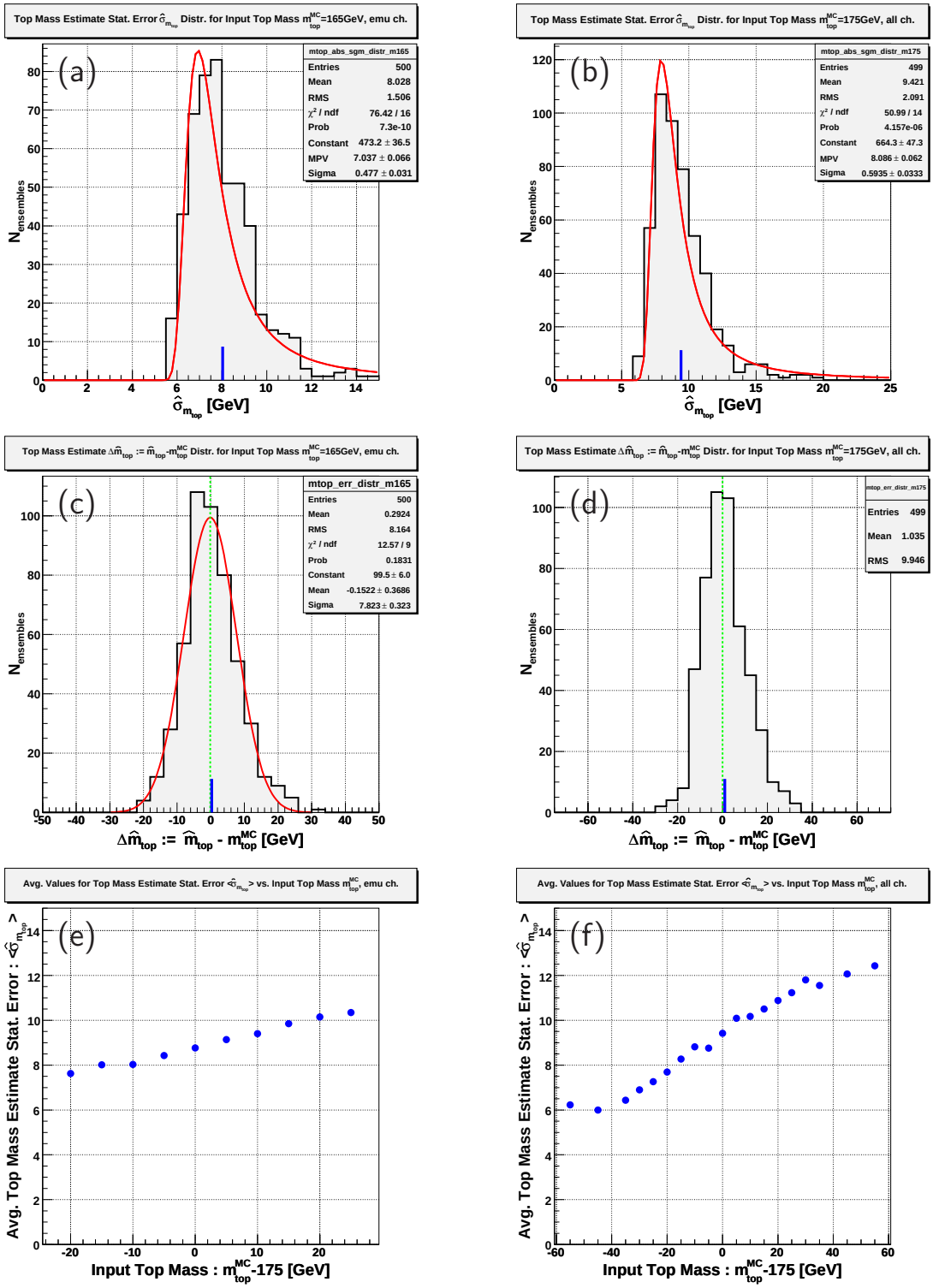

Figure 7.4.: The distribution of statistical errors is shown in (a) and (b) for the $e\mu$ channel in `p17` and the combination of all dileptonic channels in `p14`, respectively. The red smooth solid curve is a fit with a Landau function, since it is expected to describe the shape of the errors for a sampling procedure, the small blue vertical line visualises the mean of the statistical error. In (c) and (d) the difference between the mean estimated top mass and the input top mass is shown for the same Monte Carlo sets, together with a Gaussian fit and its mean parameter. The mean statistical errors for all generated mass points $m_{\text{top}}^{\text{MC,input}}$ are shown in (e) for `p17` and in (f) for `p14`.
All plots are shown after calibration with Eqn. 7.3.

8. Results

In this chapter the Neutrino Weighting Method combined with the Maximum Method will be applied to data. As detailed in Chap. 4, all three dileptonic channels of the $370\,\mathrm{pb}^{-1}$ dataset reconstructed with version `p14` of DØ software as well as the $e\mu$ channel of the $835\,\mathrm{pb}^{-1}$ dataset and `p17` are analysed. All but one $\mu\mu$ event in the $370\,\mathrm{pb}^{-1}$ data sample (run 189768, event 2578249) have solutions with the Neutrino Weighting Method. Cross checks of the result will be presented.

Data and Monte Carlo events are analysed in exactly the same way, with one exception: due to limitations in computation time, Monte Carlo events cannot be smeared 2000 times, as done for data and found to be sufficient to stabilise the mass weight distribution and its most probable value. However, for Monte Carlo events 150 smears yield reliable results for the means of ensemble testing.

8.1. Results for the $370\,\mathrm{pb}^{-1}$ Dataset

The negative logarithmic likelihood distributions, as they result for the events selected in the $370\,\mathrm{pb}^{-1}$ dataset reconstructed using version `p14` of the DØ software, are displayed channel-wise in Fig. 8.1 (a) to (c). The measured top quark masses and their statistical errors before calibration are shown in the third and fourth column of Tab. 8.1. As expected, the statistical error is smallest for the $e\mu$ channel, with the largest statistics of 17 events.

It is important to note that the results in the $e\mu$ and ee channels are several sigmas away from each other. This makes the combination of the per-channel likelihood functions problematic, as can be seen in Fig. 8.1 (d). The total likelihood has a pot-like shape and the minimum is of small significance. Therefore, for the statistical error not the result from the extrapolation of the fit to the minimum region of negative logarithmic distribution is quoted, instead the statistical uncertainty is determined from the top quark mass values for which the likelihood is half a unit above its minimum. This yields $^{+17.1}_{-28.6}\,\mathrm{GeV}$ for the statistical error. The combined result for the $370\,\mathrm{pb}^{-1}$ dataset is calibrated with Eqn. 7.3 and the fit parameters found in ensemble tests, as summarised in Tab. 7.1. Where applicable, the calibrated $\hat{m_{\mathrm{top}}}^{\mathrm{corr}}$ values are presented in the last two rows of Tab. 8.1.

As the final result and its statistical uncertainty for the $370\,\mathrm{pb}^{-1}$ dataset reconstructed with `D0Reco p14` is quoted:

$$m_{\mathrm{top}}^{370\,\mathrm{pb}^{-1}} = 176.8\ ^{+17.5}_{-29.3}\,\mathrm{GeV}\,.$$

Dataset		$\hat{m}_{\text{top}}$ [GeV]	$\hat{\sigma}_{m_{\text{top}}}$ [GeV]	$\hat{m}_{\text{top}}^{\text{corr}}$ [GeV]	$\hat{\sigma}_{m_{\text{top}}}^{\text{corr}}$ [GeV]
370 pb^{-1}, p14	$e\mu$	146.4	10.3	-	-
370 pb^{-1}, p14	ee	206.2	18.4	-	-
370 pb^{-1}, p14	$\mu\mu$	171.8	84.9	-	-
370 pb^{-1}, p14	all	176.8	$^{+17.1}_{-28.6}$	176.8	$^{+17.5}_{-29.3}$
370 pb^{-1}, p17	$e\mu$	159.2	15.3	-	-
465 pb^{-1}, p17	$e\mu$	169.1	12.4	-	-
835 pb^{-1}, p17	$e\mu$	165.7	9.9	165.5	10.0

Table 8.1.: Data measurements of the top quark mass $\hat{m}_{\text{top}}$ and its statistical uncertainty $\hat{\sigma}_{m_{\text{top}}}$ before and after correction. For details on the datasets refer to Chap. 4, the corrections applied are as discussed in Chap. 7. For the 835 pb^{-1} dataset reconstructed with p17 the results for the 370 pb^{-1} and 465 pb^{-1} subsets are shown separately for comparison.

8.2. Results for the 835 pb^{-1} Dataset

For the 835 pb^{-1} dataset reconstructed with version p17 of the DØ software, the result of the fit to the negative logarithmic likelihood is presented in Fig. 8.1 (e) and summarised in Tab. 8.1. Part (f) of the figure presents the distribution of reconstructed masses $m_{\text{top}}^{\text{rec}}$ together with the signal and background probability density function scaled by their fitted yields: $n_{\text{sig}} = 22.9 \pm 8.0$, $n_{\text{bgr}} = 4.5 \pm 2.8$, as found for $m_{\text{top}}^{\text{rec}}$=165 GeV, being closest to the measured top quark mass value. For the 835 pb^{-1} dataset after calibration is found:

$$m_{\text{top}}^{835\,\text{pb}^{-1}} = 165.5 \pm 10.0\,\text{GeV}\,.$$

8.3. Result Cross-Checks

Several cross checks have been made to validate and understand the results in data. They will be presented in the following.

As detailed in Chap. 4, the full dataset of 835 pb^{-1} consists of two parts: the 370 pb^{-1} dataset collected until August 2004 and the remaining 465 pb^{-1}. With DOReco version p17, 15 events are selected in the 370 pb^{-1} dataset, and 13 events in 465 pb^{-1}. Seven events in the 370 pb^{-1} dataset are selected with both, p14 and p17.

To cross check the validity of the data result for the full 835 pb^{-1} of data the two subsets were analysed separately in the same way, with one exception – the yield of all background processes was scaled to the respective integrated luminosity of the data subsets. The resulting likelihood distributions are presented in Fig. 8.2. For these partial datasets, the values $m_{\text{top}}^{370} = 159.2 \pm 15.3$ and $m_{\text{top}}^{465} = 169.1 \pm 12.4$ have been measured before calibration. This is in good agreement with the non-calibrated value for the full dataset.

Furthermore, assuming that the errors are Gaussian distributed the two measurements were

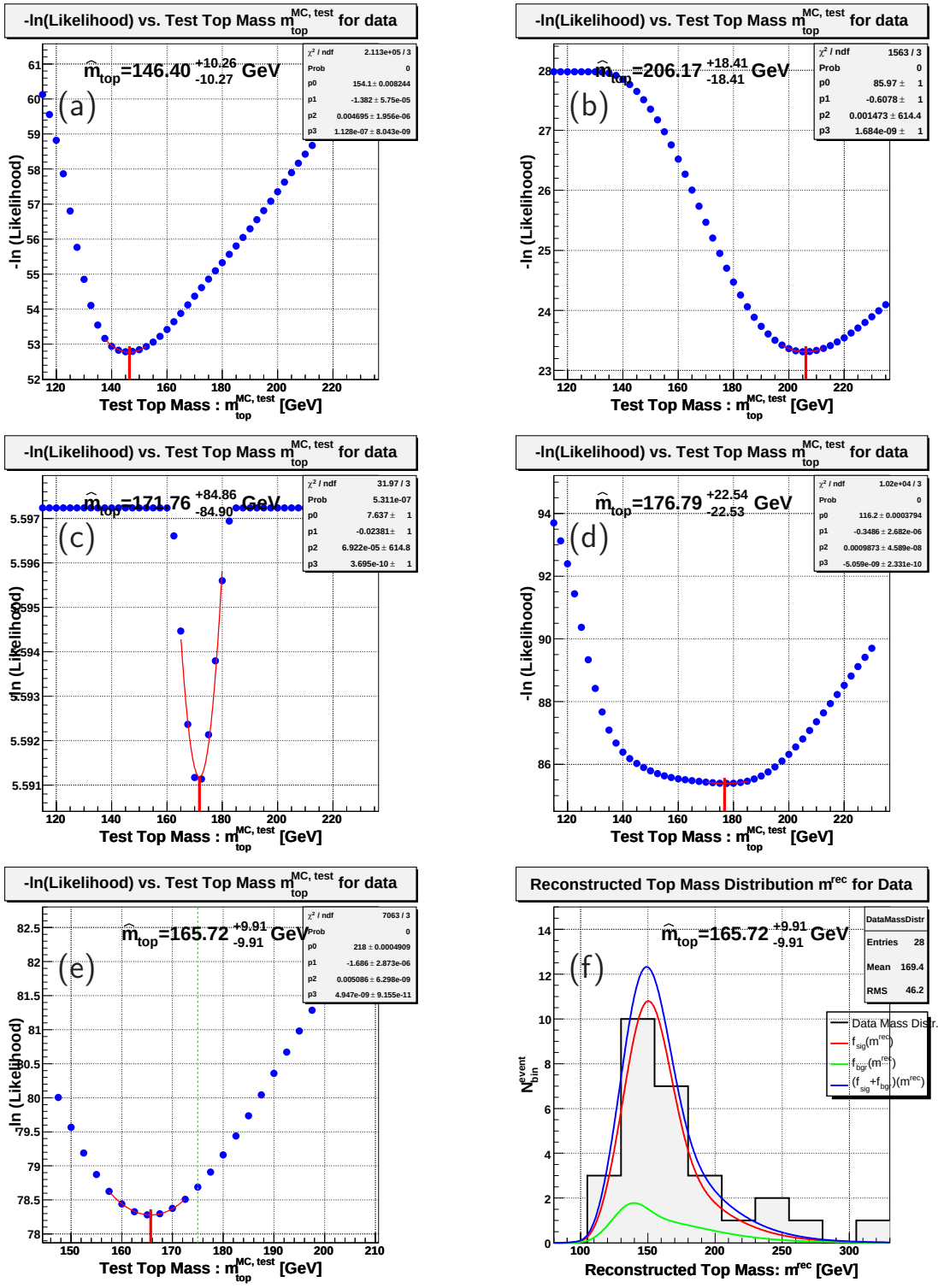

Figure 8.1.: Distributions of the negative logarithmic likelihood for the events selected in data. The numbers in the plot give the measured top quark mass $\hat{m}_{\text{top}}$ and its statistical error $\hat{\sigma}_{m_{\text{top}}}$, as determined with the cubic fit. In (a), (b), and (c) the $e\mu$, ee, and $\mu\mu$ channel of the 370 pb^{-1} dataset reconstructed with version `p14` of `D0Reco` are shown; in (d) the combination of their likelihoods. For the $e\mu$ channel of the 835 pb^{-1} dataset and `p17`, (e) depicts the $-\ln\mathcal{L}$ distribution, in (f) the distribution of top quark masses reconstructed with the Neutrino Weighting and the Maximum Methods, $m_{\text{top}}^{\text{rec}}$. In the same plot the signal and background probability density functions are drawn scaled to their yields, as well as their sum (red/middle, green/lower, blue/upper line, respectively).

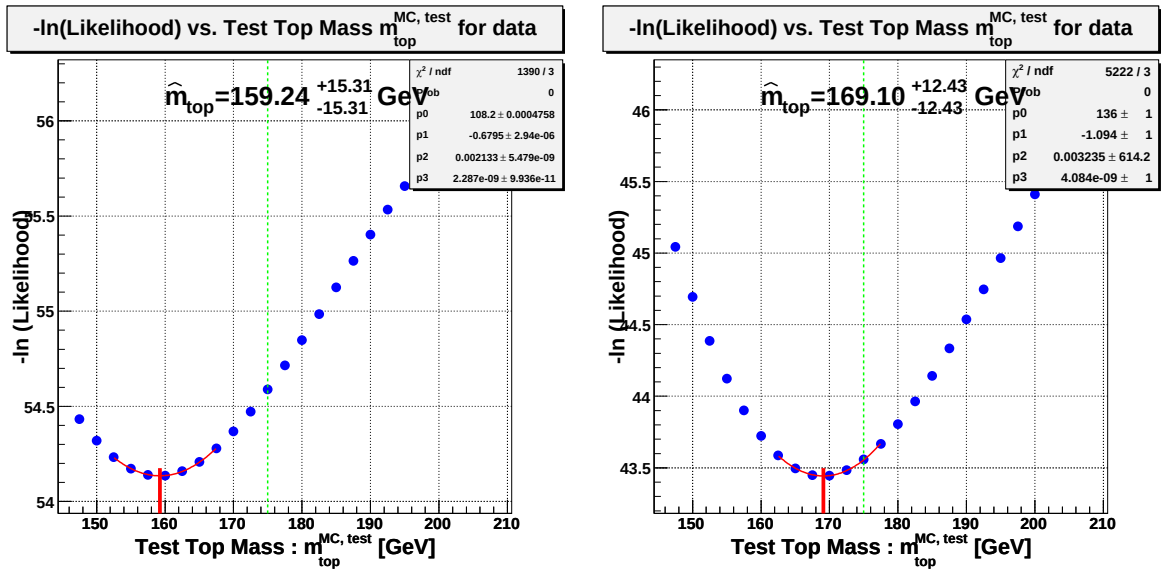

Figure 8.2.: The results of the negative logarithmic likelihood fit to the $370\,\mathrm{pb}^{-1}$ part of the $835\,\mathrm{pb}^{-1}$ dataset reconstructed with version `p17` of the DØ software (left hand side). The corresponding plot for the $465\,\mathrm{pb}^{-1}$ datasubset collected after August 2004 is shown on the right hand side. The numbers in the plots give the measured top quark mass values and their statistical errors before calibration.

combined using the canonical formulae

$$\hat{m}_{\mathrm{top}}^{370+465\,\mathrm{combined}} = \left(\frac{\hat{m}_{\mathrm{top}}^{370}}{(\hat{\sigma}_{m_{\mathrm{top}}}^{370})^2} + \frac{\hat{m}_{\mathrm{top}}^{465}}{(\hat{\sigma}_{m_{\mathrm{top}}}^{465})^2}\right) \Big/ \left(\frac{1}{(\hat{\sigma}_{m_{\mathrm{top}}}^{370})^2} + \frac{1}{(\hat{\sigma}_{m_{\mathrm{top}}}^{465})^2}\right)$$

$$\frac{1}{\hat{\sigma}_{m_{\mathrm{top}}}^{370+465\,\mathrm{combined}}} = \sqrt{\frac{1}{(\hat{\sigma}_{m_{\mathrm{top}}}^{370})^2} + \frac{1}{(\hat{\sigma}_{m_{\mathrm{top}}}^{465})^2}}\,.$$

This results in a value of

$$\hat{m}_{\mathrm{top}}^{370+465\,\mathrm{combined}} = 165.2\ \mathrm{GeV} \pm 9.6\ \mathrm{GeV}$$

which compares very well with the result for the full dataset $m_{\mathrm{top}}^{835\,\mathrm{pb}^{-1}} = 165.7 \pm 9.9\,\mathrm{GeV}$ before calibration.

Another cross check was done by removing 1 event at a time from the selected dataset and evaluating the effect on the $-\ln\mathcal{L}$ distribution. No problematic behaviour was observed for the $835\,\mathrm{pb}^{-1}$ dataset and `p17`. However, for the $e\mu$ channel of the $370\,\mathrm{pb}^{-1}$ dataset and `p14` two such events were found: run #178159, event #37315440 with $m_{\mathrm{top}}^{\mathrm{rec}} = 120\,\mathrm{GeV}$ and run #194341, event #41954816, $m_{\mathrm{top}}^{\mathrm{rec}} = 126\,\mathrm{GeV}$. The left hand side of Fig. 8.3 shows the likelihood that results when removing these two events. The top mass is shifted by $\sim$15 GeV compared to the result shown in Fig. 8.1 (a). It is remarkable, that both events are present in `p17` and yield similar results for $m_{\mathrm{top}}^{\mathrm{rec}}$, but no such unstable behaviour is observed. To enlighten this puzzle, one has to keep in mind, that the other events in the $e\mu$ channel data samples of `p14` and `p17` play a role. On the other hand, a significant effect was found to be caused by the signal probability density functions, which for the same generated top quark mass $m_{\mathrm{top}}^{\mathrm{MC,input}}$ are shifted towards higher values by some 5-7 GeV for `p17` with respect to `p14`. This is demonstrated in Fig. 8.4 for

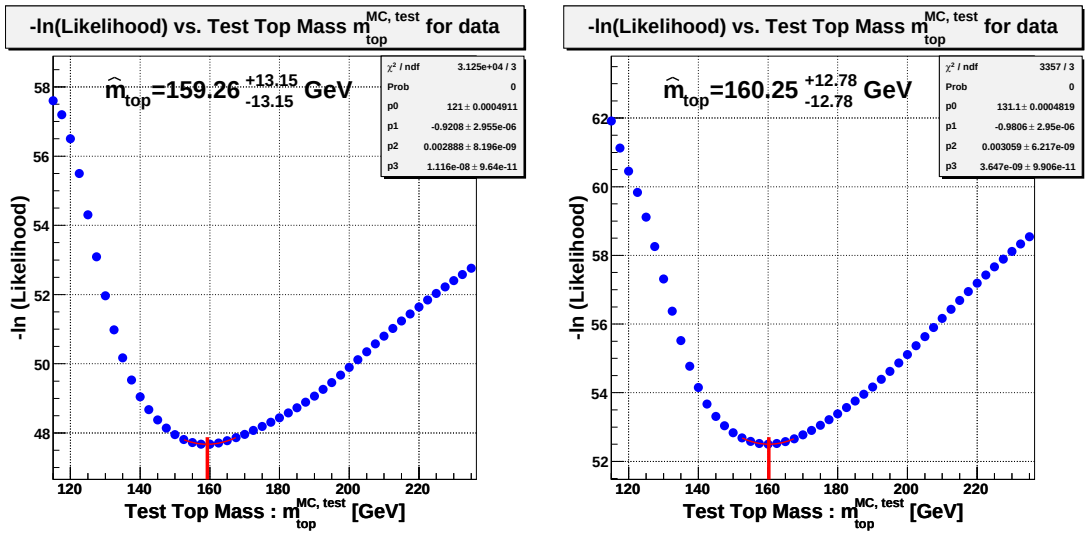

Figure 8.3.: The left hand side shows the effect on the likelihood for the $e\mu$ channel of the $370\,\mathrm{pb}^{-1}$ dataset reconstructed in `p14` when removing two events: run #178159, event #37315440 and run #194341, event #41954816, the two events with lowest top quark masses $m_{\mathrm{top}}^{\mathrm{rec}}$, as reconstructed with the Neutrino Weighting Method. On the right hand side, the negative logarithmic likelihood distribution for data in the $e\mu$ channel of the $370\,\mathrm{pb}^{-1}$ dataset reconstructed with version `p14` of the DØ software is presented. The likelihood was calculated using the signal probability density functions produced with Monte Carlo for `p17`. The sanity of this cross check is discussed in the text.

the $e\mu$ channel and a generated top quark mass of $m_{\mathrm{top}}^{\mathrm{MC,input}} = 175\,\mathrm{GeV}$. The meaning of this is that for the latter the reconstructed top quark mass $m_{\mathrm{top}}^{\mathrm{rec}}$ tends to be lower in Monte Carlo events, which was used to produce the probability density functions. It is not surprising, given the big difference between `p14` and `p17`, starting with the generators: ALPGEN for the former, PYTHIA for the latter. However, if one compares characteristic physics objects quantities like the transverse momenta p_T in data events reconstructed with `p14` and `p17`, in contrast to Monte Carlo no significant difference is observed. This fact might be pointing towards differences between data and Monte Carlo.

A very important cross check is to relate the two results for the $e\mu$ channel of the $370\,\mathrm{pb}^{-1}$ dataset for `D0Reco` versions `p14` and `p17`. The top quark mass before calibration for `p14` is $146.4 \pm 10.3\,\mathrm{GeV}$, which is approximately 1σ away from the `p17` result for the same dataset ($m_{\mathrm{top}} = 159.2 \pm 15.3\,\mathrm{GeV}$) and 2σ from the world average ($m_{\mathrm{top}} = 171.4 \pm 2.1\,\mathrm{GeV}$ [10]). To further investigate this issue, the Neutrino Weighting / Maximum Methods have been applied to the $e\mu$ channel of the $370\,\mathrm{pb}^{-1}$ dataset reconstructed with `p14`, however using the `p17` signal probability density functions. The resulting likelihood is shown in Fig. 8.3. The Maximum Likelihood formalism yields

$$m_{\mathrm{top}}^{\mathrm{Xcheck}} = 160.3 \pm 12.8\,\mathrm{GeV}\,,$$

which compares to the corresponding "all-`p17`" value of $m_{\mathrm{top}}^{\mathrm{p17},370\,\mathrm{pb}^{-1}} = 159.2 \pm 15.3\,\mathrm{GeV}$. One has to keep in mind that no strong conclusion can be drawn from this comparison, since although the datasets are the same, some of the selected events are different due to the improved data quality in `p17` with respect to `p14`.

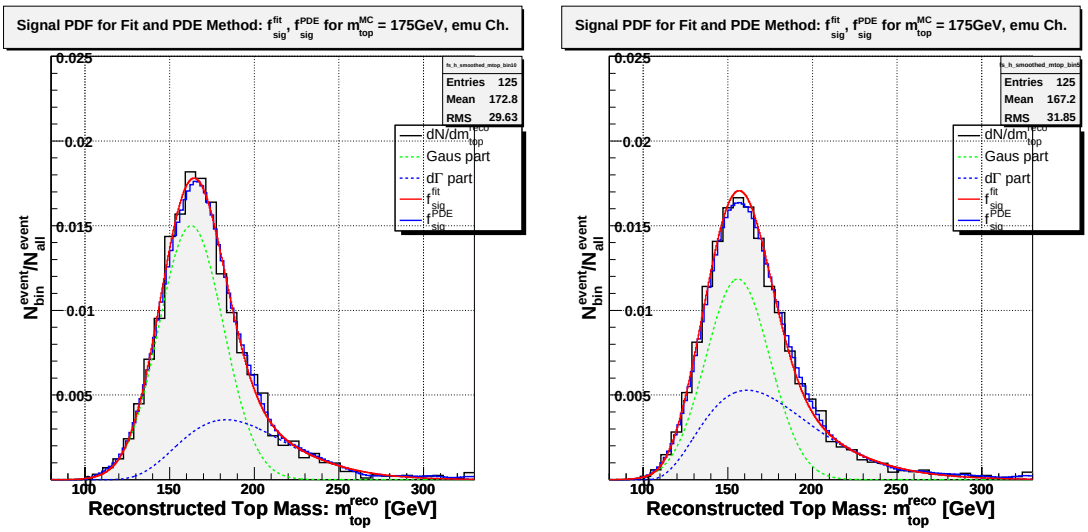

Figure 8.4.: The signal probability density function $f_{\mathrm{sig}}(m^{\mathrm{rec}}|m_{\mathrm{top}}^{\mathrm{MC}})$ (smooth solid red line) for $m_{\mathrm{top}}^{\mathrm{MC}} = 175\,\mathrm{GeV}$ for the $e\mu$ channel and versions `p14` (left hand side) and `p17` (right hand side) of the DØ software.

9. Systematic Uncertainties

In this chapter various sources for systematic uncertainties on the top quark mass measurement will be discussed. For the $370\,\mathrm{pb}^{-1}$ dataset reconstructed in `p14`, where explicitly said, the errors are quoted from [82]. This is a valid approach due to the high correlation of the Binned Template and the Maximum Method. For some of the systematic uncertainties for the $e\mu$ channel of the $835\,\mathrm{pb}^{-1}$ dataset reconstructed with version `p17` of the DØ software the numbers were worked out anew, for some the results found in [82] are taken, since these errors do not scale with luminosity. These numbers are described in [12, 13]. Finally, the total systematic uncertainty will be given for both datasets and `D0Reco` versions.

9.1. Systematic Uncertainty due to the Jet Energy Scale

The main systematic uncertainty is expected to arise from the uncertainty on the jet energy scale (JES). The jet energy scale is a mapping of the energy measured in the calorimeter to the real energy of the quark or gluon. In this mapping a sophisticated algorithm is involved, which takes into account the lateral and transverse jet profile, other physics objects in a given event, the calorimeter response, etc. The effect of the uncertainty on the jet energy scale has been evaluated for both datasets and `D0Reco` versions by producing calibration curves for Monte Carlo events reconstructed with the jet energy scale shifted by $\pm 1\sigma$ and nominal signal and background probability density functions. When shifting the jet energies, the $\not\!\!E_T$ of the event is corrected for the change. The jet energy scale uncertainty will be discussed separately for the two datasets in the following.

9.1.1. JES Uncertainty for the $370\,\mathrm{pb}^{-1}$ dataset and `p14`

For the $370\,\mathrm{pb}^{-1}$ dataset reconstructed using version `p14` of DØ software, the systematic uncertainty on the energy of jets is assumed to arise from three factors: an uncertainty of 3.4% on the correction to the jet energy of light quarks [103], an uncertainty of 2.6% on the Monte Carlo based light quark to b-quark correction [63], and a constant 1% error from p_T-dependent uncertainties [103]. These uncertainties are added up in quadrature and yield an overall uncertainty of 4.1% for the energy of a given jet. Applying the algorithm as described above yields the calibration curves as displayed on the left hand side of Fig. 9.1 and

$$(\Delta m_{\mathrm{top}})^{\mathtt{p14}}_{\mathrm{JES}} = ^{+3.6}_{-4.5}\ \mathrm{GeV}\,.$$

for the uncertainty on the top quark mass due to the jet energy scale.

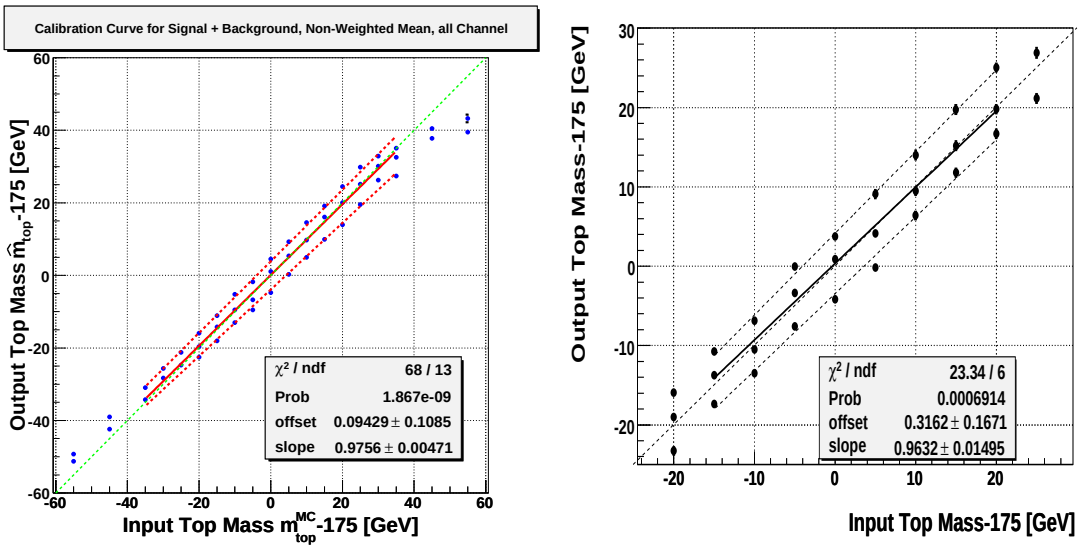

Figure 9.1.: Calibration curves after varying the jet energy scale by $\pm 1\sigma$ as determined with Monte Carlo events for the $370\,\mathrm{pb}^{-1}$ dataset reconstructed in `p14` on the left hand side and the $e\mu$ channel of the $835\,\mathrm{pb}^{-1}$ dataset and `p17` on the right hand side.

9.1.2. JES Uncertainty for the $e\mu$ channel of the $835\,\mathrm{pb}^{-1}$ dataset and `p17`

For the $835\,\mathrm{pb}^{-1}$ dataset reconstructed with the `p17` version of `D0Reco` the total uncertainty on the jet energy scale is calculated from the statistical and systematic contribution for data and Monte Carlo event-wise and jet-wise according to:

$$\sigma_{\mathrm{total}}^{\mathrm{jes}} = \sigma_{\mathrm{stat}}^{\mathrm{MC\,jes}} \oplus \sigma_{\mathrm{syst}}^{\mathrm{MC\,jes}} \oplus \sigma_{\mathrm{stat}}^{\mathrm{data\,jes}} \oplus \sigma_{\mathrm{syst}}^{\mathrm{data\,jes}} ,$$

as documented in [104]. This results in calibration curves presented on the right hand side of Fig. 9.1. The uncertainty on the top quark mass due to the jet energy scale is

$$(\Delta m_{\mathrm{top}})_{\mathrm{JES}}^{\mathtt{p17}} = ^{+3.6}_{-3.9}\ \mathrm{GeV}\,.$$

9.2. Systematic Uncertainty due to the Jet Resolution

The finite energy resolution of jets, as described in Chap. 5, can also lead to a systematic shift in the top quark mass. For the $370\,\mathrm{pb}^{-1}$ dataset, reconstructed in `p14`, this source of systematics was estimated with a special Monte Carlo signal sample for a top quark mass of $m_{\mathrm{top}}^{\mathrm{MC,input}}$, in which the jets have been smeared with the smearing parameters shifted by $\pm 1\sigma$ from their nominal values. The standard selection was applied. The top quark mass has been measured in pseudo-experiments comprised from events in this sample using the nominal signal and background probability density functions. For the $370\,\mathrm{pb}^{-1}$ dataset and `p14` the systematic error on the top quark mass due to the jet resolution uncertainty is [82]:

$$(\Delta m_{\mathrm{top}})_{\mathrm{jet\ res.}}^{\mathtt{p14}} = 0.5\,\mathrm{GeV}\,.$$

For the $e\mu$ channel of the 835 pb^{-1} dataset and `p17` the corresponding error was re-evaluated [12, 13], since it does improve with detector calibration and partially improves with more statistics available:

$$(\Delta m_{\text{top}})^{\texttt{p17}}_{\text{jet res.}} = 0.4\,\text{GeV}\,.$$

9.3. Systematic Uncertainty due to the Muon Resolution

The systematic error on the top quark mass due to the uncertainty on the muon resolution for the 370 pb^{-1} dataset and `p14` was calculated in much the same way as for the jets, with the difference that no special Monte Carlo samples exist and the present Monte Carlo sample was smeared with resolution parameters shifted by $\pm 1\sigma$. The resulting oversmearing of the muons has been found to cause very little difference in the maximum likelihood fit, as was found with oversmearing with default parameters. The error due to the muon resolution uncertainty for the results with both datasets and `D0Reco` versions is [82, 12, 13]:

$$(\Delta m_{\text{top}})^{\texttt{p14,p17}}_{\text{muon res.}} = 0.4\,\text{GeV}\,.$$

This value is taken for `p17` as well, since the muon resolution is not expected to improve with a larger dataset because of high multiplicity effects due to the increased luminosity. Tracking studies to significantly improve these resolutions are still to be done.

For the electron resolution, no systematic uncertainty on the top quark mass is evaluated, since the measurement of the electron is relatively precise and for this reason is expected to take little effect compared to the resolutions of other physics objects.

9.4. Systematic Uncertainty from Extra Jets

A significant source for systematics arises from the modeling of initial and final state radiation and extra jets in the production diagram. In fact, for approximately 32% of selected $t\bar{t}$ events 1 extra jet is expected, wheras approximately 8% will contain 2 [12, 13]. For the 370 pb^{-1} dataset reconstructed using version `p14` of DØ software, this error is estimated with a Monte Carlo sample of $t\bar{t}$ events containing one extra jet for a top quark mass of $m_{\text{top}}^{\text{MC,input}}$. The same procedure is used as for the jet resolution systematics. The difference in the result for the $t\bar{t}+j$ sample was found to be 2.5 GeV. There is no $t\bar{t}+jj$ Monte Carlo sample, therefore the error here is conservatively estimated as twice the error for the $t\bar{t}+j$ sample. Both errors are scaled by their fractional contribution to the $t\bar{t}$ yield. The systematic error on the top quark mass from associated jets for both versions of `D0Reco` and the results with both datasets is [82, 12, 13]:

$$(\Delta m_{\text{top}})^{\texttt{p14,p17}}_{\text{extra jets}} = 1.2\,\text{GeV}\,.$$

This error is taken for the `p17` analysis, since it is not connected to the size of the selected dataset, as it is estimated using Monte Carlo. For the next years to come the Tevatron is too far away from the integrated luminosity needed to allow studies of $t\bar{t}+nj$ events in data.

9.5. Systematic Uncertainty due to the Parton Distribution Functions

For historic reasons, in the $e\mu$ channel of the $370\,\mathrm{pb}^{-1}$ dataset reconstructed with version `p14` of `D0Reco` the error on the parton distribution functions used for event generation was evaluated by comparing PDF's provided by various working groups and in different versions. However, this is not an appropriate approach, since all their results are based on basically the same dataset. The correct approach would be to use the 40-dimensional error correlation matrix provided with CTEQ6.1M parton distribution functions, as was the Tevatron-wide consensus [105].

In [82], the estimation of the systematic error due to the imprecise knowledge of PDF's was done in the following way: the top quark mass has been measured for Monte Carlo events generated using various parton distribution functions (see [82] for the full list) using the nominal probability density functions for signal and background produced with CTEQ5L. For the systematic uncertainty half the difference between the highest and the lowest value are taken. This results in a value of 0.6 GeV. To estimate this uncertainty for all channels in `p14`, the error is scaled up by $\sqrt{23/17}$. For all channels of the $370\,\mathrm{pb}^{-1}$ dataset as well as for the $e\mu$ channel of the $835\,\mathrm{pb}^{-1}$ dataset the systematic uncertainty on the top quark mass due to parton distribution functions is [82, 12, 13]:

$$(\Delta m_{\mathrm{top}})^{\texttt{p14,p17}}_{\mathrm{PDF}} = 0.7\,\mathrm{GeV}\,.$$

This error estimation is used for `p17`, since it is an uncertainty due to improper modelling in Monte Carlo and is not connected to the rising integrated luminosity of the Tevatron. This error decreases with more data collected in deep inelastic scattering experiments, e.g. at DESY.

9.6. Systematic Uncertainty due to the Background Probability Distribution Shape

The low statistics for the background Monte Carlo sources caused by a very low selection efficiency introduces a significant uncertainty on the top quark mass due to the background probability distribution shape. For the $370\,\mathrm{pb}^{-1}$ dataset and `p14` it was estimated by generating dummy events with the PMCS[1] simulator [106]. The Neutrino Weighting algorithm combined with the Maximum Method were applied to them. For both approaches, nominal signal and background probability density functions were used. For the $370\,\mathrm{pb}^{-1}$ dataset reconstructed with `p14` for the uncertainty due to the background probability density shape was obtained [82]:

$$(\Delta m_{\mathrm{top}})^{\texttt{p14}}_{\mathrm{bgr.\ shape}} = 0.7\,\mathrm{GeV}\,.$$

For the $835\,\mathrm{pb}^{-1}$ dataset and version `p17` of the DØ software, the following approach is used: the $Z \to \tau\tau$ background is substituted with WW and a modified background probability distribution $f_{\mathrm{bgr}}(m^{\mathrm{rec}}_{\mathrm{top}})$ is produced. The modified background probability density distribution is used and the same set of 500 pseudo-experiments for each generated Monte Carlo top quark mass point

[1] PMCS – Parametrised Monte Carlo Simulator is a tool to produce events with little computing power by using smearing with parametrised parameters rather than the full GEANT ([65]) detector simulation. As input, the events at generator level are used.

performed, as done before. For the $e\mu$ channel of the $835\,\mathrm{pb}^{-1}$ dataset and `p17`, the uncertainty due to the background probability density shape is estimated to be [12, 13]:

$$(\Delta m_{\mathrm{top}})^{\mathtt{p17}}_{\text{bgr. shape}} = 0.3\,\mathrm{GeV}\,.$$

9.7. Systematic Uncertainty due to the $Z \to \tau\tau$ Background Yield

As detailed in Chap. 4, DØ currently observes a deviation in the 0- and 1-jet bin with the $e\mu$ channel of the $835\,\mathrm{pb}^{-1}$ dataset reconstructed with version `p17` of `D0Reco`. This deviation is believed to result from a misunderstanding of the $Z \to \tau\tau$ background. Therefore, a systematic error on the yield of this process is introduced. It is estimated by analysing pseudo-experiments with the $Z \to \tau\tau$ yield increased by its error. For the systematic uncertainty on the top quark mass in the $e\mu$ channel of the $835\,\mathrm{pb}^{-1}$ dataset and `p17` due to the error on the background yield is obtained:

$$(\Delta m_{\mathrm{top}})^{\mathtt{p17}}_{\text{yield}} = 0.3\,\mathrm{GeV}\,.$$

It is expected that this problem will be resolved with more data. If not, a new systematic source due to the modelling and lacking understanding of the background will have to be introduced.

9.8. Summary of Systematic Uncertainties

Source	$\Delta m_{\mathrm{top}}^{\mathtt{p14}}$	$\Delta m_{\mathrm{top}}^{\mathtt{p17}}$ [GeV]
Jet Energy Scale	$^{+3.6}_{-4.5}$	$^{+3.6}_{-3.9}$
Jet Resolution	0.5	0.4
Muon Resolution	0.4	0.4
Extra Jets	1.2	1.2
PDF	0.7	0.7
Background Shape	0.7	0.3
$Z \to \tau\tau$ Yield	-	1.0
Total Systematic Error	$^{+4.0}_{-4.8}$	$^{+3.9}_{-4.2}$

Table 9.1.: Summary of systematic uncertainties for the dilepton channels final states of the $370\,\mathrm{pb}^{-1}$ dataset reconstructed with version `p14` of DØ software and for the $e\mu$ channel of the $835\,\mathrm{pb}^{-1}$ dataset reconstructed with `p17`. The total systematic uncertainty was calculated as a quadratic sum of the individual contributions.

10. Conclusion

In the following, the results obtained using the Neutrino Weighting algorithm combined with the Maximum Method will be summarised including both the statistical and the systematic error, as determined in Chap. 8 and 9. These final figures will be compared with other top quark mass measurements in dileptonic final states at DØ. Finally, the compatibility with the world average top quark mass will be discussed.

10.1. Summary of Quantitative Results Found

With the Neutrino Weighting algorithm combined with the Maximum Method and taking into account the statistical and systematic error, as well as calibrating the results according to Eqn. 7.3 the combined dilepton channel top quark mass result is:

$$m_{\text{top}}^{370\,\text{pb}^{-1}} = 176.8\ ^{+17.5}_{-29.3}\ (\text{stat.})\ ^{+4.0}_{-4.8}\ (\text{syst.})\,\text{GeV}$$

in the $370\,\text{pb}^{-1}$ dataset reconstructed with version `p14` of DØ software. Channel-wise, with statistical error only and without any calibration is found:

$$\begin{aligned} m_{\text{top}}^{e\mu} &= 146.4 \pm 10.3\,\text{GeV}\,, \\ m_{\text{top}}^{ee} &= 206.2 \pm 18.4\,\text{GeV}\,, \\ m_{\text{top}}^{\mu\mu} &= 171.8 \pm 84.9\,\text{GeV}\,. \end{aligned}$$

Analogously, taking into account the statistical and systematic error, as well as the calibration, in the $e\mu$ channel of the $835\,\text{pb}^{-1}$ dataset reconstructed with version `p17` of DØ software the top quark mass is measured to be:

$$m_{\text{top}}^{835\,\text{pb}^{-1}} = 165.5 \pm 10.0(\text{stat.})\ ^{+3.9}_{-4.2}\ (\text{syst.})\,\text{GeV}\,.$$

10.2. Comparison with other Methods at DØ Using Dilepton Final States

In this section, the results presented in this thesis and in [12, 13], as found with the Neutrino Weighting / Maximum Method, will be compared with the results obtained in other analyses at DØ using dilepton final states.

10.2.1. Comparison for the 370 pb^{-1} Dataset

For the 370 pb^{-1} dataset and `p14` there are two other analyses measuring the mass of the top quark at DØ: the Binned Template Neutrino Weighting Method which uses a 10-bin template to analyse the weight distribution [82] and the Matrix Weighting Method, which uses a simplified matrix element calculation to obtain a weight [107].

The *Matrix Weighting Method* was applied to a sample obtained with the same selection as this analysis and a sample of events where at least one of the jets is required to have a b-tag. The comparison is made for the former dataset. With the Matrix Weighting Method DØ measures considering statistical errors only channel-wise (before calibration) and combined (calibrated):

$$\begin{aligned} m_{\text{top}}^{e\mu} &= 148 \pm 11\,\text{GeV} \\ m_{\text{top}}^{ee} &= 188 \pm 15\,\text{GeV} \\ m_{\text{top}}^{\mu\mu} &= 186 \pm 35\,\text{GeV} \\ m_{\text{top}}^{\text{all}} &= 165.0 \pm 13.5\,\text{GeV}\,. \end{aligned}$$

The per-channel figures are compatible with the results obtained using the Neutrino Weighing Method combined with the Maximum Method presented in this thesis.

The *Binned Template Neutrino Weighting Method* has the same selections for the ee and $\mu\mu$ channels as the Maximum Method. For the $e\mu$ channel an older version of the selection is used with a cut on H_T and $\not\!\!E_T$, which yields 15 events. To determine the signal and background probability density functions the Probability Density Estimation (PDE) approach is followed. With the Binned Template Neutrino Weighting Method, DØ measures channel-wise (before calibration) and combined (calibrated):

$$\begin{aligned} m_{\text{top}}^{e\mu} &= 148 \pm 11\,\text{GeV} \\ m_{\text{top}}^{ee} &= 198 \pm 17\,\text{GeV} \\ m_{\text{top}}^{\mu\mu} &= 183 \pm 34\,\text{GeV} \\ m_{\text{top}}^{\text{all}} &= 176.4 \pm 11.4\,\text{GeV}\,, \end{aligned}$$

with only statistical errors given. The likelihood distributions are displayed in Fig. 10.1. The per-channel results are in good agreement with the measurements presented in this thesis.

However, for both alternative methods, the combined result shows a large deviation in the statistical error with respect to the analysis presented here. This can be explained by the fact that the Binned Template Method uses the PDE approach for smoothing of the probability density functions, which results in a systematic bias in the fits to the likelihood points, as detailed in Sec. 6.4. In fact, a much larger error should be obtained when a statistical combination of measurements more than 3σ away from each other and similar magnitudes of statistical errors is made, as is the case here.

10.2.2. Comparison for the 835 pb^{-1} Dataset

The situation with analyses using the $e\mu$ channel of the 835 pb^{-1} dataset reconstructed with version `p17` of DØ software is different. There are 3 analyses (including this) that take the

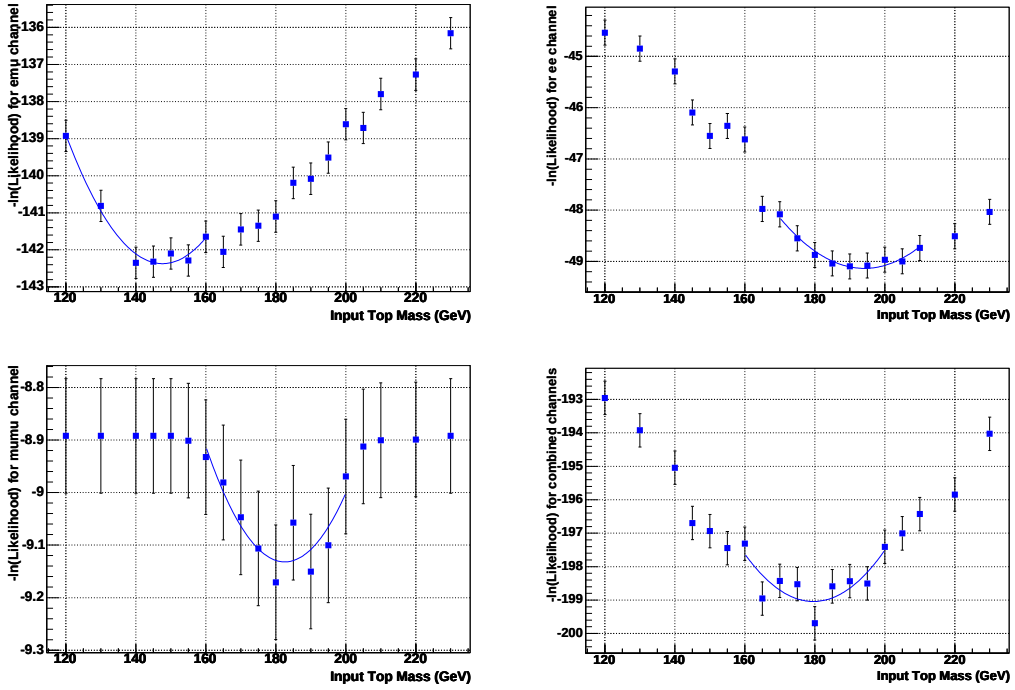

Figure 10.1.: The likelihood distributions for the 370 pb^{-1} dataset and `p14`, as found with the Binned Template Method [82]. Going from left to right and from top to bottom the $e\mu$, ee, $\mu\mu$ channel and their combination are shown.

weight distributions produced with the Neutrino Weighting algorithm as input [12, 13], plus the Matrix Weighting Method [85]. All `p17` analyses are based on exactly the same selection both for data and Monte Carlo. In the following, the results obtained with these methods will be briefly overviewed in the following. They are not meant as cross-checks.

In the algorithm of the *Matrix Weighting Method* no major changes worth mentioning have been made with respect to the `p14` version of this analysis. DØ measures using this method after calibration and considering the statistical error only:

$$m_{\mathrm{top}}^{\mathrm{MWT}} = 177.7 \pm 8.8\,\mathrm{GeV}\,.$$

As already mentioned, there are currently three analyses at DØ that are based on the Neutrino Weighting Method:

- *Binned Template Method*: here the event weight distribution is coarsely re-binned into 5 bins and their entries are used to produce probability density functions after smoothing with the PDE approach. There are significant improvements of the analysis technique with respect to the version used for `p14`, the major one being the transformation of the binned event weights to non-correlated variables and a mirroring approach when estimating the probability density. It takes care of the overall normalisation of the probability density for the entries close to the bin range boundaries, where the Gaussian kernel used in the PDE smoothing approach significantly exceeds the allowed range of $[0, 1]$. The likelihood distribution for data is shown in Fig. 10.2. DØ measures (after calibration and considering

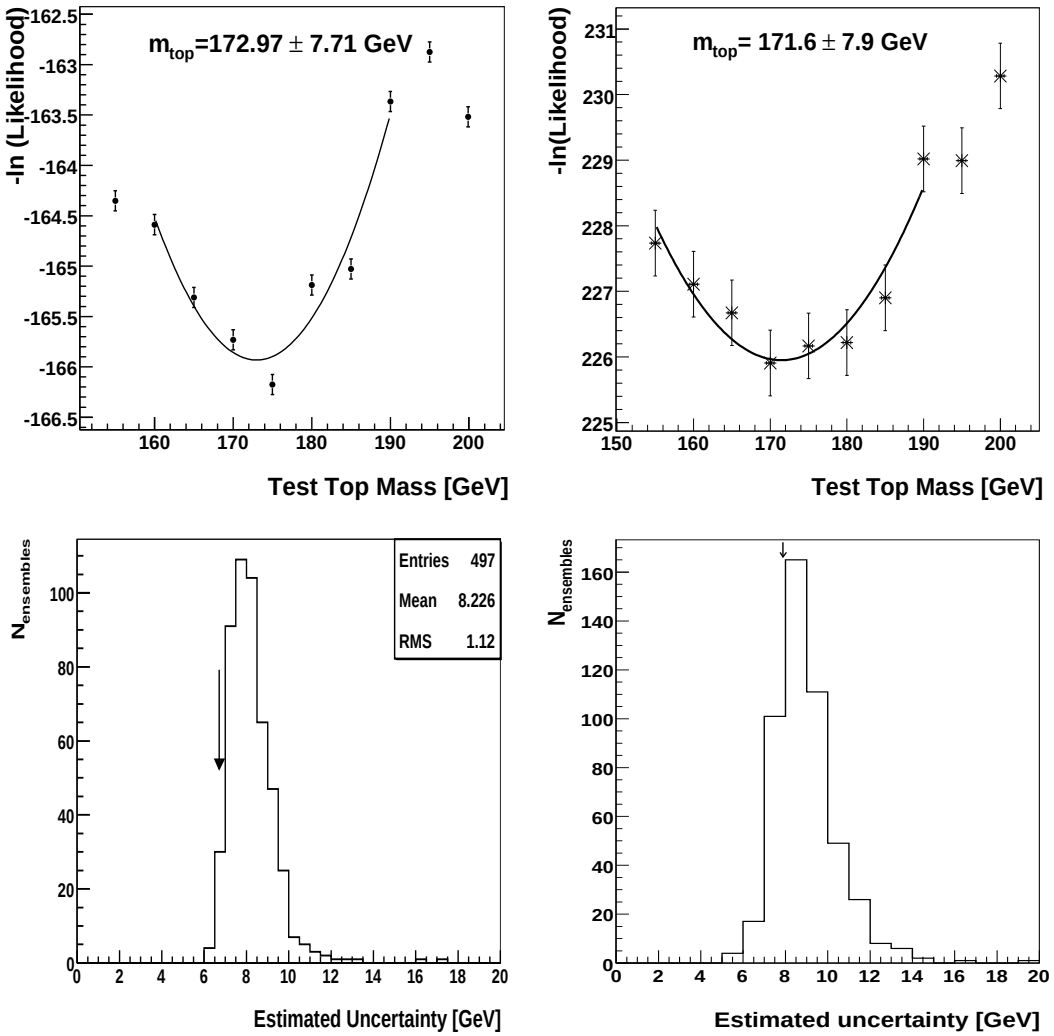

Figure 10.2.: The likelihood distributions for the 835 pb^{-1} dataset and `p17`, as found with the Binned Template Method (top left plot) and the Moments Method (top right plot). The expected statistical errors are shown in the bottom left and right plots [12, 13]. The arrows mark the statistical error measured in the selected data sample.

the statistical error only) with the Binned Template Method:

$$m_{\mathrm{top}}^{5\ \mathrm{bin}} = 173.6 \pm 6.7\,\mathrm{GeV}\,.$$

- *Moments Method*: with this approach the first and the second moment (the mean and the root mean square) are used as input variables from the event weight distribution obtained with the Neutrino Weighting Method. The PDE smoothing algorithm is used to obtain the probability density functions. For data, the likelihood distribution is shown in Fig. 10.2. Using the Moments Method, DØ obtains after calibration and with statistical error only:

$$m_{\mathrm{top}}^{\mathrm{mom}} = 171.6 \pm 7.9\,\mathrm{GeV}\,.$$

- *Maximum Method*, as presented in this thesis. Using the Maximum Method, DØ measures

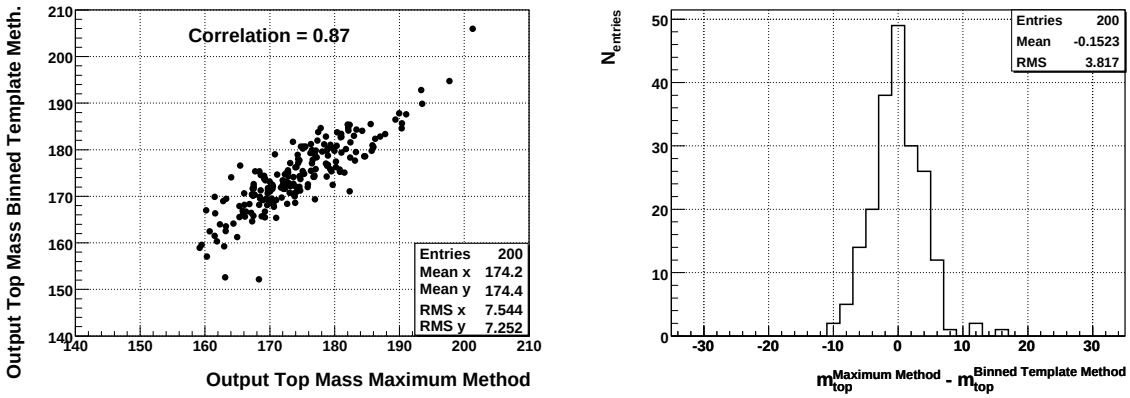

Figure 10.3.: The correlation between the Maximum Method and the Binned Template Method is shown in `p17` with 200 identical pseudo-experiments comprised of 28 signal events each: on the left hand side the scatter plot of the mass result in the Maximum Method versus the Binned Template Method, on the right hand side the difference between them.

after calibration and with statistical error only:

$$m_{\text{top}}^{\text{max}} = 165.5 \pm 10.0\,\text{GeV}\,.$$

All three methods based on the Neutrino Weighting algorithm as presented above provide a similar sensitivity to the top quark mass, as can be seen from the distribution of statistical errors in Fig. 7.4 for the Maximum Method and in Fig. 10.2 for the other two approaches. The Binned Template Method performs slightly better (however, here the pull width correction is included). Unfortunately, the Maximum Method is unlucky with the statistical error in the event sample selected in data.

The difference in the final result between the Maximum Method and the other two methods based on Neutrino Weighting is problematic. This has been tested using 200 identical pseudo-experiments for the Maximum Method and the Binned Template Method. The pseudo-experiments were formed from pure signal Monte Carlo for a top quark mass of $m_{\text{top}}^{\text{MC,input}} = 175\,\text{GeV}$ and analysed with both the Maximum Method and the Binned Template Method. A scatter plot of the Maximum Method results versus the Binned Template Method results as well as their difference are shown in Fig. 10.3. Both plots look sane – the correlation cloud has an elliptical shape along the bisector, the mass difference distribution has a Gaussian shape. The correlation coefficient for the two methods is:

$$\mathcal{C}(\text{Max}, 5\text{bin}) = 0.87\,.$$

A difference higher then 7.3 GeV, as found for the data results before calibration, is estimated to occur with a 6.5% probability.

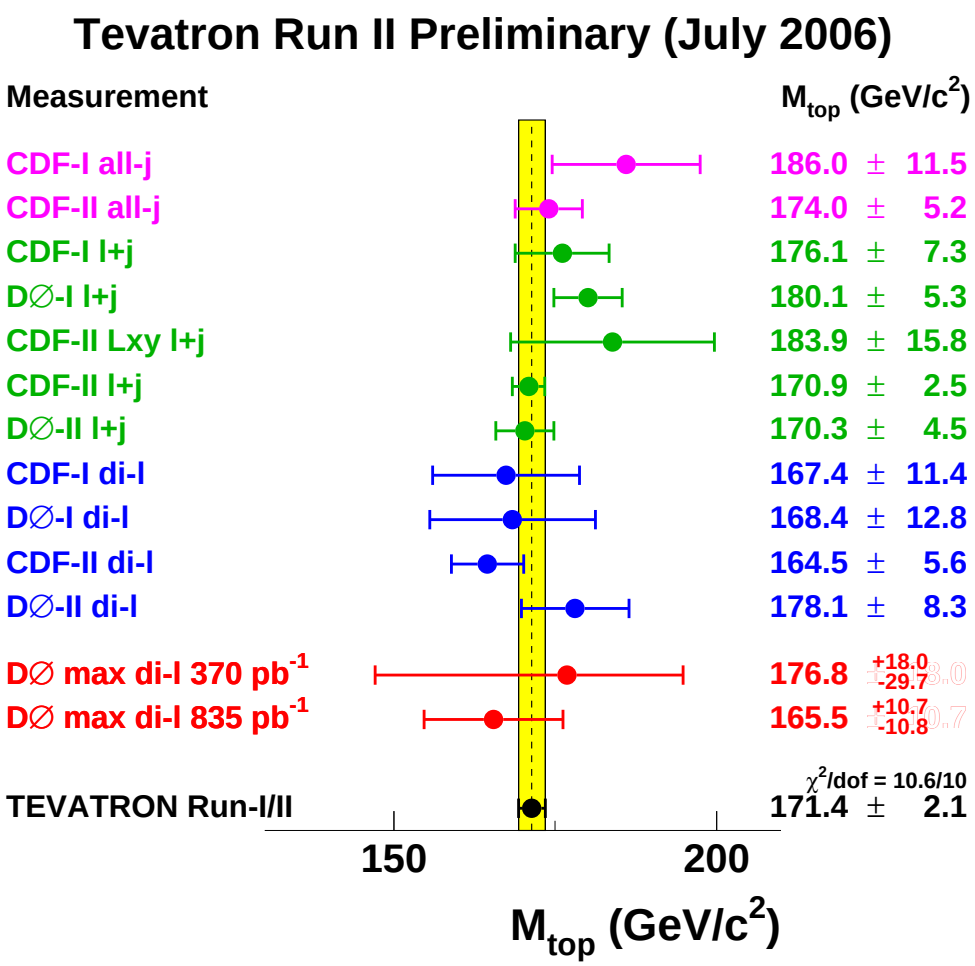

Figure 10.4.: The world average top quark mass with its error and the contributing measurements from DØ and CDF, splitted up into the dilepton, lepton+jets and all-jets channel, as in [10]. Both measurements presented in this thesis are shown in red in the two pre-last lines.

10.3. Comparison with the World Average Top Quark Mass

Both top quark mass measurements presented in this thesis,

$$m_{\text{top}}^{370\,\text{pb}^{-1}} = 176.8\ ^{+17.5}_{-29.3}\ (\text{stat.})\ ^{+4.0}_{-4.8}\ (\text{syst.})\,\text{GeV}\,,$$
$$m_{\text{top}}^{835\,\text{pb}^{-1}} = 165.5 \pm 10.0(\text{stat.})\ ^{+3.9}_{-4.2}\ (\text{syst.})\,\text{GeV}\,,$$

are in a good agreement within their expected errors with the world average top quark mass [10]:

$$m_{\text{top}}^{\text{world}} = 171.4 \pm 2.1\ (\text{stat.} + \text{syst.})\,\text{GeV}\,.$$

Due to its low systematic error and a high signal-to-background ratio, the top quark mass precision measurement in the dilepton channel is highly important and a valuable contribution. Further, it is a cross check of the Standard Model independent from the semileptonic and the all-jets channel.

The world average top quark mass with its errors and the contributing channels, in particular

the dilepton channel is visualised in Fig. 10.4.

10.4. Summary of Qualitative Results Found

In this Section, the qualitative findings of the Maximum Method combined with the Neutrino Weighting algorithm will be briefly summarised:

- Taking into account the per-channel numbers for the $370\,\mathrm{pb}^{-1}$ dataset reconstructed in `p14` as presented above and recapitulating the discussion in Chap. 8, the conclusion has to be drawn that the results found in `p14` are problematic. Not only are the results in the ee and $e\mu$ channel more than 3σ apart, moreover, the $e\mu$ channel is approx. 2σ away from the world average, which is not the case for the same dataset reconstructed in `p17`. It is remarkable, that the same is true for the result of the Binned Template Neutrino Weighting Method presented above. From all this a conclusion can be drawn that the improvement of data quality criteria and the data quality itself introduced with `p17` are indeed essential changes. However, it cannot be excluded that to a certain extent this problem is due to a lacking quality in the modelling of $t\bar{t}$ events in Monte Carlo, as discussed in Chap. 8. On the other hand, a statistical fluctuation cannot be fully excluded. Valuable insights to enlighten this question are pending – the ee and $\mu\mu$ channels reconstructed in `p17`.

- In the course of development of the Maximum Method the 2-dimensional fit approach, that is to fit the distributions of reconstructed top quark masses $m_{\mathrm{top}}^{\mathrm{rec}}$ for all available generated top quark masses $m_{\mathrm{top}}^{\mathrm{MC,input}}$ simultaneously with a 2-dimensional function was developed and introduced at DØ for the first time. The method used by DØ to produce probability density functions so far, the PDE smoothing approach was evaluated and found to be outperformed by the 2-dimensional fit method. The big advantage of the 2-dimensional fit approach is that for finite statistics available it automatically accounts for correlation between the signal Monte Carlo samples for all generated top quark masses, which is not the case with the PDE smoothing approach and leads to systematic errors. The other advantage is the analytical form of the likelihood, which can be used to introduce *any* number of additional points[1] for evaluating the likelihood function to minimise fit errors to a negligible level.

- A new method to extract the top quark mass in dilepton final state events – the Maximum Method combined with the Neutrino Weighting Method – has been developed and can be used in the future at DØ. The validity of this method has been tested in pseudo-experiments with simulated Monte Carlo events and found to be competitive with alternative approaches. The results obtained using this newly developed method in the $e\mu$ channel of the $835\,\mathrm{pb}^{-1}$ dataset were evaluated by the DØ collaboration and considered worth being shown at the ICHEP 2006 conference as an official "DØ Preliminary Result" [12, 13]. The work done is a small step towards an ever more precise measurement of the top quark mass, which is a fundamental parameter in the Standard Model, as detailed in Chap. 2.

[1] with the restriction, that the range of generated top quark masses cannot be exceeded by more than 10-20 GeV, as the fit cannot be extrapolated infinitely far away.

11. Outlook: Top Quark Mass Measurement in the Dilepton Channel

In this chapter, the improvement potential for the Maximum Method combined with the Neutrino Weighting algorithm as well as for the top quark mass measurements at DØ in general will be presented. Closing up, the prospects for the world average top quark mass measurement in the dilepton channel shall be given.

Outlook for the Neutrino Weighting / Maximum Method

- With the Maximum Method, only the maximum value of the mass probability distribution produced by the Neutrino Weighing algorithm is used. The 2-dimensional fit approach could be followed for additional variables characterising the mass weight distribution. Here, the most promising candidates are the first and the second moment, i.e. average and root mean square. A combined likelihood is to be defined as a product of the likelihoods for the individual variables to increase the statistical power.
- The analytic form of the likelihood could be used for simultaneous maximisation of the likelihood with respect to the signal and backround yields n_{sig} and n_{bgr} as well as the top quark mass $m_{\mathrm{top}}^{\mathrm{MC}}$. This way, no fits to the likelihood have to be performed. Following both of the first two suggestions could make the Neutrino Weighting algorithm combined with the 2-dimensional fit approach the most precise for the dilepton channel.
- More statistical power could be gained by including the ee and $\mu\mu$ channels for the $835\,\mathrm{pb}^{-1}$ dataset.
- For a significant fraction of dileptonic $t\bar{t}$ events additional jets are present, either from Initial / Final State Radiation or from splitting of the b-jets. Including the combinations for different jet pairings in the analysis could increase its precision and statistical power.
- For the $835\,\mathrm{pb}^{-1}$ dataset the QCD background has to be included in the analysis.
- The Maximum Method could be applied to lepton+track final state events with higher statistics, but also higher backgrounds.

Outlook for the Top Quark Mass Measurement in the Dilepton Channel at DØ

- At the current stage, the b-tagging algorithms for `p17` are extensively tested and improved to fully profit from the new version of DØ software. Very soon b-tagging information can be included in the analysis to identify at least one of the b-jets and thus increase the signal-to-background ratio,

- The understanding of the background has to be improved, in particular the yield for the $Z \to \tau\tau$ process,
- The new muon resolution parameters have to be determined for `p17`,
- The $\not\!\!E_T$ resolution has to be determined depending on the scalar E_T of the event, as done for `p14`,
- The jet energy scale uncertainty, being the source for the largest systematic error, must be studied and improved with more data collected.

Outlook on the World Top Mass Measurement in the Dilepton Channel

As already detailed in Chap. 2, besides offering a new test possibility for the Standard Model, the dilepton channel combines two big advantages: a high signal-to-background ratio and a low systematic error. These 2 prerequisites are essential for a precision measurement of the top quark mass.

A high signal-to-background ratio and a low systematic error become even more important with the begin of the LHC era, since the statistics will not be the limiting factor anymore thanks to a production rate of approximately 4 $t\bar{t}$ events per minute. For the dilepton channel, in the ideal case, the final state has 2 jets and 2 leptons which are measured with almost a δ-function like precision compared to jets. Thus the Jet Energy Scale uncertainty comes into play only twice. For the lepton+jets channel, the final state has 1 lepton as well as 2 b-jets and two other jets in the simplest scenario. Here, the JES uncertainty enters four times. Moreover, there are also some contributions to the Jet Energy Scale which are expected to stay constant on a time scale of several years, like the uncertainty of approximately 600 MeV due to the b-jets. This limit is set by the modelling quality of Monte Carlo because of the lack of well-understood physics processes for further b-jet studies. Uncertainties due to improper modelling of the background processes will also be much smaller for the dilepton channel due to the higher signal-to-background ratio, which can be ever increased with b-tagging, as they approximately scale with the fractional contribution of the background.

Until the end of this decade, a measurement of the top quark mass with a combined precision of 1-1.5 GeV is expected for the Tevatron. My hope is that the main effort documented in this thesis – the introduction of the 2-dimensional fit approach – will help the DØ collaboration to improve its contributions to the top quark mass world average in the future.

A. List of Selected Events and their Kinematics

Run	Event	$p_T(e)$	$p_T(\mu)$	$p_T(j_1)$	$p_T(j_2)$	$\not\!\!E_T$	N_{jets}	$m_{\text{top}}^{\text{rec}}$
168393	1997007	15.9	56.6	72.1	46.9	37.6	2	138
172952	6270376	55.9	69.4	94.5	37.5	38.0	2	170
174901	8710859*	136.5	29.6	85.3	82.5	71.0	4	262
177826	15259654*	51.3	80.2	147.6	107.4	71.9	2	138
178159	37315440*	109.3	123.4	60.8	41.6	39.5	2	120
178733	8735139	15.8	52.0	103.2	51.0	143.4	2	152
179141	11709332	30.5	52.5	53.8	36.9	32.2	2	142
179195	26386170	73.2	76.8	101.5	100.4	65.3	2	216
179331	19617820*	39.1	39.3	117.1	72.7	33.3	2	174
188675	41814068	52.0	16.2	109.4	36.6	148.5	2	190
188678	74966192*	56.9	17.1	120.4	71.5	55.3	2	142
189393	8877098	21.4	37.0	65.1	41.2	51.9	2	170
192536	4229461	67.9	213.8	57.2	38.6	139.7	2	202
193332	3472458*	65.1	48.2	192.3	80.9	155.1	2	204
194288	11639075	18.0	16.4	81.3	23.2	57.2	3	138
194340	26668184	19.8	51.0	70.7	31.4	30.7	2	148
194341	41954816*	67.2	16.5	48.0	36.5	69.5	2	126

Table A.1.: Data events selected in the $e\mu$ channel of the $370\,\text{pb}^{-1}$ dataset reconstructed with `p14`. Events with a "*" are selected with `p17`, too. The jets are p_T-sorted. The Table is adapted from [107]. All kinimatic quantities are given in GeV.

Run	Event	$p_T(l_1)$	$p_T(l_2)$	$p_T(j_1)$	$p_T(j_2)$	$\not\!\!E_T$	N_{jets}	$m_{\text{top}}^{\text{rec}}$
166779	121971120	55.5	19.9	97.7	37.0	109.5	2	164
170016	16809090	34.6	30.0	55.2	54.9	47.7	3	190
178177	13511001	97.7	18.9	120.6	51.8	81.8	2	184
178737	50812364	95.6	88.5	194.2	30.4	40.1	2	316
192663	4006566	41.6	28.5	85.0	48.9	48.7	2	210

Table A.2.: Data events selected in the ee channel of the $370\,\text{pb}^{-1}$ dataset reconstructed with `p14`. The leptons and jets are p_T-sorted. The Table is adapted from [107]. All kinimatic quantities are given in GeV.

Run	Event	$p_T(l_1)$	$p_T(l_2)$	$p_T(j_1)$	$p_T(j_2)$	$\not\!\!E_T$	N_{jets}	$m_{\text{top}}^{\text{rec}}$
189768	2578249	134.9	74.9	50.3	20.7	87.3	2	n/s
193986	374796	46.5	34.3	152.0	66.2	132.9	4	168

Table A.3.: Data events selected in the $\mu\mu$ channel of the $370\,\text{pb}^{-1}$ dataset reconstructed with `p14`. The leptons and jets are p_T-sorted. The Table is adapted from [107]. All kinimatic quantities are given in GeV.

Run	Event	$p_T(e)$	$p_T(\mu)$	$p_T(j_1)$	$p_T(j_2)$	$\not\!\!E_T$	N_{jets}	$m_{\text{top}}^{\text{rec}}$
169889	3627864	28.3	43.5	99.4	91.3	20.5	2	170
174901	8710859*	138.6	30.0	87.4	83.8	96.3	3	262
175669	38071382	57.7	36.5	60.0	30.5	74.8	2	134
177009	26597630	49.0	33.7	55.5	50.6	81.1	2	152
177826	15259654*	49.9	77.4	151.2	111.8	73.4	2	232
178159	37315438*	110.4	118.2	62.5	42.7	33.1	2	118
179331	19617819*	39.3	40.9	112.7	77.0	48.0	2	168
188678	74966192*	56.1	17.3	118.1	72.9	64.3	2	142
192963	4879306	48.3	30.0	106.0	67.2	34.7	2	182
193157	5386241	24.0	32.9	171.1	118.9	69.8	2	236
193332	3472458*	65.4	47.6	183.9	86.4	148.0	2	202
193993	56457785	33.1	18.3	54.0	49.6	62.8	2	158
194341	41954817*	67.4	16.4	50.4	35.5	61.4	2	120
195229	66560046	25.7	28.4	65.5	26.4	24.3	2	108
195839	48997902	41.2	48.5	50.1	26.0	71.9	2	138
202328	21928052	22.8	103.2	71.7	20.7	41.1	2	148
203318	9509737	42.3	31.6	66.9	47.0	46.9	2	142
203397	77017753	19.0	51.0	62.0	25.7	80.1	2	134
204404	12787510	17.6	53.0	71.6	43.8	58.8	2	164
204960	58964196	117.2	49.3	148.9	107.6	77.3	3	316
205966	59322987	16.5	140.0	47.8	38.2	62.3	2	216
206407	18543395	53.3	52.1	62.0	48.1	37.5	3	142
206616	22139900	69.8	49.4	162.7	128.9	107.1	2	184
206914	24343146	64.9	29.3	46.3	31.1	38.6	2	136
208690	6725690	129.6	40.6	139.0	51.3	32.2	2	166
209989	45331500	47.4	117.7	23.7	22.6	118.6	2	140
210520	59131455	24.6	43.3	70.3	34.2	42.3	2	156
211064	28741831	47.7	40.5	110.5	49.9	94.0	2	176

Table A.4.: Data events selected in the $e\mu$ channel of the $835\,\text{pb}^{-1}$ dataset reconstructed with `p17`. The jets are p_T-sorted. Events marked with a "*" are selected with version `p14` of the DØ software, too. The Table is adapted from [85]. All kinimatic quantities are given in GeV.

B. Kinematic Solution for the $\not\!\!E_T$ from Assumed Neutrino Pseudorapidities

In the following, the calculation of the $\not\!\!E_T$ vector from assumed neutrino and anti-neutrino pseudorapidities and a hypothetical m_{top} value, as performed with the Neutrino Weighting Method, presented in Chap. 5, will be given. The calculation as it appears here was written down by [92].

From a kinematical point of view, the process

$$t\bar{t} \rightarrow W^+ b W^- \bar{b} \rightarrow l^+ \nu l^- \bar{\nu}$$

is considered. The kinematical properties of particles in the final state are:

b-quark:	p_b	$=$	$(E_b, \vec{p}_b)$	$=$	$(E_b, p_b^x, p_b^y, p_b^z)$,	m_b	$=$	$4.3\,\text{GeV}$
$\bar{b}$-quark:	$p_{\bar{b}}$	$=$	$(E_{\bar{b}}, \vec{p}_{\bar{b}})$	$=$	$(E_{\bar{b}}, p_{\bar{b}}^x, p_{\bar{b}}^y, p_{\bar{b}}^z)$,	$m_{\bar{b}}$	$=$	$4.3\,\text{GeV}$
lepton:	p_{l^-}	$=$	$(E_{l^-}, \vec{p}_{l^-})$	$=$	$(E_{l^-}, p_{l^-}^x, p_{l^-}^y, p_{l^-}^z)$,	m_{l^-}	$\approx$	$0\,\text{GeV}$
antilepton:	p_{l^+}	$=$	$(E_{l^+}, \vec{p}_{l^+})$	$=$	$(E_{l^+}, p_{l^+}^x, p_{l^+}^y, p_{l^+}^z)$,	m_{l^+}	$\approx$	$0\,\text{GeV}$
neutrino:	p_ν	$=$	$(E_\nu, \vec{p}_\nu)$	$=$	$(E_\nu, p_\nu^x, p_\nu^y, p_\nu^z)$,	m_ν	$\approx$	$0\,\text{GeV}$
antineutrino:	$p_{\bar{\nu}}$	$=$	$(E_{\bar{\nu}}, \vec{p}_{\bar{\nu}})$	$=$	$(E_{\bar{\nu}}, p_{\bar{\nu}}^x, p_{\bar{\nu}}^y, p_{\bar{\nu}}^z)$,	$m_{\bar{\nu}}$	$\approx$	$0\,\text{GeV}$

As detailed in Chap. 5, the following kinematic constraints can be imposed:

$$m_W{}^2 = (p_l + p_\nu)^2 \tag{B.1}$$

$$m_t{}^2 = (p_l + p_\nu + p_b)^2 \,. \tag{B.2}$$

The following set of observables is measured in the detector: $p_b, p_{\bar{b}}, p_{l^+}, p_{l^-}$.
The following assumptions are made based on the Standard Model: m_t, $m_W = 80.4\,\text{GeV}$, the η_ν, $\eta_{\bar{\nu}}$-distributions.
The measurements, assumptions, and equations B.1 and B.2 are used to completely reconstruct the $t\bar{t}$ event, i.e. to calculate p_ν and $p_{\bar{\nu}}$:
From equation B.1 follows:

$$\begin{aligned} m_W{}^2 &= (E_l + E_\nu)^2 - (\vec{p}_l + \vec{p}_\nu)^2 = E_l{}^2 + E_\nu{}^2 + 2E_l E_\nu - \vec{p}_l{}^2 - \vec{p}_\nu{}^2 - 2\vec{p}_l\vec{p}_\nu \\ &= 2(E_l E_\nu - \vec{p}_l\vec{p}_\nu) \\ \Leftrightarrow E_\nu &= |\vec{p}_\nu| = \frac{1}{E_l}\left(\frac{m_W{}^2}{2} + \vec{p}_l\vec{p}_\nu\right) . \end{aligned} \tag{B.3}$$

From equation B.2 follows:

$$\begin{aligned} m_t{}^2 &= (E_l + E_\nu + E_b)^2 - (\vec{p}_l + \vec{p}_\nu + \vec{p}_b)^2 \\ &= m_W{}^2 + m_b{}^2 + 2(E_l E_b + E_\nu E_b - \vec{p}_l\vec{p}_b - \vec{p}_\nu\vec{p}_b) \\ \Leftrightarrow E_\nu &= |\vec{p}_\nu| = \frac{m_t{}^2 - m_W{}^2 - m_b{}^2 - 2p_l p_b}{2E_b} + \frac{\vec{p}_\nu\vec{p}_b}{E_b} . \end{aligned} \tag{B.4}$$

The Lorentz transformation L boosts in z-direction into the system with $p_\nu^z = 0$ GeV:

$$L = \begin{pmatrix} \cosh\eta_\nu & 0 & 0 & -\sinh\eta_\nu \\ 0 & 1 & 0 & 0 \\ 0 & 0 & 1 & 0 \\ -\sinh\eta_\nu & 0 & 0 & \cosh\eta_\nu \end{pmatrix} \tag{B.5}$$

Applying L to equation B.3 yields:

$$\begin{aligned} p_T^\nu &= \frac{{m_W}^2}{2{E_l}'} + \frac{p_l^x p_\nu^x}{{E_l}'} + \frac{p_l^y p_\nu^y}{{E_l}'}, \text{ where} \\ {E_l}' &= E_l \cosh\eta_\nu - p_l^z \sinh\eta_\nu \end{aligned} \tag{B.6}$$

Applying L to equation B.4 yields:

$$\begin{aligned} p_T^\nu &= \frac{{m_t}^2 - {m_W}^2 - {m_b}^2 - 2p_l p_b}{2{E_b}'} + \frac{p_\nu^x p_b^x + p_\nu^y p_b^y}{{E_b}'}, \text{ where} \\ {E_b}' &= E_b \cosh\eta_\nu - p_b^z \sinh\eta_\nu \end{aligned} \tag{B.7}$$

Equation B.6 must give the same result as equation B.7. After solving for p_ν^x one obtains a linear equation:

$$p_\nu^x = a p_\nu^y + b, \text{ where} \tag{B.8}$$

$$a \equiv \frac{p_l^y {E_b}' - p_b^y {E_l}'}{p_b^x {E_l}' - p_l^x {E_b}'} \tag{B.9}$$

$$b \equiv \frac{{E_l}'({m_t}^2 - {m_W}^2 - {m_b}^2 - 2p_l p_b) - {E_b}'{m_W}^2}{2(p_l^x {E_b}' - p_b^x {E_l}')} \tag{B.10}$$

Eliminating p_ν^x in equation B.6 using $p_T^\nu = \sqrt{{p_\nu^x}^2 + {p_\nu^y}^2}$ and equation B.8 gives:

$$\sqrt{(a^2+1)p_\nu^y + 2ab p_\nu^y + b^2} = \frac{{m_W}^2}{2{E_l}'} + \frac{p_l^x}{{E_l}'}(a p_\nu^y + b) + \frac{p_l^y}{{E_l}'} p_\nu^y \tag{B.11}$$

Squaring equation B.11 leads to a quadratic equation in p_ν^y of the form

$$c{p_\nu^y}^2 + d p_\nu^y + f = 0, \tag{B.12}$$

with

$$c \equiv a^2 + 1 - \left(\frac{p_l^x}{{E_l}'}a + \frac{p_l^y}{{E_l}'}\right)^2 \tag{B.13}$$

$$d \equiv 2ab - 2\left(\frac{{m_W}^2}{2{E_l}'} + \frac{p_l^x}{{E_l}'}b\right)\left(\frac{p_l^x}{{E_l}'}a + \frac{p_l^y}{{E_l}'}\right) \tag{B.14}$$

$$f \equiv b^2 - \left(\frac{{m_W}^2}{2{E_l}'} + \frac{p_l^x}{{E_l}'}b\right)^2 \tag{B.15}$$

Equation B.12 has zero, one or two real solutions:

$$p_{\nu\,1/2}^y = -\frac{d}{2c} \pm \frac{1}{2c}\sqrt{d^2 - 4cf} \tag{B.16}$$

p_ν^x can be obtained by plugging in the solution of p_ν^y in equation B.8.
p_ν^z can be calculated with:

$$p_\nu^z = p_T^\nu \sinh\eta_\nu \tag{B.17}$$

Bibliography

[1] S. Weinberg, "A Model of Leptons," *Phys. Rev. Lett.* **19** (1967) 1264–1266.

[2] S. L. Glashow, "Partial Symmetries of Weak Interactions," *Nucl. Phys.* **22** (1961) 579–588.

[3] A. Salam, J. C. Ward, "Electromagnetic and Weak Interactions," *Phys. Lett.* **13** (1964) 168–171.

[4] D. J. Gross and F. Wilczek, "Asymptotically Free Gauge Theories," *Phys. Rev. D* **8** (1973) 3633–3652.

[5] H. D. Politzer, "Asymptotic Freedom: An Approach to Strong Interactions," *Phys. Rept.* **14** (1974) 129.

[6] M. Gell-Mann, "A Schematic Model of Baryons and Mesons," *Phys. Lett.* **8** (1964) 214–215.

[7] P. W. Higgs, "Broken Symmetries, Massless Particles and Gauge Fields," *Phys. Lett.* **12** (1964) 132–133.

[8] **D0** Collaboration, S. Abachi *et al.*, "Observation of the Top Quark," *Phys. Rev. Lett.* **74** (1995) 2632–2637, `hep-ex/9503003`.

[9] **CDF** Collaboration, F. Abe *et al.*, "Observation of Top Quark Production in $p\bar{p}$ Collisions with the Collider Detector at Fermilab," *Phys. Rev. Lett.* **74** (1995) 2626–2631, `hep-ex/9503002`.

[10] Tevatron Electroweak Working Group, "Combination of CDF and DØ Results on the Mass of the Top Quark," `hep-ex/0608032`.

[11] Christian Schwanenberger, talk given in the Top Properties meeting on 15.06.2006, `http://www-d0.hef.kun.nl//fullAgenda.php?ida=a061127`.

[12] **D0** Collaboration, S. Abachi *et al.*, "Measurement of m_{top} in $e\mu$ Events with Neutrino Weighting in Run II at DØ." DØ-Note 5171-CONF (Summer 2006 conferences), July, 2006.

[13] O. Brandt *et al.*, "Measurement of m_{top} in $e\mu$ Events with Neutrino Weighting in Run II at DØ." DØ-Note 5162, July, 2006.

[14] M. E. Peskin, D. V. Schröder, *An Introduction to Quantum Field Theory.* West View Press.

[15] F. Halzen, A. D. Martin, *Quarks and Leptons: an Introductory Course in Modern Particle Physics.* Addison Wesley Press.

[16] D. J. Griffiths, *Introduction to Elementary Particles*. New York, USA: Wiley (1987) 392p.

[17] M. Herrero, "The Standard Model," `hep-ph/9812242`.

[18] V. L. Ginzburg, L. D. Landau, "On the Theory of Superconductivity," *Zh. Eksp. Teor. Fiz.* **20** (1950) 1064.

[19] A. Quadt, "Top Quark Physics at Hadron Colliders." 2006.

[20] W. M. Yao *et al.*, "Review of Particle Physics," *Journal of Physics G* **33** (2006).

[21] N. Kidonakis, R. Vogt, "Next-to-next-to-leading Order Soft Gluon Corrections in Top Quark Hadroproduction," *Phys. Rev. D* **68** (2003) 114014.

[22] N. Kidonakis, R. Vogt, "Top Quark Production at the Tevatron at NNLO," *Eur. Phys. J. C* **33** (2004) s466.

[23] **CTEQ** Collaboration, H. L. Lai *et al.*, "Global QCD analysis of parton structure of the nucleon: Cteq5 parton distributions," *Eur. Phys. J.* **C12** (2000) 375–392, `hep-ph/9903282`.

[24] C. Quigg, "History Plot of Limits on Measuremetns of the Top Quark Mass," *Phys. Today* **50N5** (1997) 20.

[25] LEP-Electroweak Working Group and the LEP Collaborations: ALEPH, DELPHI, L3 and OPAL, "Electroweak Parameters of the Z^0 Resonance and the Standard Model," *Phys. Lett. B* **276** (1992) 247.

[26] The ALEPH, DELPHI, L3, OPAL and SLD Collaborations, the LEP-Electroweak Working Group, the SLD Electroweak and Heavy Flavour Groups, "A Combination of Preliminary Electroweak Measurements and Constraints on the Standard Model," *CERN-PH-EP/2004-069 (2004),* `hep-ex/0412015`.

[27] The ALEPH, DELPHI, L3, OPAL and SLD Collaborations, the LEP-Electroweak Working Group, the SLD Electroweak and Heavy Flavour Groups, "A Combination of Preliminary Electroweak Measurements and Constraints on the Standard Model," *updated for the Summer 2005 conferences,* `http://www.cern.ch/LEPEWWG` (2005).

[28] The LEP Working Group fo Higgs Boson Searches, R. Barate *et al.*, "Search for the Standard Model Higgs at LEP," *Phys. Lett. B* **88** (2002) 61, `hep-ex/0306033`.

[29] The ALEPH, DELPHI, L3, OPAL and SLD Collaborations, the LEP-Electroweak Working Group, the SLD Electroweak and Heavy Flavour Groups, "A Combination of Preliminary Electroweak Measurements and Constraints on the Standard Model," *updated for the Summer 2006 conferences,* `http://www.cern.ch/LEPEWWG` (2006).

[30] A. Czarnecki and K. Melnikov, "Top Loop QCD Corrections to Top Quark Width," *Nucl. Phys. B* **544** (1999) 520, `hep-ph/9806244`.

[31] **D0** Collaboration, V. M. Abazov *et al.*, "Measurement of the W Boson Helicity in Top Quark Decays," *Phys. Rev. D* **72** (2005) 011104, `hep-ex/0505031`.

[32] **D0** Collaboration, V. M. Abazov *et al.*, "Search for Right-handed W-bosons in Dilepton Top Quark Pair Candidates." DØ-Note 482, 2005.

[33] **CDF** Collaboration, A. Abulencia *et al.*, "Measurement of the Helicity of W Bosons in Top Quark Decays." CDF-Note 7806, 2005.

[34] **D0** Collaboration, B. Abbott *et al.*, "Spin Correlation in $t\bar{t}$ Production from $p\bar{p}$ Collisions at $\sqrt{s} = 1.8\,\text{TeV}$," *Phys. Rev. Lett.* **85** (2000) 256, `hep-ex/0002058`.

[35] **D0** Collaboration, V. M. Abazov *et al.*, "Measurement of the Charge of the Top Quark with the DØ Experiment." DØ-Note 4876-CONF (Summer 2005 conferences), 2005.

[36] **D0** Collaboration, V. M. Abazov *et al.*, "Measurement of the $t\bar{t}$ Cross Section at $\sqrt{s} = 1.96\,\text{TeV}$ in Dilepton Final States Using $370\,\text{pb}^{-1}$ of DØ Data." DØ-Note 4850-CONF (Summer 2005 conferences), June, 2005.

[37] **D0** Collaboration, V. M. Abazov *et al.*, "Measurement of the $t\bar{t}$ Production Cross Section in $p\bar{p}$ Collisions at $\sqrt{s} = 1.96\,\text{TeV}$ in Dilepton Final States," *Phys. Lett.* **B626** (2005) 55–64, `hep-ex/0505082`.

[38] **D0** Collaboration, V. M. Abazov *et al.*, "The Upgraded DØ Detector," *Accepted by NIM A* (2005) `physics/0507191`.

[39] Fermilab Beams Division Run II, "Run II Handbook," `http://www-bd.fnal.gov/runII/index.html`, `http://www-bd.fnal.gov/lug` (2001).

[40] **D0** Collaboration, S. Abachi *et al.*, "Direct Measurement of the Top Quark Mass by the DØ Collaboration," *Phys. Rev. D* **58** (1998) 052001.

[41] **CDF** Collaboration, F. Abe *et al.*, "Measurement of the Top Quark Mass with the Collider Detector at Fermilab," *Phys. Rev. D* **63** (2001) 032003.

[42] **D0** Collaboration, V. M. Abazov *et al.*, "A Precision Measurement of the Mass of the Top Quark," *Nature* **429** (2004) 638–642, `hep-ex/0406031`.

[43] **D0** Collaboration, S. Abachi *et al.*, "The DØ Detector," *NIM* **A338** (1994) 185.

[44] **D0** Collaboration, J. Ellison, "The DØ Detector Upgrade and Physics Program," `hep-ex/0101048`.

[45] **D0** Collaboration, S. Abachi *et al.*, "The DØ Upgrade: The Detector and its Physics,". FERMILAB-PUB-96-357-E.

[46] **D0** Collaboration, S. Abachi *et al.*, "DØ Silicon Tracker Technical Design Report." DØ-Note 2169, July, 1997.

[47] **D0** Collaboration, S. Abachi *et al.*, "The DØ Upgrade Central Fiber Tracker: Technical Design Report." DØ-Note 4164, June, 1997.

[48] **D0** Collaboration, S. Abachi *et al.*, "The DØ Detector," *Nucl. Instrum. Meth.* **A338** (1994) 185–253.

[49] L. Groers, "Calorimeter Upgrades for Tevatron Run II." DØ-Note 4240, Proceedings for the IXth International Conference on Calorimetry in Particle Physics, Annecy, France, Oct 9-14, 2000, August, 2000.

[50] A. Gordeev *et al.*, "The DØ Muon System Upgrade." DØ-Note 2780, January, 1996.

[51] T. Diehl *et al.*, "Technical Design of the Central Muon System." DØ-Note 3365, December, 1997.

[52] T. Diehl *et al.*, "Technical Design Report for the DØ Forward Muon Tracking Detector Based on Mini-Drift Tubes." DØ-Note 3366, December, 1997.

[53] T. Diehl *et al.*, "Technical Design Report for the DØ Forward Trigger Scintillator Counters." DØ-Note 3237, November, 1997.

[54] S. Anderson *et al.*, "Measurement of the $t\bar{t}$ Cross Section at $\sqrt{s} = 1.96\,\text{TeV}$ in ee and $\mu\mu$ Final States Using $370\,\text{pb}^{-1}$ of Pass 2 Data." DØ-Note 4827, May, 2005.

[55] M. Besançon *et al.*, "Measurement of the $t\bar{t}$ Production Cross Section at $\sqrt{s} = 1.96\,\text{TeV}$ in $e\mu$ Final States." DØ-Note 4877, July, 2005.

[56] R. Brun *et al.*, "ROOT – an Object-Oriented Data Analysis Framework," `http://root.cern.ch/`.

[57] Top Group of the DØ collaboration `http://www-d0.fnal.gov/Run2Physics/top/d0_private/wg/commonskims/data_rootuples_Ipanema.html`.

[58] Markus Klute, Lukas Phaf and Daniel Whiteson, "TopAnalyze - A Framework Analyze Package For Top Group Analyses." DØ-Note 4122, March, 2003.

[59] Top Group of the DØ collaboration, "DØ Analysis and Data Sample for the Winter Conferences 2004." DØ-Note 4419, April, 2004.

[60] Top Group of the DØ collaboration `http://www-d0.fnal.gov/computing/data_quality/d0_private/forusers.html`.

[61] Top Group of the DØ collaboration `http://www-d0.fnal.gov/Run2Physics/top/d0_private/wg/triggers/triggers.html`.

[62] A. Magerkurth, "Parton Level Corrections for `JetCorr 5.3`." DØ-Note 4708, February, 2005.

[63] **D0** Collaboration, V. M. Abazov *et al.*, "Measurement of the Top Quark Mass with the Matrix Element Method at D0 Run-II." DØ-Note 4717, DØ-Note 5053-CONF, February, 2005.

[64] P. Calfayan *et al.*, "Muon Identification Certification for `p17` data." DØ-Note 5157, June, 2006.

[65] R. Brun *et al.*, "GEANT – Detector Description and Simulation Tool," *CERN Program Library Vers. 3.21* **W5013** (1993).

[66] J. Hays, J. Mitrevski, C. Schwanenberger, T. Toole, "Single Electron Efficiencies in `p17` Data and Monte-Carlo." DØ-Note 5025, February, 2006.

[67] J. Hays, J. Mitrevski, C. Schwanenberger, T. Toole, "Single Electron Trigger Efficiencies in `p17` Data." DØ-Note 5069, March, 2006.

[68] P. Verdier, talk in the Top Precision meeting on 10.07.2006, `http://www-d0.hef.kun.nl//fullAgenda.php?ida=a061229`.

[69] M. Besançon *et al.*, "Measurement of the $t\bar{t}$ Production Cross Section at $\sqrt{s} = 1.96\,\text{TeV}$ in $e\mu$ Final States Using p17 Data Set." DØ-Note 4877 (preliminary), February, 2005.

[70] Top Group of the DØ collaboration `https://plone3.fnal.gov/d0wiki/caf/`.

[71] M. L. Mangano, M. Moretti, F. Piccinini, R. Pittau, and A. D. Polosa, "ALPGEN, a Generator for Hard Multiparton Processes in Hadronic Collisions," *JHEP* **07** (2003) 001, `hep-ph/0206293`.

[72] Sjöstrand, Torbjörn *et al.*, "PYTHIA 6.2 Physics and Manual," *Comp. Phys. Comm.* **135** (2001) 238, `hep-ph/0108264`.

[73] S.Jadach, Z.Was, R. Decker, M. Kuhn, and H. Johann, "The Tau Decay Library TAUOLA: Version 2.4," *Comput. Phys. Commun.* **76** (1993) 361–380.

[74] M. Gagliardi, J. Hays, J. Mitrevski, C. Schwanenberger, T. Toole, "Electron Certification in `p14`." DØ-Note 4783, April, 2005.

[75] C. Clement, F. Deliot, T. Golling, K. Haganaki, B. Leonhardt, M. Mulders, E. Nurse, S. Söldner-Remboldt, J. Stark, "MuonID Certification for `p14`." DØ-Note 4350, February, 2004.

[76] DØ Common Samples Group homepage `http://www-d0.fnal.gov/Run2Physics/cs/index.html`.

[77] Oleg Brandt, talk given in the Top Properties meeting on 16.03.2006, `http://www-d0.hef.kun.nl//fullAgenda.php?ida=a06506`.

[78] Campbell, J. M. and Ellis, R. K., "An Update on Vector Boson Pair Production at Hadron Colliders," *Phys. Rev.* **D60** (1999) 113006, `hep-ph/9905386`.

[79] D. Stump *et al.*, "Inclusive jet production, parton distributions, and the dearch for new physics," *JHEP* **10** (2003) 046, `hep-ph/0303013`.

[80] J. Hays, V. Kaushik, J. Mitrevski, O. Mundal, C. Schwanenberger, "Electron Trigger Efficiencies using Calorimeter Information in `p17` Data." DØ-Note 5138, June, 2006.

[81] Nikola Makovec, Jean-François Grivaz, "Shifting, Smearing, and Removing Simulated Jets." DØ-Note 4914, August, 2005.

[82] S. Anderson *et al.*, "Measurement of m_{top} in Dilepton Events with Neutrino Weighting,". DØ-Note 4983.

[83] Su-Jung Park, *Measuring the $t\bar{t}$ Production Cross Section in the Electron-Plus-Jets Channel*. Diploma thesis, University of Bonn, BONN-IB-2004-05, 2004.

[84] Oleg Brandt, talk given in the University of Bonn meeting on 07.03.2006, `http://www-d0.hef.kun.nl//fullAgenda.php?ida=a06471`.

[85] D. Boline, U. Heintz, "Measurement of the Top Quark Mass in the $e\mu$ Channel Using the Matrix Weighting Method at DØ." DØ-Note (in preparation), DØ conference note (in preparation for Summer 2006 conferences).

[86] L. Wang, J. Hays, J. Mitrevski, C. Schwanenberger, "Electron Likelihood Efficiency in `p17`." DØ-Note 5114, May, 2006.

[87] K. Kondo, "Dynamical Likelihood Method for Reconstruction of Events with Missing Momentum. I. Method and Toy Models," *J. Phys. Soc. Jpn.* **57** (1988) 4126.

[88] K. Kondo, "Dynamical Likelihood Method for Reconstruction of Events with Missing Momentum. II. Mass Spectra for $2 \to 2$ Processes," *J. Phys. Soc. Jpn.* **60** (1991) 836.

[89] **D0** Collaboration, B. Abbott *et al.*, "Measurement of the Top Quark Mass in the Dilepton Channel," *Phys. Rev.* **D60** (1999) 052001, `hep-ex/9808029`.

[90] E. W. Varnes. Ph. D. thesis, University of California at Berkeley, 1997.

[91] **CDF** Collaboration, D. Acosta *et al.*, "Measurement of the Top Quark Mass Using the Neutrino Weighting Algorithm on Dilepton Events at CDF." CDF-Note 7303.

[92] Jörg Meyer, University of Bonn, *private communication* (2006).

[93] **CDF** Collaboration, D. Acosta *et al.*, "Measurement of the $t\bar{t}$ Production Cross Section in $p\bar{p}$ Collisions at $\sqrt{s} = 1.96$ TeV Using Dilepton Events," *Phys. Rev. Lett.* **93** (2004) 142001, `hep-ex/0404036`.

[94] J. Kozminski, *Measurement of the Top Quark Mass in Dilepton Events Using Neutrino Constraints*. Ph.D. thesis, Michigan State University, 2005.

[95] P. Renkel, B. Kehoe, talk given in the Top Precision Meeting on 30.05.2006, `http://www-d0.hef.kun.nl//fullAgenda.php?ida=a06976`.

[96] L. Wang *private communication, work in progress* (2006).

[97] Jan Stark, talk given in the W Mass meeting on 13.01.2006, `http://www-d0.hef.kun.nl//fullAgenda.php?ida=a0651`.

[98] P. Schieferdecker, M. Wang, "Jet Transfer Functions Derived from `p17` Monte Carlo." DØ-Note 5136 (in preparation), 2006.

[99] R. Barlow, *Statistics: a Guide to the Use of Statistical Methods in the Physical Sciences*. The Manchester Physics Series, New York, Wiley, 1989.

[100] F. James and M. Roos, "'MINUIT' – A System for Function Minimization and Analysis of the Parameter Errors and Correlations," *Comp. Phys. Comm.* **10** (1975) 343–367.

[101] L. Holmström, S. R. Sain, H. E. Miettinen,, "A New Multivariate Technique for Top Quark Search," *Comput. Phys. Commun.* **88** (1995) 195–210.

[102] M. Mulders, "Ensemble Testing for the Top Mass Measurement." DØ-Note 4460, June, 2004.

[103] Martijn Mulders, Michele Weber, "Top Mass Measurement with b-tagging in the Lepton+Jets Channel using the Ideogram Method in Run II." DØ-Note 4705, February, 2005.

[104] DØ Jet Energy Scale Working Group homepage `http://www-d0.fnal.gov/phys_id/jes/d0_private/jes.html`.

[105] V. Büscher, J.-F. Grivaz, T. Nunnemann, M. Wobisch, "Conclusions of Mini-Workshop on PDF Uncertainties and Related Topics." DØ-Note 4618, September, 2004.

[106] DØ Monte Carlo Production Group, "PMCS Documentation," `http://www-d0.fnal.gov/computing/MonteCarlo/pmcs/pmcs_doc/pmcs.html`.

[107] D. Boline, U. Heintz, "Measurement of the Top Quark Mass in the Dilepton Channel." DØ-Note 4997, January, 2006.

Acknowledgements

It is my firm belief that the last year was one of its most interesting, intriguing and challenging periods of my entire life. Moreover, it was fundamental for my future in Science, and I really appreciate the great experience and passion I could gain during this time. I would like thank all the people who helped me in that enterprise.

For the scientific part of the last year, I would to give thanks to the members of the group of Prof. Norbert Wermes for their support, especially to the members of the DØ Group: Jörg Meyer, Dr. Marc-André Pleier, Prof. Arnulf Quadt, Dr. Christian Schwanenberger, and Dr. Eckhard von Törne.

I am very grateful to Prof. Norbert Wermes for giving me the opportunity to spend 10 months at the DØ experiment at Fermilab, experience the everyday life in an Elementary Particle Physics laboratory and meet excellent scientists from all over the world. I especially appreciate his advise on the choice of the Diploma thesis topic.

I owe a very special word of gratitude to my direct scientific advisers: Prof. Arnulf Quadt and Dr. Christian Schwanenberger. Most important to me are precious and extensive scientific discussions we had when developing and understanding the Maximum Method. I learned a lot from their clear reasoning and intuition. But it is not only the discussions we had, it is also the passion for Science they shared with me and their constant encouragement. In the same spirit I would like to thank Jörg Meyer not only for the detailed and precious conversations, but also for his help with technical questions. He taught me skills and good manners in programming.

I am also thankful to the members of the Top Group at DØ, especially to the conveners of the Top Properties subgroup, Regina Demina and Erich Varnes, for having a watchful eye on the Maximum Method analysis, and to Robert Kehoe and Peter Renkel for their constant advise and the contributions to the Neutrino Weighting results for ICHEP 2006. From the Top Group in general, I would like to mention the help of Jeffrey Temple, Daniel Boline, Stephan Anderson, and Viatcheslav Sharyy.

I am grateful for the financial support I received from the Deutscher Akademischer Austauschdienst to spend additional time at the experiment. I am especially grateful to the Studienstiftung des Deutschen Volkes for its financial and ideological support during my studies which has lead to this thesis and for the many interesting contacts I made during this time.

Finally, I would like to thank my family for their constant support and encouragement, not only in the past year or during my studies, but in the course of my whole life. I thank all of my friends and especially my girlfriend Katia for the support the great times we shared during my studies. I am very grateful to Sergey and Tamara Los, Taejeong Kim and Pierre Poirot for helping me feel at home during the time at Fermilab.